University of South Carolina
Scholar Commons

Theses and Dissertations

1-1-2013

# Crystal Growth, Characterization and Fabrication of CDZNTE-Based Nuclear Detectors

Ramesh Madhu Krishna
*University of South Carolina*

Follow this and additional works at: http://scholarcommons.sc.edu/etd

Recommended Citation
Krishna, R. M.(2013). *Crystal Growth, Characterization and Fabrication of CDZNTE-Based Nuclear Detectors.* (Doctoral dissertation). Retrieved from http://scholarcommons.sc.edu/etd/2410

This Open Access Dissertation is brought to you for free and open access by Scholar Commons. It has been accepted for inclusion in Theses and Dissertations by an authorized administrator of Scholar Commons. For more information, please contact SCHOLARC@mailbox.sc.edu.

# CRYSTAL GROWTH, CHARACTERIZATION AND FABRICATION OF CDZNTE-BASED NUCLEAR DETECTORS

by

Ramesh M. Krishna

Bachelor of Science
Clemson University, 2007

---

Submitted in Partial Fulfillment of the Requirements

For the Degree of Doctor of Philosophy in

Electrical Engineering

College of Engineering and Computing

University of South Carolina

2013

Accepted by:

Krishna C. Mandal, Major Professor

Guoan Wang, Committee Member

Charles W. Brice, Committee Member

Harry J. Ploehn, Committee Member

Lacy Ford, Vice Provost and Dean of Graduate Studies

© Copyright by Ramesh Krishna, 2013
All Rights Reserved.

## ACKNOWLEDGEMENTS

Firstly, I would like to thank my advisor, Dr. Krishna C. Mandal, for his continued support and guidance on this research. My development within his group has allowed me to undertake this work with the proper knowledge and skillset I otherwise would not have. I would also like to thank my committee members, Dr. Harry J. Ploehn, Dr. Guoan Wang, and Dr. Charles W. Brice, for taking the time to oversee my research and their support of my work.

I would also like to thank the following people for their contributions to the research performed in this work:

- Timothy Hayes, who assisted heavily to design and build the electronics and software for the entirety of the crystal growth furnaces and zone-refiner, and the mechanical construction and design of the carbon coating system.
- Dr. Peter Muzykov, who led the project for doing TSC spectroscopy on CZT, which I assisted with. Peter also assisted in the EBIC characterization of CZT.
- Dr. Shugo Ma, who performed the XPS characterization on the unmodified and surface modified CZT samples.
- The Electron Microscopy Center, for their assistance with SEM and EDS studies.
- Prof. Harry J. Ploehn and Yating Mao, for their assistance with performing AFM studies on the chemically etched CZT samples.

- Dr. Sandeep Chaudhuri and Kelvin Zavalla, for their assistance in updating the digital correction scheme used to correct the planar CZT detector's pulse height spectrum.
- Prof. Arnold Burger and Michael Groza from Fisk University for their assistance with fabrication of the Small pixel guard ring CZT detector.

I would also like to thank my fellow lab members, Dr. Sandeep Chaudhuri, Kelvin Zavalla, Abhinav Metha, Timothy Hayes, Sandip Das, and M. A. Mannan for their support and friendship throughout this process. Finally, I would like to thank my friends, family, and all those who have not been mentioned here. Without their contributions, this work would have been impossible to perform.

# ABSTRACT

In today's world, nuclear radiation is seeing more and more use by humanity as time goes on. Nuclear power plants are being built to supply humanity's energy needs, nuclear medical imaging is becoming more popular for diagnosing cancer and other diseases, and control of weapons-grade nuclear materials is becoming more and more important for national security. All of these needs require high-performance nuclear radiation detectors which can accurately measure the type and amount of radiation being used. However, most current radiation detection materials available commercially require extensive cooling, or simply do not function adequately for high-energy gamma-ray emitting nuclear materials such as uranium and plutonium.

One of the most promising semiconductor materials being considered to create a convenient, field-deployable nuclear detector is cadmium zinc telluride (CdZnTe, or CZT). CZT is a ternary semiconductor compound which can detect high-energy gamma-rays at room temperature. It offers high resistivity ($\geq 10^{10}$ Ω-cm), a high band gap (1.55 eV), and good electron transport properties, all of which are required for a nuclear radiation detector. However, one significant issue with CZT is that there is considerable difficulty in growing large, homogeneous, defect-free single crystals of CZT. This significantly increases the cost of producing CZT detectors, making CZT less than ideal for mass-production. Furthermore, CZT suffers from poor hole transport properties, which creates significant problems when using it as a high-energy gamma-ray detector.

In this dissertation, a comprehensive investigation is undertaken using a successful growth method for CZT developed at the University of South Carolina. This method, called the solvent-growth technique, reduces the complexity required to grow detector-grade CZT single crystals. It utilizes a lower growth temperature than traditional growth methods by using Te as a solvent, while maintaining the advantages of crystal homogeneity of other modern CZT growth techniques. However, information about crystals grown with this method has not been undertaken in a comprehensive way thus far.

In this work, $Cd_{0.9}Zn_{0.1}Te$ is grown using the solvent-growth method using zone-refined precursor materials loaded into carbon-coated quartz ampoules. Ampoules were sealed and crystal growth was performed using crystal growth furnaces built in-house at USC. Ingots 1-2" in diameter produced using the solvent-growth method were wafered, processed, and polished for characterization. Semiconductor characterization is performed on the CZT crystals to determine band gap, elemental stoichiometry, and electrical resistivity. Surface modification studies were undertaken to determine if surface leakage current can be reduced using sulfur passivation. XPS studies were used to confirm the effects of passivation on the surface states, and electrical characterization was performed to measure the effects of passivation on the CZT crystals. Deep-level and surface defect studies were conducted on the CZT samples to determine the type and intensity of defects present in the crystals which may affect detector performance. Finally, nuclear detectors were fabricated and characterized using analog and digital radiation detection systems to measure their performance and energy resolution.

TABLE OF CONTENTS

**ACKNOWLEDGEMENTS ... III**

**ABSTRACT ... V**

**LIST OF TABLES ... X**

**LIST OF FIGURES ... XI**

**LIST OF ABBREVIATIONS ... XVII**

**CHAPTER 1: GENERAL INTRODUCTION ... 1**

1.1 DISSERTATION INTRODUCTION ... 1

1.2 DISSERTATION OVERVIEW ... 2

1.3 INTRODUCTION TO RADIATION DETECTION MATERIALS AND DEVICES ... 4

**CHAPTER 2: CRYSTAL GROWTH ... 11**

2.1 OVERVIEW ... 11

2.2 PRECURSOR PREPARATION BY ZONE REFINING ... 13

2.3 CARBON COATING OF QUARTZ AMPOULES ... 18

2.4 PRIOR GROWTH TECHNIQUES ... 21

2.5 SOLVENT GROWTH TECHNIQUE ... 25

2.6 CONCLUSION ... 30

**CHAPTER 3: CRYSTAL CHARACTERIZATION ... 31**

3.1 OVERVIEW ... 31

3.2 CRYSTAL PREPARATION ... 31

3.3 OPTICAL TRANSMISSION ... 33

3.4 ENERGY-DISPERSIVE X-RAY SPECTROSCOPY ... 34

3.5 INFRARED TRANSMISSION IMAGING ........ 37
3.6 ELECTRICAL CHARACTERIZATION ........ 38
3.7 CONCLUSION ........ 47
**CHAPTER 4: SURFACE MODIFICATION ........ 49**
4.1 OVERVIEW ........ 49
4.2 PASSIVATION THEORY ........ 50
4.3 EXPERIMENTAL ........ 51
4.4 X-RAY PHOTOELECTRON SPECTROSCOPY ........ 52
4.5 PASSIVATION AND ELECTRICAL CHARACTERIZATION ........ 59
4.6 CONCLUSION ........ 61
**CHAPTER 5: DEFECT CHARACTERIZATION ........ 62**
5.1 OVERVIEW ........ 62
5.2 THERMALLY STIMULATED CURRENT ........ 63
5.3 CHEMICAL ETCHING ........ 68
5.4 ELECTRON BEAM INDUCED CURRENT ........ 73
5.5 CONCLUSION ........ 77
**CHAPTER 6: DETECTOR FABRICATION AND CHARACTERIZATION ........ 78**
6.1 THEORETICAL DISCUSSION OF RADIATION INTERACTION ........ 78
6.2 DETECTOR STRUCTURES ........ 85
6.3 ANALOG RADIATION DETECTION ........ 95
6.4 DIGITAL SIGNAL PROCESSING FOR RADIATION DETECTION ........ 108
6.5 BIPARAMETRIC PLOTS AND DIGITAL CORRECTION SCHEMES ........ 116
6.6 CHARGE TRANSPORT MEASUREMENTS ........ 118
6.7 DETECTOR CHARACTERIZATION RESULTS ........ 126
6.8 CONCLUSION ........ 143

**CHAPTER 7: CONCLUSION AND FUTURE WORK ........................................... 144**

7.1 CONCLUSION........................................................................................... 144

7.2 FUTURE WORK ........................................................................................ 145

**REFERENCES.......................................................................................... 147**

**APPENDIX A – CARBON COATER MECHANICAL DRAWINGS.................... 154**

**APPENDIX B – CRYSTAL GROWTH FURNACE SOFTWARE......................... 155**

**APPENDIX C – MATLAB SOFTWARE FOR PULSE SHAPING........................ 172**

LIST OF TABLES

Table 1.1. Ideal qualities of a semiconductor gamma-ray and X-ray detector. .................. 6

Table 1.2. Material properties of CdZnTe. ........................................................................ 8

Table 1.3. Physical properties of popular X-ray and γ-ray semiconductors at T = 25°C [6] ..................................................................................................................... 9

Table 2.1. Glow Discharge Mass Spectroscopy (GDMS) impurity analysis for zone refined Cd, Zn, and Te. Impurity concentration in parts per billion. ND = Not detected. ............................................................................................................. 16

Table 3.1. EDS stoichiometry data for CZT samples, along with error percent. All values are given in atomic percentage (%at)................................................................. 36

Table 3.2. Work Functions of selected contact metals for CZT [33]. ............................. 40

Table 3.3. CZT samples and detectors used for I-V studies. ........................................... 41

Table 3.4. Comparison of leakage current and resistivity of fabricated CZT detectors. .. 47

Table 5.1. Trap parameters deduced from TSC measurements of the fabricated CZT Schottky diodes related to major defect levels. .................................................... 68

Table 5.2. Summary of results for etched CZT samples E1 and E2. ................................ 72

Table 6.1. CZT detectors used for nuclear spectroscopy studies...................................... 94

LIST OF FIGURES

Figure 1.1. (a) Simple schematic of the operation of a semiconductor nuclear detector, and (b) a 1 $cm^3$ CdZnTe detector fabricated in the laboratory. ............................. 5

Figure 2.1. Phase Diagram for CdTe [11]....................................................................... 12

Figure 2.2. Phase Diagram for CdZnTe. Top line indicates liquidus temperatures, bottom line indicates solidus temperatures [11]............................................................. 13

Figure 2.3. (a) Typical zone refining furnace schematic, showing the solid and molten portions of the material. (b) Effect of the number of passes (1, 5, and 10) over the material, and its effect on impurities. [15].......................................................... 15

Figure 2.4. Typical zone refined precursor material produced in the laboratory, with impurities segregated to left side of the ampoule, and pure precursor material on right side............................................................................................................. 17

Figure 2.5. Schematic diagram of carbon coating system developed in our laboratory for coating quartz ampoules. ......................................................................... 19

Figure 2.6. Schematic diagram of the furnace end of the carbon coating system, showing the inlet, ampoule encasement, and exhaust for the system. ............................... 19

Figure 2.7. Carbon Coating system for quartz ampoules, installed in the laboratory....... 20

Figure 2.8. Typical quartz ampoule after carbon coating and annealing process is completed............................................................................................................ 21

Figure 2.9. Schematic diagram of a vertical Bridgman crystal growth process (a) in the hot zone and (b) while moving through the cold zone......................................... 22

Figure 2.10. (a) Example schematic of THM crystal growth, used for HgCdTe. (b) THM crystal growth showing what happens to the precursor materials as the heater makes multiple passes through the ampoule. [18]............................................. 23

Figure 2.11. Schematic diagram of solution growth method for CZT............................. 26

Figure 2.12. (a) Schematic of crystal growth furnaces built in our laboratory at USC, ... 27

Figure 2.13. Typical crystal growth profile used for CZT, showing the ramp-up, crystal growth, and cooldown phases of the growth. ..................................................... 29

Figure 2.14. Images of a 2” CZT ingot produced in our laboratory. ............................... 30

Figure 3.1. (a) SEM image and (b) AFM tapping mode image of the surface of an example of a CZT sample after polishing and etching. ....................................... 32

Figure 3.2. Optical transmission properties of a solution-growth CZT wafer. ................ 33

Figure 3.3. Samples harvested from CZT ingot for EDS studies. .................................. 35

Figure 3.4. Infrared transmission image of a represntative portion of a grown CZT crystal (Scale: 1.2mm width x 1.0mm height)................................................................ 37

Figure 3.5. (a) Schematic [8] and (b) band diagram of a semiconductor nuclear detector under irradiation [8]. ........................................................................................... 38

Figure 3.6. Band diagrams of Ohmic and Schottky contacts of p-type Ohmic and p-type Schottky contacts [32]............................................................................................ 39

Figure 3.7. I-V characteristics of a detector-grade CZT crystal with Ohmic contacts, and a linear fit of the I-V curve used for resistivity measurements............................... 43

Figure 3.8. (a) I-V characteristics of a CZT crystal with Schottky contacts (indium and platinum), and (b) inset showing detailed reverse bias I-V characteristics. ......... 44

Figure 3.9. I-V characteristics of detector P1 from -1100V to +1100V. ......................... 45

Figure 3.10. I-V characteristics of detectors FG1 and FG2 from -1100V to +1100V...... 46

Figure 3.11. I-V characteristics of detector PGR1 from 0V to +4000V.......................... 46

Figure 4.1. Band-diagram showing the Schottky semiconductor-metal interface for (a) an unmodified semiconductor with surface states and (b) surface state splitting due to passivation. [41]........................................................................................... 51

Figure 4.2. Schematic diagram of binding energy and Kinetic energy of a displaced electron due to x-ray interaction with a material. ................................................ 53

Figure 4.3. XPS survey scan for (a) unmodified CZT sample (no passivation), (b) $Na_2S$ modified CZT sample, and (c) $(NH_4)_2S$ modified CZT sample. ......................... 54

Figure 4.4. High-resolution XPS spectra of Cd *3d* core levels for unmodified, $Na_2S$ modified, and $(NH_4)_2S$ modified CZT crystals.................................................... 55

Figure 4.5. High-resolution XPS spectra of Te *3d* core levels for unmodified, $Na_2S$ modified, and $(NH_4)_2S$ modified CZT crystals.................................................... 56

Figure 4.6. High-resolution XPS spectra of Te *4d* core levels for unmodified, $Na_2S$ modified, and $(NH_4)_2S$ modified CZT crystals.................................................... 57

Figure 4.7. High-resolution XPS spectra of S *2p* core levels for $Na_2S$ modified and $(NH_4)_2S$ modified CZT crystals. ............ 58

Figure 4.8. I-V characteristics of (a) CZT sample A, and (b) CZT sample B, showing unpassivated and passivated electrical properties for Ohmic contacts. ............ 59

Figure 4.9. I-V characteristics of (a) CZT sample C and (b) CZT sample D, showing unpassivated and passivated electrical characteristics for Schottky contacts. ...... 60

Figure 5.1. Schematic of TSC spectrum showing trap centers at temperatures $T_{m1}$ and $T_{m2}$ [56]. ............ 63

Figure 5.2. Schematic of the TSC experimental setup ............ 65

Figure 5.3. (a) TSC spectra obtained using CZT Schottky diode at 4, 8, and 15 K/min heat rates and 10 V bias, (b) TSC spectra from panel (a) with subtracted leakage current. ............ 66

Figure 5.4. (a) TSC spectra for the CZT crystal at 0, 1, and 10 V reverse bias voltage and 15 K/min heat rate. (b) TSC spectra for CZT crystal at 4, 8, and 15 K/min and 0 V bias. ............ 66

Figure 5.5. (a) Arrhenius plot deduced from the TSC spectra at 10 V and 0 V bias shown in Figure 5.3b and Figure 5.4b respectively. (b) Theoretical fit of peaks # 1 and #2 in Figure 5.3b using nine energy levels in the range 0.18 – 0.47 eV. ............ 67

Figure 5.6. (a) Topography and (b) deflection contact-mode AFM images of CZT Sample E1. ............ 70

Figure 5.7. SEM image of CZT Sample E1. ............ 70

Figure 5.8. (a) Tapping-mode AFM topography image, and (b) SEM image of CZT Sample E2. ............ 71

Figure 5.9. I-V characteristics and resistivity calculations for CZT samples (a) E1 and (b) E2. ............ 72

Figure 5.10. Schematic of EBIC setup ............ 73

Figure 5.11. (a) EBIC image of a CZT crystal at 80 V reverse bias, and (b) 500X optical image of the of the CZT crystal after chemical etching ............ 76

Figure 6.1. (a) Schematic of gamma-rays escaping a detector material after Compton scattering, before having a chance to interact with the detector again [73]. (b) Effect of Compton scattering on detection signal [73]. ............ 81

Figure 6.2. Left: Contact electrode schematic of a CZT planar detector. Right: The CZT planar detector P1 fabricated in the laboratory, and mounted on a PCB. ............ 85

Figure 6.3. Schematic showing the weighting potential seen by the anode of a planar detector, and the contribution of electrons and holes to detection signal [74]. .... 87

Figure 6.4. Weighting potential of a small pixel detector shown with different pixel pitch/detector thickness ratios [78]. ........................................................................ 89

Figure 6.5. (a) Side and (b) Top view schematics of a guard ring structure, (c) Picture of CZT detector PGR1. ........................................................................................ 90

Figure 6.6. Weighting potential of a virtual Frisch grid detector. ................................... 91

Figure 6.7. (a) Cross-sectional schematic of a Frisch collar CZT detector. (b) Schematic showing the focused electric field within a Frisch collar detector [82]. (c) Schematic showing the location of the virtual Frisch grid within a Frisch collar detector [82]. ............................................................................................... 93

Figure 6.8. Two virtual Frisch grid CZT detectors fabricated in the laboratory. Detector on right is named FG1; detector on left is named FG2........................................ 94

Figure 6.9. Schematic diagram of an analog nuclear detection measurement system...... 95

Figure 6.10. (a) Simplified circuit diagram for a charge sensitive preamplifier used in a detection system. (b) Typical input and output pulse shapes seen by a preamplifier [90]................................................................................................................ 96

Figure 6.11. (a) Typical input and output pulse shapes seen by a shaping amplifier. (b) Simplified circuit diagram for the various stages of differentiation (CR) and integration (RC) used by an analog shaping amplifier [90]................................. 97

Figure 6.12. (a) Basic connection diagram for a CZT nuclear detector inside of the shielded test box, (b) picture of the radiation detection system at USC, and (c) picture of the shielded aluminum testing box with CZT detector. ....................... 98

Figure 6.13. Schematic of a radiation detection system under calibration conditions. .... 99

Figure 6.14. (a) Pulse height spectrum obtained for six different pulse sizes, and (b) Corresponding calibration curve......................................................................... 101

Figure 6.15. Pulser peaks generated for Amptek A250CF and Cremat CR110 charge sensitive preamplifiers in a calibration configuration (using CZT equivalent detector calculation)........................................................................................... 103

Figure 6.16. Relationship between spectroscopic amplifier shaping time and equivalent noise present in a radiation detection system. [77] ............................................ 104

Figure 6.17. Effects of varying voltage bias for detector FG1 under $^{241}$Am irradiation on (a) photopeak and pulser resolution (lower is better), and (b) peak centroid (higher is better) ........................................................................................................ 107

Figure 6.18. Peak and pulser resolution for detector FG1 taken with varying amplifier shaping times under $^{241}$Am irradiation (lower is better). .................................. 108

Figure 6.19. An example of an ADC coding scheme for an 8-bit resolution ADC [83]. 109

Figure 6.20. Schematic diagram of a digital nuclear detection measurement system. ... 111

Figure 6.21. (a) Digitized test pulse prior to digital shaping. (b) Test pulse shaped using a CR-(RC)$^4$ digital filter algorithm using MATLAB. ......................................... 114

Figure 6.22. Pulse height distribution generated using pulse heights calculated based on digitally stored detector pulses from a CZT detector using a $^{137}$Cs source. ....... 114

Figure 6.23. Oscilloscope snapshot showing pre-amplifier output of an alpha particle signal detected using CZT. ................................................................... 115

Figure 6.24. Rise-time distribution generated using rise-times calculated based on digitally stored detector pulses from a CZT detector using a $^{137}$Cs source. ....... 116

Figure 6.25. Diagram showing how a biparametric plot is generated from rise-times and pulse-heights calculated from nuclear detector pulses....................................... 117

Figure 6.26. Schematic of mobility ($\mu_e$) and the mobility-lifetime product ($\mu\tau_e$) measurements for electrons in a CZT radiation detector. .................................. 120

Figure 6.27. Histogram of rise times generated from the planar CZT detector PL1 biased at 900V. ........................................................................................ 121

Figure 6.28. Drift velocity vs. Electric field plot for the planar CZT detector PL1. The slope of the linear fit of the data gives the mobility of the CZT detector crystal. ........................................................................................................ 122

Figure 6.29. Alpha particle spectra at varying voltage bias for CZT planar detector P1 irradiated with $^{241}$Am. ........................................................................ 124

Figure 6.30. Charge collection efficiency vs. bias voltage plot for the planar CZT detector PL1. Fitting the data with the Hecht equation gives the $\mu\tau_e$ of the CZT crystal. 125

Figure 6.31. $^{241}$Am pulse height spectrum obtained from CZT detector P1 biased at 700V. ........................................................................................................ 126

Figure 6.32. $^{137}$Cs pulse height spectrum obtained from CZT detector P1 biased at 1000V. ........................................................................................................ 127

Figure 6.33. $^{241}$Am pulse height spectrum obtained from CZT detector FG1 biased at 550V. ........................................................................................ 128

Figure 6.34. $^{137}$Cs pulse height spectrum obtained from CZT detector FG1 biased at 1100V. ........................................................................................ 129

Figure 6.35. Comparison of $^{137}Cs$ spectrum taken from detectors P1 and FG1. ............ 130

Figure 6.36. Biparametric plot of CZT detector P1 biased at 1000V, irradiated using $^{137}Cs$ source. Brighter regions indicate higher frequency of counts. ........................... 131

Figure 6.37. Biparametric plot of CZT detector FG1 biased at 1200V, irradiated using $^{137}Cs$ source. ........................................................................................... 132

Figure 6.38. $^{137}Cs$ pulse-height spectra generated from the biparametric plot for events from four different depth-intervals in CZT detector P1. Interval 1 shows spectrum from events close to the anode, while interval 4 shows spectrum from events close to the cathode. ........................................................................................... 134

Figure 6.39. Biparametric plot obtained from interaction of 662 keV gamma rays with the planar detector P1 (a) uncorrected (b) corrected................................................ 135

Figure 6.40. Corrected pulse height spectrum generated from the digital corrections applied to the biparametric plot of detector P1 shown in Figure 6.39. ............... 136

Figure 6.41. $^{137}Cs$ pulse height spectrum obtained from CZT detector FG2 biased at 1200V........................................................................................................ 137

Figure 6.42. Rise-time distribution calculated from detection pulses from $^{137}Cs$ for CZT detectors (a) FG1 and (b) FG2. ............................................................. 138

Figure 6.43. Biparametric plot of CZT detector FG2 biased at 1500V, irradiated using $^{137}Cs$ source. ........................................................................................... 139

Figure 6.44. Biparametric plot obtained from detector FG2 after applied digital corrections. ........................................................................................... 140

Figure 6.45. Pulse height distribution obtained (a) before and (b) after digital corrections from the digital radiation detection system for detector FG2. ............................ 141

Figure 6.46. Analog pulse height spectrum obtained (a) with the guard ring disconnected and (b) with the guard ring connected for detector PGR1. ................................. 142

# LIST OF ABBREVIATIONS

AFM .......... Atomic Force Microscopy

at% .......... Atomic Percentage

CdTe .......... Cadmium Telluride

CZT .......... Cadmium Zinc Telluride

EBIC .......... Electron Beam Induced Current

EDS .......... Energy Dispersive X-ray Spectroscopy

FWHM .......... Full Width at Half Maxima

GDMS .......... Glow Discharge Mass Spectroscopy

keV .......... Kilo Electron Volt

MeV .......... Mega Electron Volt

MCA .......... Multi-Channel Analyzer

SEM .......... Scanning Electron Microscopy

TSC .......... Thermally Stimulated Current

$\mu\tau$ .......... Mobility-Lifetime Product

XPS .......... X-ray Photoelectron Spectroscopy

ZR .......... Zone Refined

# CHAPTER 1: GENERAL INTRODUCTION

## 1.1 DISSERTATION INTRODUCTION

In the world today, radiation and its use by humanity is growing by the minute. Communities small and large use nuclear radiation to power their homes without harmful fumes and toxic pollution. Scientists use radiation to detect and image cancer cells within the human body [1, 2]. Nuclear radioactive materials are proliferated by various entities to cause mass destruction by exploding nuclear bombs. As the number of uses continue to increase, the dangers of radiation, specifically the high energy gamma-rays emitted by these applications, and the need to detect it become more and more apparent. Due to the hazardous nature of nuclear radiation to humans, specific information such as the dosage exposure, type of isotope, and location of the radiation in a given environment will be essential for government agencies and private sector companies.

To fulfill the needs of accurate and precise radiation detection measurements, semiconductors are used for their excellent resolution for detecting radiation. Solid state semiconductor detectors absorb ionizing radiation, such as X-rays, gamma-rays, and alpha particles, from radioactive materials. The radiation waves or particles generate electron-hole pairs, which are separated using a voltage bias applied to the semiconductor and collected by the front-end readout electronics. Several excellent semiconductor materials are available for nuclear radiation detection purposes, such as silicon (Si), high-purity germanium (HPGe), and mercuric iodide ($HgI_2$). However, the most interesting and

commercially pursued detector material for X-ray and gamma-ray detection at room temperature and above is cadmium zinc telluride (CdZnTe, or CZT). Silicon and high-purity germanium detectors require cryogenic cooling to function properly which reduces their portability, however CZT can be used in a compact device which operates at room temperature or higher. CZT fulfills all of the requirements of a good high energy gamma-ray detector material, however it has one major issue: high production costs, due to issues with the crystal growth process [3, 4]. Due to complications in the crystal growth, it is highly difficult to produce large quantities of detector-grade CZT, and even more difficult to produce large-volume crystals of detector-grade CZT. This reduces the amount and quality of detector grade CZT crystals. This also leads to an exploration of methods which increase the efficiency of CZT detectors, since large volume detector grade crystals are difficult to produce.

## 1.2 DISSERTATION OVERVIEW

This work contributes to four key areas of ongoing research to make CZT detectors more cost effective and widespread in its use. First, a method of CZT crystal growth developed in the laboratory at USC is explored. This new method produces detector grade CZT crystals, yet reduces the complexity of the growth procedure compared to currently used techniques. Second, passivation techniques are explored for their effectiveness at improving detection properties on these grown crystals. Surface conditions of CZT detectors are extremely important, and improve detector performance when the surface is treated with a passivation layer. Third, defect studies are carried out on CZT, to determine the key areas of improvement on the CZT crystals grown using this unique method. Fourth,

unique detector structures were fabricated and characterized to explore the effects of detector fabrication on the detection performance of the grown CZT crystals.

This dissertation is divided into seven chapters. Chapter 1 provides a background and review of the properties of CZT. A brief review of the current challenges present in CZT research is also provided.

Chapter 2 discusses the unique crystal growth method employed for CZT in this work, the tellurium solvent method. An overview and comparison of previous growth methods with the solvent method growth is provided. Furthermore, an overview of precursor preparation through zone refining and ampoule preparation through carbon coating is reviewed and the processes used in our laboratory are discussed.

Chapter 3 details characterization performed on the CZT crystals grown using the unique solvent method. The characterization includes analysis of the stoichiometry of the grown CZT (including the ratio of zinc to cadmium), optical characterization using UV-Vis and infrared imaging, and electrical characterization. Techniques such as Current-voltage (I-V) and resistivity measurements determine if the grown crystals can be utilized for radiation detection.

Chapter 4 describes surface modification of the grown CZT crystals using sulfur and selenium ion passivation. Surface states present on CZT crystals strongly influence the performance of fabricated CZT detectors, which can be affected and improved using surface passivation. Once the CZT surface is passivated, characterization is performed using x-ray photoelectron spectroscopy (XPS). Sulfide passivation is analyzed for effectiveness in passivating electrically active surface states resulting in the improvement in performance of nuclear detectors fabricated from CZT crystals. I-V characteristics are

tested before and after sulfur passivation to determine the effect of this surface modification on the electrical properties of the grown CZT crystals.

Chapter 5 involves defect characterization of the grown CZT crystals to determine the type and amount of defects present. Since the crystal growth method employed is unique, defect analysis is required to determine what defects are present in the grown crystals, and how they may be affecting performance of fabricated detectors. Defect characterization is performed using electron beam induced current (EBIC), thermally stimulated current (TSC), and etch pit studies.

Chapter 6 focuses on detector fabrication and characterization using our in-house nuclear radiation detection system. Despite improvements in CZT's electron and hole mobility and lifetime, a large gap between the electron and hole transport properties persists. This is remedied by using different detector geometries which eliminate the poor hole transport properties from the acquired detection spectra, such as a Frisch collar and pixel geometry. The fabricated detectors are characterized using Pulse Height Spectra (PHS) measurements, electron and hole mobility measurements, and electron mobility-lifetime product ($\mu\tau_e$) measurements. Further analysis of fabricated detectors was performed using biparametric correlation method.

Finally, Chapter 7 concludes the research presented in this work, and provides suggestions for future work.

## 1.3 INTRODUCTION TO RADIATION DETECTION MATERIALS AND DEVICES

On the market today, very few nuclear radiation detector semiconductor materials exist which can provide a compact, portable, lightweight gamma-ray detector which can be field deployed easily. In order to perform as a radiation detector, the material must be

able to determine the type of radiation present, such as alpha particles, gamma-rays, beta particles, etc., and precisely pinpoint the energy emitted by the radiation source. In order for a semiconductor nuclear detector to perform this work, it must be able to 1.) absorb the nuclear radiation, 2.) generate charge pairs which will represent the information about the nuclear radation, and 3.) transport the charge pairs through the detector material to the read-out electrodes and, subsequently, the front-end electronics. Figure 1.1a shows a simple schematic of the operation of a semiconductor nuclear detector.

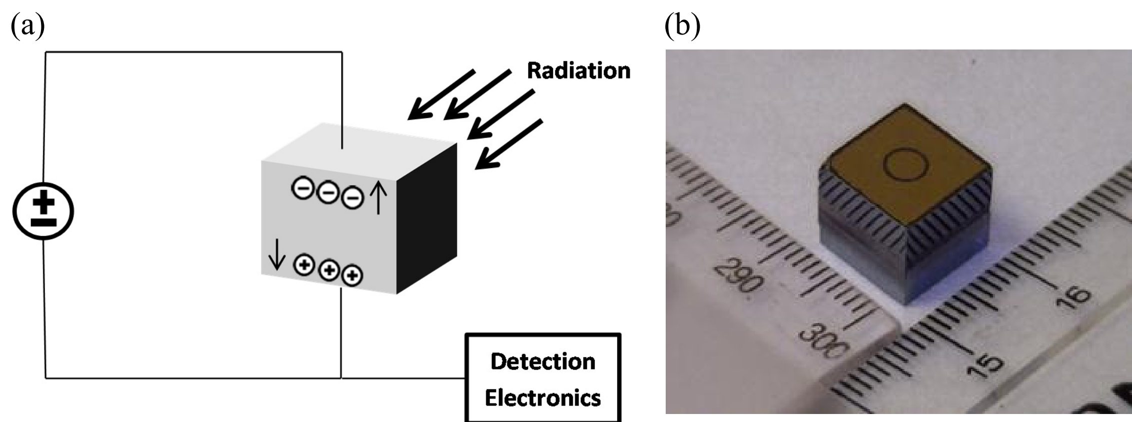


Figure 1.1. (a) Simple schematic of the operation of a semiconductor nuclear detector, and (b) a 1 $cm^3$ CdZnTe detector fabricated in the laboratory.

In order for a semiconductor material to function as an X-ray and gamma-ray detector, it must satisfy several requirements which are listed in Table 1.1. First, the semiconductor must be capable of stopping X-rays and gamma-rays, which requires that the material have a high atomic number and density. This allows the material to have a greater probability of the radiation interacting with the material. Second, the material must have a high resistivity, which reduces the detector leakage current and therefore the amount of noise present in the entire detection system. Third, the material should have good charge transport properties, such as a high mobility lifetime product ($\mu\tau$) and a high mobility ($\mu$)

for both electrons and holes. A detector material with poor charge transport properties will not be able to transport charge generated due to irradiation to the readout contacts without information being lost. In order to determine the difference between radiation with various energies present in the detection spectrum, a high energy resolution will ensure distinct peaks for different energies. More information on this is discussed in Chapter 6. Finally, the detector material must have a high band gap of about 1.5 eV or greater, to reduce the effects of thermal noise on the detection spectrum.

Table 1.1. Ideal qualities of a semiconductor gamma-ray and X-ray detector.

| Qualities | Requirements |
|---|---|
| Capable of Stopping X-Rays and Gamma-Rays | High Atomic Number and Density |
| High Resistivity | $\geq 10^{10}$ Ω-cm |
| High Mobility Lifetime Product (μτ) | $\geq 10^{-3}$ $cm^2/V$ |
| High Mobility | $\geq 1000$ $cm^2/V.s$ |
| High Energy Resolution | ~ 0.5 % or better for High Energy Gamma Rays (i.e. 662 keV) |
| High Band Gap to reduce thermal noise | 1.5 eV or greater |

For modern day X-ray and gamma-ray detection, the primary semiconductor materials available for commercial purchase are silicon (Si), high-purity germanium (HPGe), mercuric iodide ($HgI_2$), and cadmium telluride (CdTe). Germanium has a high atomic number, can be produced in large volumes (> $10 cm^3$), and has excellent energy resolution of 0.2% using a benchmark 662 keV gamma-ray irradiation [5]. However, in order to obtain good energy resolution, germanium detectors must be cryogenically cooled

to liquid nitrogen temperatures (~77K), due to its low band gap of 0.67 eV [6]. Silicon has also been used commercially as an X-ray detector. However, silicon cannot be used effectively as a gamma-ray detector due to its low atomic number, making it ineffective at stopping gamma-rays. Furthermore, silicon requires cooling due to its low band gap (~1.1eV). In addition, mercuric iodide has a high atomic number and wide band-gap, however both electron and hole mobilities are very poor [7], which restrict its use as a high energy gamma-ray detector. Mercuric iodide also requires encasement, since it is hygroscopic and a soft material. CdTe is also another prevalent choice for nuclear detection due to its good charge transport properties, however the bandgap of CdTe cannot be tuned above 1.4 eV, and it has a resistivity of $\sim 10^8 - 10^9$ Ω-cm, which is less than ideal for noise performance reasons [8]. Other popular non-semiconductor materials exist on the market, such as sodium iodide (NaI), however NaI suffers from very poor resolution [5]. Because of these limitations on X-ray and gamma-ray detectors available on the market, materials such as CZT are being proposed as strong alternatives to currently available detector materials.

Cadmium zinc telluride is a direct-bandgap ternary semiconductor comprised of the binary compound cadmium telluride (CdTe) which is alloyed with zinc. As a nuclear detector material, it has several advantages over silicon and germanium, which can be seen in Table 1.2. First, it has a high atomic number, with tellurium having the highest atomic number of 52. This means CZT will have the necessary stopping power to absorb high energy gamma-rays. Second, it is able to operate as a nuclear detector below, at, and above room temperature (~300K). This allows a portable detector device to be made from CZT, without the use of heavy dewars or liquid nitrogen. Third, it has a tunable bandgap from

1.5 to 2.2 eV, depending on the concentration, x, of zinc present in the $Cd_{1-x}Zn_xTe$. Fourth, it has a high resistivity of around $10^{10}$ Ω-cm, which reduces noise due to leakage current. Fifth, it has good electron charge transport properties, meaning that electrons are able to travel through the CZT bulk material without being lost or trapped.

Table 1.2. Material properties of CdZnTe.

| CdZnTe Properties | Specifications |
|---|---|
| Tunable Band Gap | 1.5 to 2.2 eV at 300K |
| High Atomic Number | Cd: 48<br>Zn: 30<br>Te: 52 |
| High Resistivity | ≥ $10^{10}$ Ω-cm |
| High Electron Mobility Lifetime Product ($\mu\tau_e$) | $10^{-2}$ - $10^{-3}$ $cm^2/V$ |
| High Electron Mobility | ≥ 1000 $cm^2/V.s$ |
| Operates at Room Temperature and above | 300 K |
| Issues | Low Yield, High Price, Poor $\mu\tau_h$ |
| Poor Hole Transport Properties | $\mu\tau_h$ : ~$10^{-5}$ $cm^2/V$<br>$\mu_h$ : ~50 $cm^2/V.s$ |

Table 1.3 shows a comparison of several important properties of CZT with some semiconductor materials commonly employed for nuclear detection in a research setting. CZT compares favorably with Si and Ge by having a higher atomic number, higher density, higher band gap, and higher resistivity than Si and Ge. While these material properties are favorable, CZT does suffer from several issues preventing widespread market adoption. CZT suffers from poor hole transport properties, including a low hole mobility ($\mu_h$) and

low hole mobility-lifetime product ($\mu\tau_h$). Furthermore, the transport properties for electrons and holes are different, with the hole mobility-lifetime product being several orders of magnitude less than electron mobility-lifetime product. This means that when electron-hole pairs are generated due to radiation interaction, electrons are more likely to reach the readout electrodes of the detector without being lost or trapped than holes. Since detection signals are a composite of both the electron and hole signal, the resulting spectrum will yield incomplete information about the incident radiation. In addition to the poor hole transport properties, CZT also has very low crystal growth yields for detector-grade CZT, due to defects and inhomogeneity. The result of this is that it is very difficult, and therefore very expensive, to produce large single crystals of detector grade CZT material.

Table 1.3. Physical properties of popular X-ray and γ-ray semiconductors at T = 25°C [6]

| Material | Si | Ge | CdTe | $Cd_{0.9}Zn_{0.1}Te$ | $HgI_2$ |
|---|---|---|---|---|---|
| **Crystal Structure** | Cubic | Cubic | Cubic (ZB) | Cubic (ZB) | Tetragonal |
| **Growth method*** | C | C | THM | HPB, THM | VAM |
| **Atomic Number** | 14 | 32 | 48, 52 | 48, 30, 52 | 80, 53 |
| **Density ($g/cm^2$)** | 2.33 | 5.33 | 6.20 | 5.78 | 6.4 |
| **Band gap (eV)** | 1.12 | 0.67 | 1.44 | 1.57 | 2.13 |
| **Pair creation energy (eV)** | 3.62 | 2.96 | 4.43 | 4.6 | 4.2 |
| **Resistivity (Ω cm)** | $10^4$ | 50 | $10^9$ | $10^{10}$ | $10^{13}$ |
| **$\mu_e\tau_e$ ($cm^2/V$)** | >1 | >1 | $10^{-3}$ | $10^{-3} – 10^{-2}$ | $10^{-4}$ |
| **$\mu_h\tau_h$ ($cm^2/V$)** | ~1 | >1 | $10^{-4}$ | $10^{-5}$ | $10^{-5}$ |

* The more common growth methods: C = Czochralski, THM = traveler heater method, HPB = high-pressure Bridgman and VAM = vertical ampoule method

Despite the issues surrounding CZT and its use as a widespread gamma-ray and X-ray detector, CZT is a proven material with several decades of research showing its effectiveness [6, 9]. With further study and continued research, it is hoped that CZT will

become more cost effective to produce and use as a replacement for commercially available yet cumbersome gamma-ray and X-ray detector materials.

# CHAPTER 2: CRYSTAL GROWTH

## 2.1 OVERVIEW

Single crystal growth is the act of transforming material from a variety of different phases into the solid phase, resulting in an ordered crystal lattice. If materials are able to melt, or become a liquid at a certain temperature, then it is possible to perform crystal growth by performing a liquid to solid phase transition in order to grow a material with an ordered lattice structure. The melting temperature of Cd, Zn, and Te at a pressure of 1 atm are 321.1°C, 419.6°C, and 449.5°C respectively, meaning that all of these precursor materials can be melted to form the ternary compound CdZnTe using a liquid to solid phase transition.

In order to form the compounds CdTe and CZT, the temperature must be well above the melting point of the compounds themselves as well as the precursor elements, in order to form the covalent bonds that hold together the elements within the lattice structure. As seen in the binary phase diagram in Figure 2.1, CdTe has a melting point of 1096°C for an atomic ratio of 50% Cd to 50% Te. As the atomic ratio of Te is increased above 50% (signifying excess Te), the growth temperature of CdTe will decrease accordingly. The growth temperature will also decrease if more than 50% of Cd is present in the melt during crystal growth. This is because CdTe is capable of dissolving in both Cd and Te while in the liquid phase. Because CdTe will dissolve in Cd or Te if there is excess amounts of the

element than necessary to create CdTe, the the growth temperature of CdTe will decrease, as seen in Figure 2.1 [10].

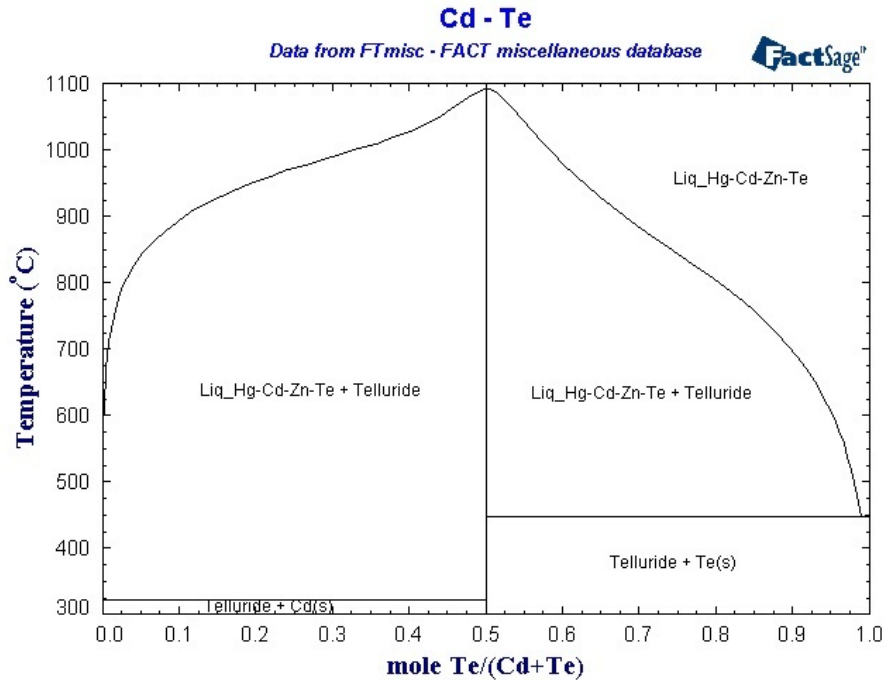


Figure 2.1. Phase Diagram for CdTe [11].

In order to grow cadmium zinc telluride, CdTe is alloyed with zinc, to create a ternary compound consisting of CdTe with Zn atoms occasionally replacing Cd atoms in the lattice structure. The ratio of Cd:Zn is commonly 90%:10% for detector grade CZT crystals [9]. The resulting ternary compound is referred to as $Cd_{0.9}Zn_{0.1}Te$. As seen on the ternary phase diagram shown in Figure 2.2, the melting point of $Cd_{0.9}Zn_{0.1}Te$ is ~1120°C.

New growth techniques are extremely invaluable for the development of CZT as a room-temperature semiconductor gamma-ray spectrometer material. Defects and polycrystallinity make CZT very expensive to produce and use [9]. Issues with oxidation and impurities become more pronounced as growth temperatures increase [10, 12]. This chapter details the preparation of precursor materials, preparation of the quartz ampoules

holding the precursor materials, an overview of issues with previous growth methods, and details of the solvent growth method developed in our laboratory.

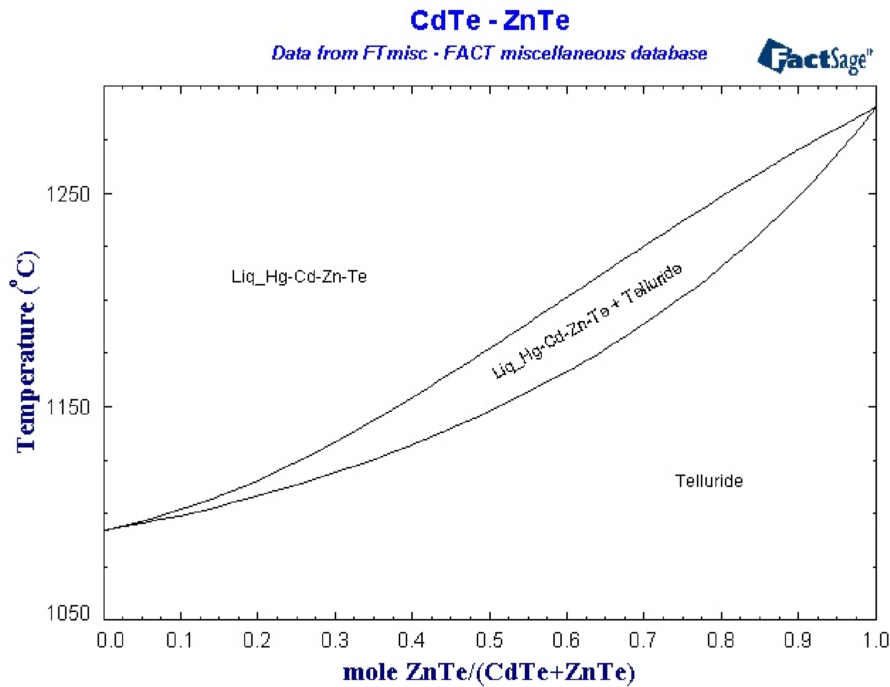


Figure 2.2. Phase Diagram for CdZnTe. Top line indicates liquidus temperatures, bottom line indicates solidus temperatures [11].

## 2.2 PRECURSOR PREPARATION BY ZONE REFINING

Almost all semiconductor-based devices require high purity precursor materials. Impurities, big or small, have a very strong negative impact on consistent performance. However, high purity precursors are either very expensive, or commercially unavailable. Purification of the precursors for CZT can be performed in-house using a process called Zone Refining, to satisfy the need to produce high quality precursor materials. Zone refining is a technique developed to purify semiconductor materials in the 1950's by Bell Laboratories [13]. This technique relies on the idea that impurities are distributed

differently in their solid and liquid phases at equilibrium. If a small zone of a material is melted with the remainder of the material remaining solid, impurities will collect in this molten zone as it moves through the solid. These impurities will eventually collect into one end of the material, and the remainder of the material will be highly pure [14]. The relationship governing how pure a material can be made is given by the following equation:

$$k = \frac{C_s}{C_l} \qquad 2.1$$

where k is the segregation constant of the impurity relative to its solid and liquid states, $C_s$ is the impurity concentration in the solid phase, and $C_l$ is the impurity concentration in the liquid phase. The segregation constant k refers to the concentration of impurities in the solid crystal compared to that of the melt, or the solubility of impurities in the melt versus the solidified crystal. For cases where $k < 1$, impurities prefer to stay in the melted portion of the material being purified. If $k < 1$, the material can be purified using zone refining, and the closer k is to 0, the easier it is to purify using this method. Furthermore, as more zone passes are made over the material in question, further purification of the material is achieved. Figure 2.3 illustrates this process, and the enhanced effect of multiple zone passes on any given material. For 10 zone passes along a material, more impurities are segregated to one end of the ingot than if 1 or 5 passes were made along the ingot. Just as with the impurities, the portion of the ingot containing pure precursor material is purified further due to more zone passes.

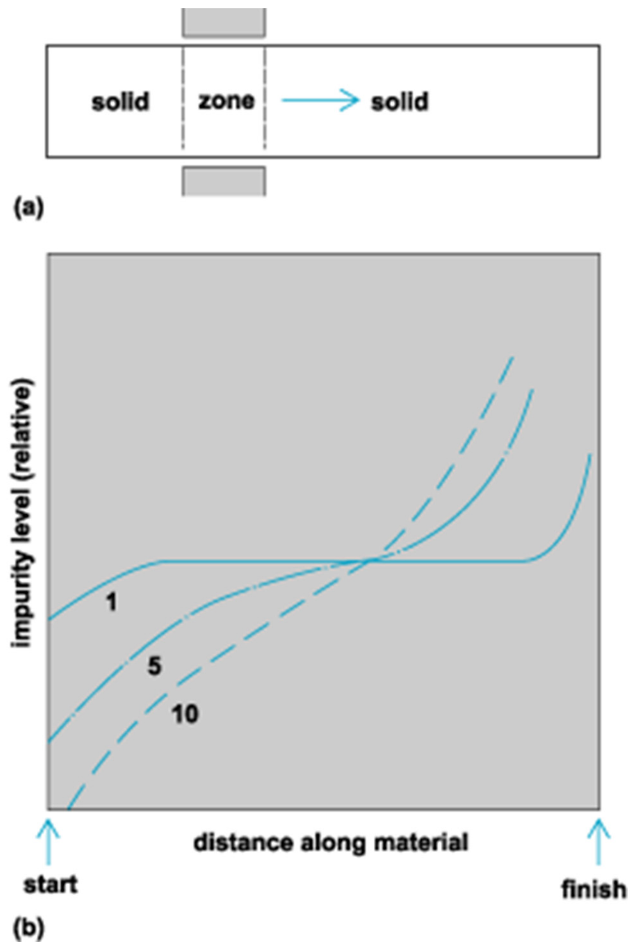


Figure 2.3. (a) Typical zone refining furnace schematic, showing the solid and molten portions of the material. (b) Effect of the number of passes (1, 5, and 10) over the material, and its effect on impurities. [15]

A zone refining system was developed here in the laboratory at USC in order to purify semiconductors and metals. The system uses a single zone furnace mounted on a track actuator, which is controlled using an Arduino. The Arduino is an electronics microcontroller board which can be programmed to perform control of motors and devices through the C programming language. The Arduino in this case is connected to an H-Bridge control setup, which is designed to have the track actuator selectively move forward or reverse. Speed control of the track is implemented using impulses sent to the motor at various intervals. The Arduino is autonomous, and will run without human intervention.

To facilitate a human interface to the Arduino, it has been programmed to connect to PC software developed in Visual Basic .net to allow for human control of the system.

Table 2.1. Glow Discharge Mass Spectroscopy (GDMS) impurity analysis for zone refined Cd, Zn, and Te. Impurity concentration in parts per billion. ND = Not detected.

| GDMS Analysis (Cd) | | GDMS Analysis (Zn) | | GDMS Analysis (Te) | |
|---|---|---|---|---|---|
| Impurity Elements | Conc. (ppb) | Impurity Elements | Conc. (ppb) | Impurity Elements | Conc. (ppb) |
| Cd | Major | Zn | Major | Te | Major |
| Li | ND | Li | ND | Li | ND |
| O | < 5 | O | < 5 | O | < 5 |
| Na | 4 | Na | 4 | Na | ND |
| Al | ND | Al | ND | Al | ND |
| Si | 18 | Si | 9 | Si | 8 |
| Fe | ND | Fe | ND | Fe | ND |
| Cu | 18 | Cu | 5 | Cu | 6 |
| Mn | ND | Ni | ND | Ni | ND |
| Ni | ND | Co | ND | Co | ND |
| Co | ND | Cr | ND | Cr | ND |
| Zn | < 8 | Mn | ND | Mn | ND |
| Cr | < 4 | Te | < 4 | Ca | ND |
| Sn | < 4 | Ca | ND | Se | < 7 |
| Ca | ND | Sn | ND | Sn | < 5 |
| Te | 7 | Cd | 4 | Cd | 4 |
| Hg | ND | Tl | ND | Tl | ND |
| Tl | ND | Pb | ND | Pb | ND |
| Pd | ND | Hg | ND | Hg | ND |
| Ba | ND | Rb | ND | Rb | ND |
| Rb | ND | Pd | ND | Pd | ND |
| Pd | ND | Ba | ND | Ba | ND |

Figure 2.4. Typical zone refined precursor material produced in the laboratory, with impurities segregated to left side of the ampoule, and pure precursor material on right side.

The zone refining was initiated by sealing the precursor materials in a quartz ampoule, and suspended over the track actuator in the horizontal zone refining furnace. 6N (or 99.9999% pure) cadmium, zinc, and tellurium were used as the precursor materials for zone refining. The furnace was ramped up to slightly above the melting point of each precursor material (melting temperatures: 321.1°C for Cd, 419.6°C for Zn, and 449.5°C for Te) at a rate of 1°C per minute. The track actuator moved the furnace along the ampoule at a rate of 30mm per day, and the furnace made 40 passes from one end of the ampoule to the other. Glow discharge mass spectroscopy (GDMS) analysis was performed on the zone refined (ZR) precursor materials (Cd, Zn and Te). Table 2.1 shows the impurity concentration results of the GDMS analysis performed on the precursor material. The purity of the precursor materials used for CZT crystal growth has been shown to impact the resulting CZT ingot quality [16]. According to the GDMS data shown in Table 2.1. Glow Discharge Mass Spectroscopy (GDMS) impurity analysis for zone refined Cd, Zn, and Te. Impurity concentration in parts per billion. ND = Not detected.Table 2.1, the precursor materials prepared in our laboratory have several parts per billion of common impurities or less. A photograph of a typical zone refinement run performed in our

laboratory is shown in Figure 2.4, with impurities segregated to the left end of the ampoule, and pure precursor material on the right side of the ampoule.

## 2.3 Carbon Coating of Quartz Ampoules

Carbon coating is a process which covers the inside of a quartz ampoule with a thin coating of carbon. This is done to protect the precursor materials used for crystal growth, as well as the resulting ingot, from interaction with the surface of the quartz. The most common issue with CZT crystal growth is the tendency of Cd to adhere to the inside wall of the quartz ampoule and react with the $SiO_2$ material. To prevent this, and to trap any residual oxygen or water within the ampoule walls in the carbon layer, carbon coating is used [12].

To fulfill the desire to grow detector-grade CZT crystals which benefit from these advantages, a carbon coater system was developed here in our laboratory at USC, based on prior work detailing this type of system [12]. Several modifications were made to the prior work. The basic instrumentation and piping system used for flowing argon and hexane into the quartz ampoules was reimplemented in our laboratory, as seen in Figure 2.5. A new method of housing the quartz ampoules was required, in order to allow ordinary quartz ampoules, which can be used directly in a crystal growth furnace, to be placed in the carbon coating system. The system developed in our laboratory encases the quartz ampoules in a stainless steel piping system, which allows ampoules to be held within and coated, and easily removed without harmful fumes escaping the encasement, as seen in the schematic in Figure 2.6. The inlet gas line supplies argon containing hexane, which is burned within the furnace and coats the ampoule wall with carbon. This inner pipe is welded to the encasement, which allows exhaust to flow into a small chamber which allows a flexible

hose connection to a fume hood. See Appendix A for the mechanical design details of this encasement setup. The full carbon coating system can be seen in Figure 2.7.

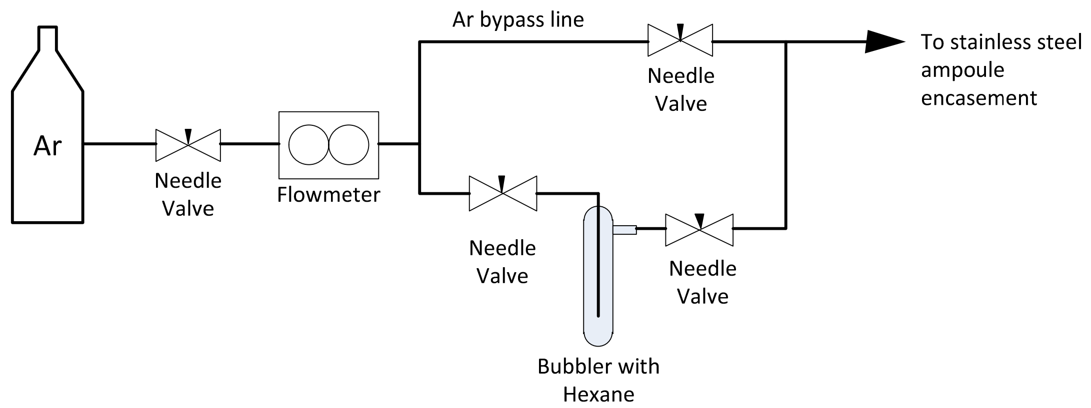


Figure 2.5. Schematic diagram of carbon coating system developed in our laboratory for coating quartz ampoules.

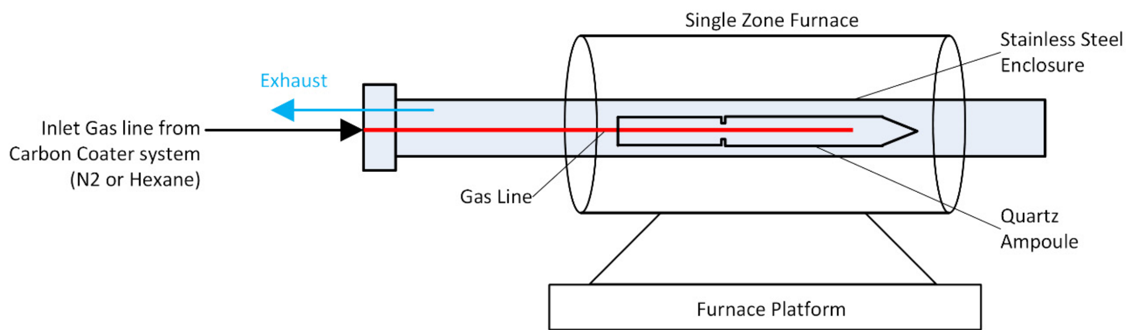


Figure 2.6. Schematic diagram of the furnace end of the carbon coating system, showing the inlet, ampoule encasement, and exhaust for the system.

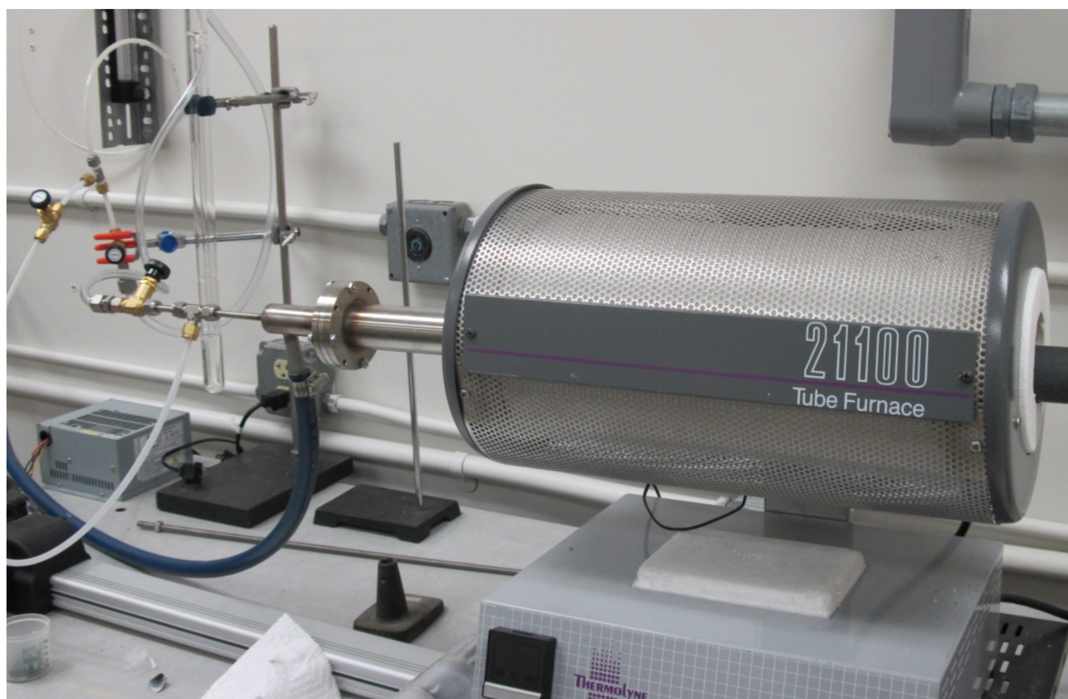


Figure 2.7. Carbon Coating system for quartz ampoules, installed in the laboratory.

Prior to carbon coating, quartz ampoules used for crystal growth are rinsed using acetone, methanol, and de-ionized water. After this rinsing process the ampoules are etched using 10% hydrofluoric acid, and rinsed using de-ionized water several times. Ampoules were then loaded into the stainless steel encasement, and purged with argon for 15 minutes prior to operation of the carbon coating setup. For carbon coating, the furnace is ramped up to 800°C at a rate of 1°C per minute, under argon flow. After 15 minutes at 800°C, normal argon flow is stopped and argon flowing through the hexane bubbler is enabled for 1 hour and 30 minutes at a flow rate of 15 mL/minute, to achieve approximately 1 µm of carbon thickness on the ampoule wall [12]. After coating, normal argon flow is resumed, and the ampoule is purged of hexane gas for 30 minutes. The carbon coated ampoule is then annealed at 1100°C for 1 hour. Figure 2.8 shows a typical 1” diameter quartz ampoule after the carbon coating and annealing procedure has been carried out. The coated

ampoules are nearly opaque, and the carbon coating in the inner wall has a graphite-like dark color associated with it.

Figure 2.8. Typical quartz ampoule after carbon coating and annealing process is completed.

## 2.4 Prior Growth Techniques

Detector-grade CZT is typically grown by melt growth techniques or solution growth techniques. Melt growth techniques involve melting the material, and then crystallizing the material using changing pressure, temperature, or a combination of the two. CdTe and CZT single crystals have historically been grown using the Bridgman method and the travelling heater method (THM) [6].

The Bridgman method has been used successfully to grow detector grade CZT crystals during the past two decades. The Bridgman technique uses a “hot” and “cold” zone to create a temperature difference within a furnace, as visualized in Figure 2.9 [10]. The hot zone is kept at a temperature above the melting point of the growth material. The precursor material used to create the material is sealed within a crucible or ampoule and placed within the furnace, along with a seed crystal. The seed crystal is a crystal of known orientation placed at the base of the crucible or ampoule used for crystal growth, which is used to facilitate crystal growth in the same orientation as the seed crystal. The precursor

material is then melted in the hot zone, and translated into the cold zone by motion. Since the melting point of the material will be between the hot and cold zone of the furnace, the material will solidify when moved through the temperature gradient of the furnace. The Bridgman method can be performed in either horizontal or vertical configurations. Two types of Bridgman methods have been employed for CZT: the high pressure Bridgman method (HPB) and the low pressure Bridgman method (LPB).

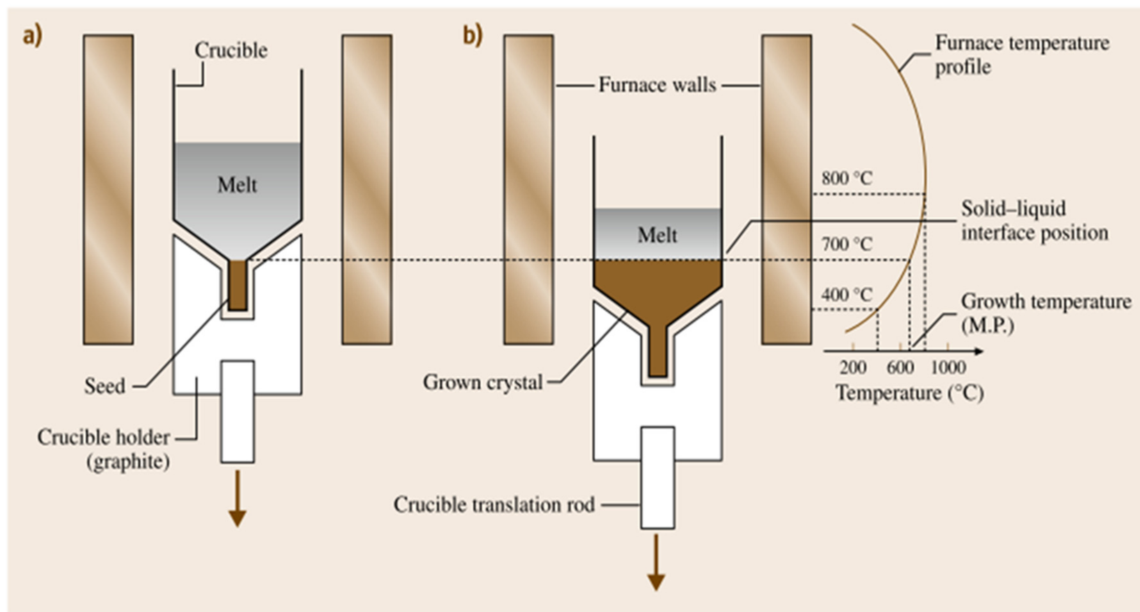


Figure 2.9. Schematic diagram of a vertical Bridgman crystal growth process (a) in the hot zone and (b) while moving through the cold zone.

For both Bridgman methods, CZT is grown using stoichiometric $Cd_{0.9}Zn_{0.1}Te$ atomic proportions, with a hot zone temperature of about 1100°C [9]. Quartz and graphite are commonly used materials for use as crucibles, due to their resistance to high temperatures and pressures. Typical growth rates are in the range of 1mm/hour, with a temperature gradient of about 1.5°C/cm [9]. High pressure Bridgman methods typically employ 5 MPa of argon pressure [17], whereas low pressure Bridgman methods evacuate the crucible/ampoule to an ultra-high vacuum (approx. $10^{-6}$ torr).

The HPB and LPB methods have been used extensively to grow detector grade CZT material, however these methods suffer from various defects, preventing widespread use of CZT as a room temperature semiconductor detector [9]. CZT crystals grown by HPB are inhomogeneous on the scale of a few centimeters, due to macro-defects such as small grain sizes. Furthermore, there are significant variations in the concentration of zinc present from one end of the ingot to another (known as zinc segregation) [6]. These issues mean that HPB results in 25% of an ingot yielding sizeable single-crystals, with only 10% of the ingot yielding detector-grade CZT [9]. The LPB method uses ampoules which are held under vacuum and sealed, which requires a simpler furnace setup than the HPB method. However, yields are similar to the HPB method [9]. Both methods suffer from large amounts of defects due to impurities introduced because of the high growth temperature.

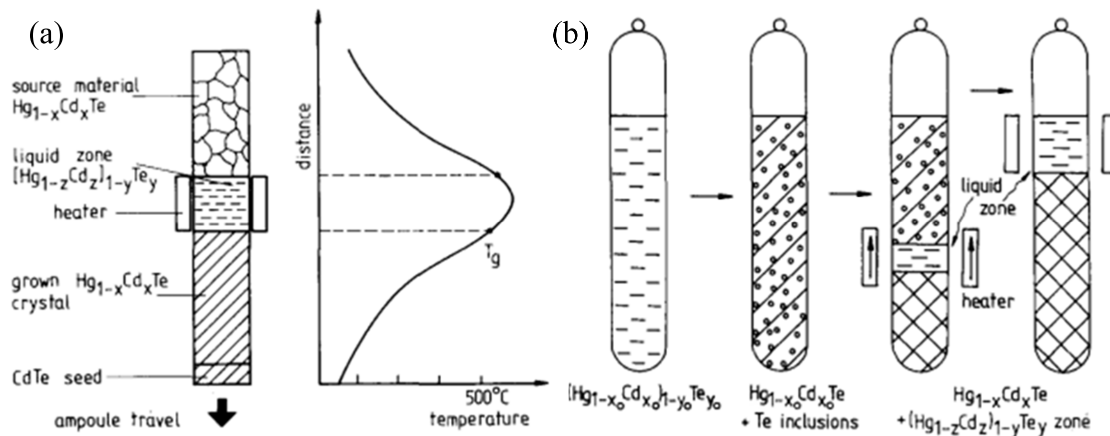


Figure 2.10. (a) Example schematic of THM crystal growth, used for HgCdTe. (b) THM crystal growth showing what happens to the precursor materials as the heater makes multiple passes through the ampoule. [18].

The travelling heater method is a crystal growth method which requires the material to be grown be dissolved in a compatible solution. In this method, a molten zone of material slowly migrates through a solid, homogeneous source material. Matter transport occurs

through convection and diffusion across the solvent zone due to the temperature gradient [18]. This method also purifies the source materials, due to the zone melting nature of this technique.

Although performance of CZT crystals grown by THM has been reported extensively [19] [20] [21], the exact details required to grow detector-grade CZT using THM has never been reported. Some details mentioned in this paragraph have been deduced from similar methods used for HgCdTe [18], as seen in Figure 2.10. CZT grown using the THM technique involves placing pre-synthesized $Cd_{0.9}Zn_{0.1}Te$, the dopant In, and additional tellurium as the solvent material within a quartz ampoule [19]. The ampoules are sealed under ultra-high vacuum, and placed in a furnace with a hot zone. Please note that growth temperatures for THM-grown CZT have not been reported by any organization. Before THM growth, another furnace heats and evenly distributes the tellurium throughout the material, to ensure all of the material is dissolved in Te. The material is then placed in the THM furnace, where the first pass of the heater moving through the material will collect the excess Te solvent distributed throughout the CZT. Multiple passes ensure all of the excess Te diffuses to one end of the ingot [18].

The travelling heater method has several advantages compared to the Bridgman method. It combines the low growth temperatures afforded by it being a solution growth method (see Figure 2.2), with the steady state conditions present between the dissolution of the source material before the heater and the crystal growth section after the heater (as in zone melting). The latter advantage ensures that Zn does not segregate, and is uniform throughout the ingot [21]. However, THM requires that a homogeneous source ingot be

used. In all reported instances for CZT, homogeneous $Cd_{0.9}Zn_{0.1}Te$ in stoichiometric proportions is used as a precursor material [20] [19] [21].

## 2.5 Solvent Growth Technique

### 2.5.1 Overview

The solvent growth technique, developed in our laboratory at the University of South Carolina [22], combines several aspects of THM and of the Bridgman method. In this method, the CZT precursors, dopants, and seed crystal are loaded into a quartz ampoule, and evacuated and sealed under ultra-high vacuum ($10^{-5}$ torr or higher). The ampoule is then loaded into a multi-zone furnace, and heated to a temperature above the melting point of the desired compound, in order to synthesize the precursor materials into CZT. For $Cd_{0.9}Zn_{0.1}Te$ with 50% excess Te, in the case of a solvent growth, this melting temperature is ~980°C [11]. Once synthesized, the ampoule is lowered into the cold zone at a very slow rate (3 mm/hr or less, depending on the temperature gradient of the furnace) [22]. This is done to ensure homogeneity of the material, and for single crystal growth of the ingot after the first pass through the furnace. Just as in THM, multiple passes through the hot and cold zones are used, in order to segregate excess Te from the rest of the CZT ingot.

This method has several advantages over THM and conventional Bridgman methods. Like THM, the solvent technique requires a lower growth temperature to form CZT, and also has the advantage of being self-purifying due to multiple passes through the melting zone, similar to zone melting. Like the Bridgman method, precursor materials can be synthesized and grown at the same time, unlike THM which requires pre-synthesized

precursors or a separate synthesis stage. However, not much information about defects has been gathered on the solvent growth method as of yet.

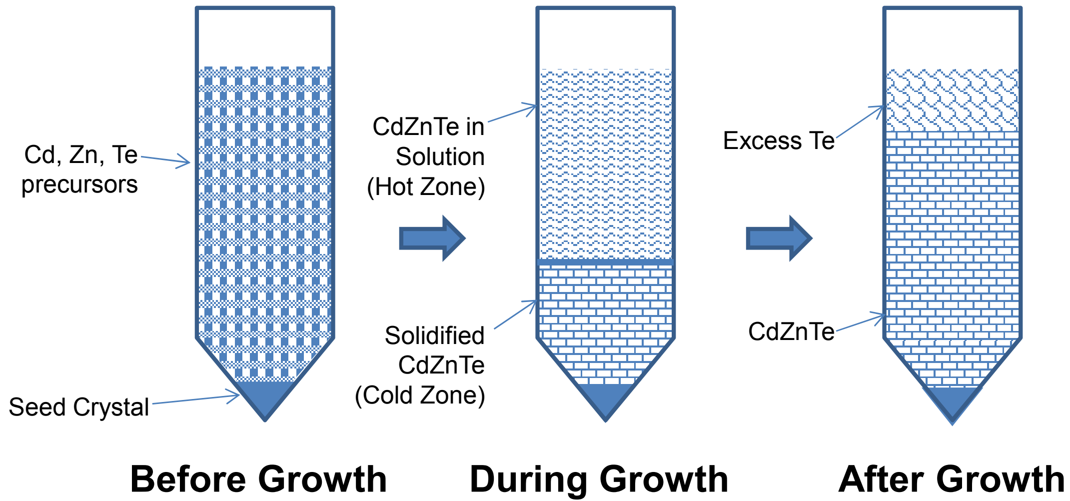


Figure 2.11. Schematic diagram of solution growth method for CZT.

### 2.5.2 Crystal Growth Furnace Modifications

Crystal growth is performed using a three-zone crystal growth furnace fabricated in-house in our laboratory at USC. A standard tube furnace was outfitted with custom pulling and rotation mechanics, and software and control circuitry was built and created to automate nearly all furnace functions. A Lindberg Blue three-zone tube furnace was fastened mechanically on the inside and stood up on its side to transform it into a vertical furnace. A mechanical puller was attached to a steel plate mounted inside the furnace to pull ampoules inside and out of the furnace. A rod was suspended over the furnace opening, and a 1 rpm geared rotation motor was attached to a welded coupling sitting on the rod to provide ampoule rotation. The rotation and puller motor was wired to an off-the-shelf

motor H-Bridge controller (Canakit UK1122 Bi-directional motor driver). The motor controller was then hooked up to an Arduino for automation and controls. The Arduino was coded to require input from a computer using a USB-RS232 connection before performing any operations, and would send status updates back to the computer during normal operation. The computer software was coded in Visual Basic .net, and provides full access to all features coded in the Arduino. All Arduino and PC code was written in-house. The resulting crystal growth furnace can be seen in Figure 2.12.

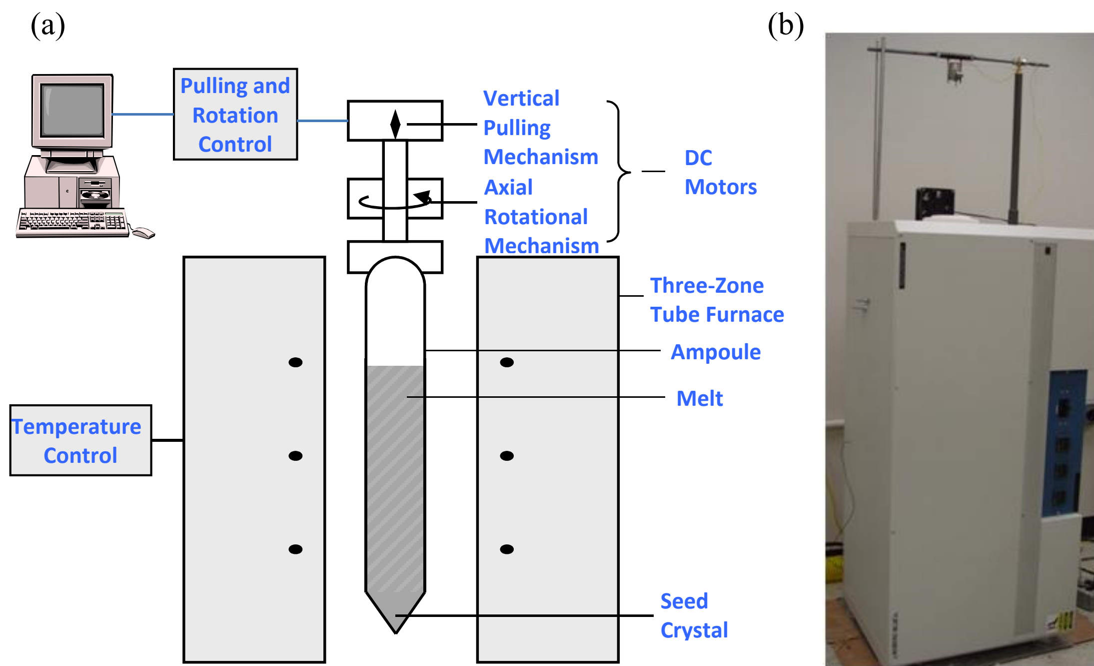


Figure 2.12. (a) Schematic of crystal growth furnaces built in our laboratory at USC, (b) photograph of one of our crystal growth furnaces.

However, the furnace in its initial form lacked the ability to perform multiple passes through the furnace, and was only capable of moving through the furnace one time. Crystal growth of CZT using the solvent method requires multiple passes to ensure proper crystal growth. Extra logic was added in the Arduino C code, as well as the Visual Basic .net GUI code to support additional passes through the hot zone. See Appendix B for more details

about the electronics and software. The quartz ampoule puller is now capable of precise movement through the multi-zone furnace, with constant monitoring using the developed PC software. Furthermore, unless a hardware failure occurs, the logic controlling the pulling and rotation mechanisms for the furnace is precise to several seconds, meaning that predicted times for a crystal growth cycle are equivalent to actual crystal growth times.

### 2.5.3 Experimental

Crystal Growth of CZT was performed using the in-house custom built modified growth furnaces shown in Figure 2.12, using the zone refined (~7N) Cd, Zn, Te, and In precursor materials. Ingots were grown with a 90:10 ratio of Cd:Zn in order to produce $Cd_{0.9}Zn_{0.1}Te$. The crystal growth was performed with 50% excess Te as a solvent, yielding a 36:4:60 at% ratio of Cd:Zn:Te precursors. These precursors, including In of 15 ppm as a dopant, were inserted into carbon coated quartz ampoules with a wall thickness of ~3.0 mm, and evacuated to a $10^{-6}$ torr vacuum. Ampoules were then sealed using an oxy-hydrogen torch to maintain an inert vacuum-sealed environment. Ampoules were then loaded into the growth furnace and attached to the puller and rotation system.

Crystal growth was performed by the solvent technique, using the growth profile shown in Figure 2.13. The furnace is ramped up to the peak growth temperature of 990°C in stages, with progressively slower ramp-up rates. The furnace is then held at 990°C for several hours, to ensure thorough melting of the precursor materials. Crystal growth is initiated by starting the puller and rotation system, which will lower the ampoule into the cold zone of 900°C at a rate of 2 mm/hr. The temperature gradient present between the hot and cold zones is ~3.9C/cm, and the gradient at the crystal growth zone is ~0.3°C/cm. The

CZT ampoules are rotated using accelerated crucible rotation [23] using 1 second pulses, at a rate of 12 rotations per hour.

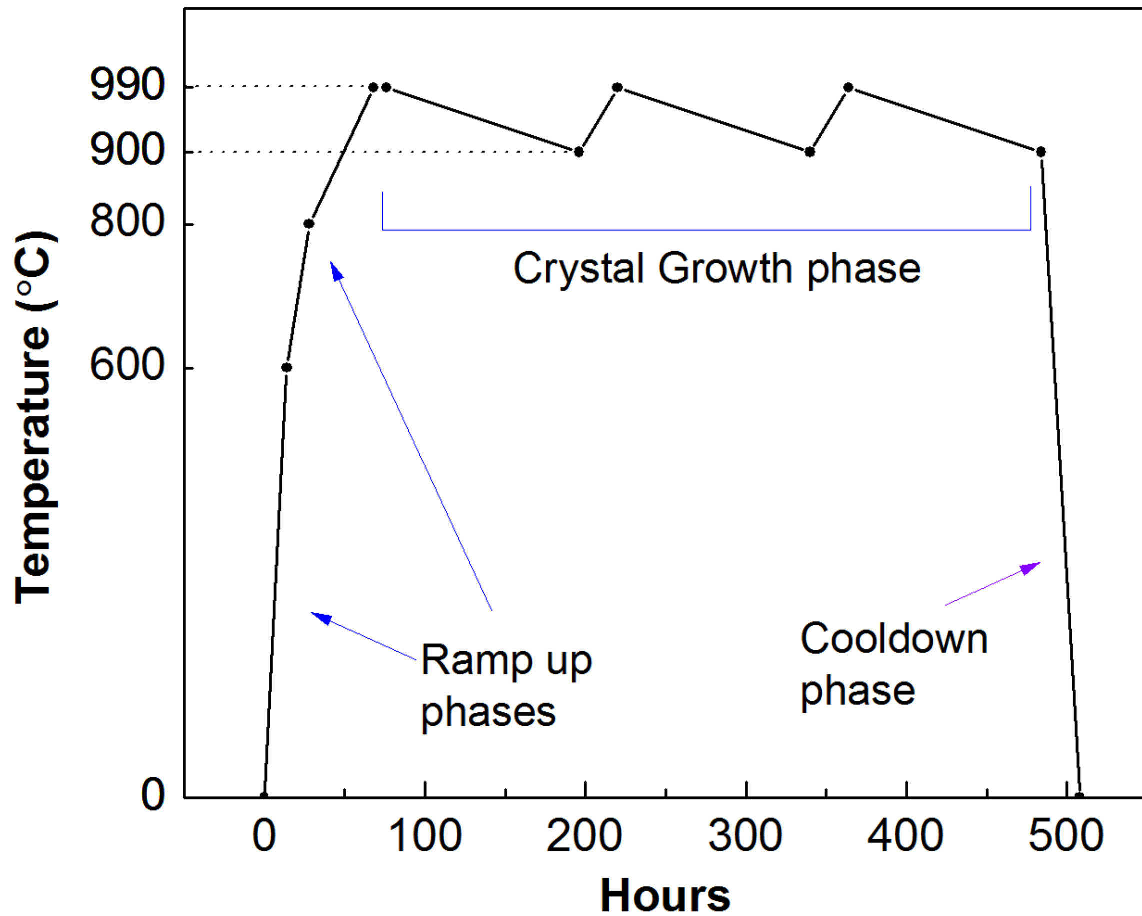


Figure 2.13. Typical crystal growth profile used for CZT, showing the ramp-up, crystal growth, and cooldown phases of the growth.

### 2.5.4 Results

After crystal growth, the quartz ampoules containing the grown CZT crystals were removed from the furnace. The quartz ampoules were carefully sawed open using a diamond wire-saw. Typical CZT ingots produced by this method can be seen in Figure 2.14.

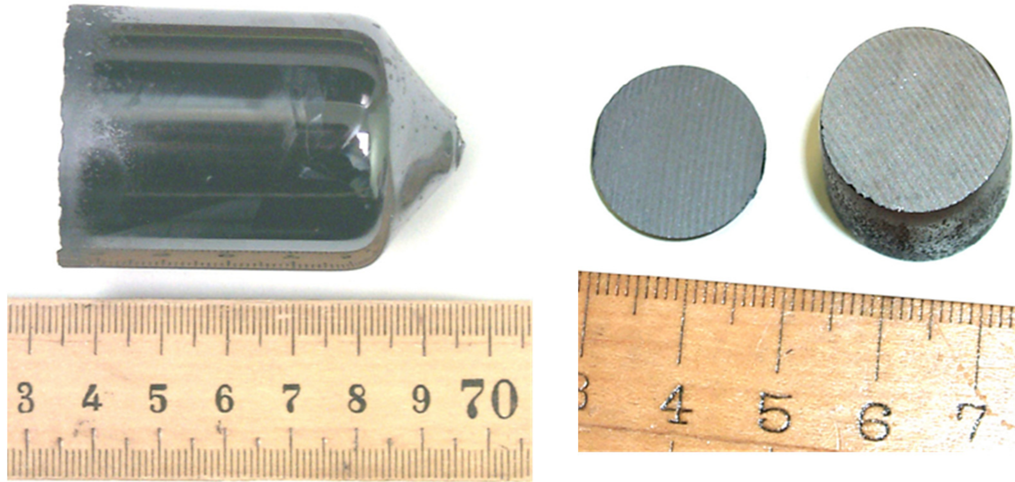


Figure 2.14. Images of a 2” CZT ingot produced in our laboratory.

## 2.6 CONCLUSION

In this chapter, the crystal growth process involved for growing CZT single crystals has been given. Preparation methods required prior to crystal growth, such as zone refining and carbon coating, have been reviewed and performed. Prior growth techniques for growing nuclear detector-grade CZT crystals have been examined for their effectiveness and drawbacks. A new growth technique, based on using tellurium as a solvent, has been shown and performed. In the next chapter, the preparation of CZT crystals will be examined, as well as optical, electrical, and structural characterization of the grown CZT crystals.

# CHAPTER 3: CRYSTAL CHARACTERIZATION

## 3.1 OVERVIEW

After successful crystal growth, the CZT crystals must be prepared through wafering and polishing, and characterized prior to use as nuclear detectors. Information such as the band gap of the crystals, stoichiometry, resistivity, and infrared imaging of tellurium defects provide information about the CZT crystals and their potential effectiveness as detectors. Information about the band gap of the CZT crystals is obtained using optical transmission of a thin wafer of CZT. Energy dispersive X-Ray analysis (EDAX) is used to determine the stoichiometry of the CZT ingot. Infrared transmission studies show the size and distribution of tellurium precipitates/inclusions, which have a negative effect on the electrical properties of CZT. Finally, electrical characterization through current-voltage (I-V) studies are performed, which reveals the resistivity of the grown CZT material.

## 3.2 CRYSTAL PREPARATION

When the crystal growth is complete, the CZT ingot is retrieved from the ampoule and cut into a regular square/rectangular sample shape using a wire-saw. The cut crystal is then polished using a series of sandpapers and buffing pads of different grits to achieve a mirror finish on all faces of crystal. Polishing the crystal provides a mirror finish via a series of variable grit sandpapers and ultimately microfiber pads. The art of polishing is

very essential in that it removes unwanted surface features that lead to higher leakage current and other unwanted effects. For example, 600 grit sandpaper is used to remove jagged surface features that are present after the diamond wire saw cutting procedure which gives the crystal a determinate shape. Once the surfaces of the crystal are rid of varied landscapes, then the idea is to work with decreasing grits to make ridges and certain other formations even smaller in depth till they disappear altogether. At this point, a couple of microfiber pads are used to buff the surfaces using 0.3 µm and 0.05 µm alumina powder respectively. After completing the polishing using 0.05 µm alumina powder on the microfiber pad, the crystal can then be cleaned thoroughly using an ultrasonicator. The crystal is then etched using a 2% Bromine-Methanol solution (Br-MeOH) for 1 minute and 30 seconds and then rinsed off with de-ionized water.

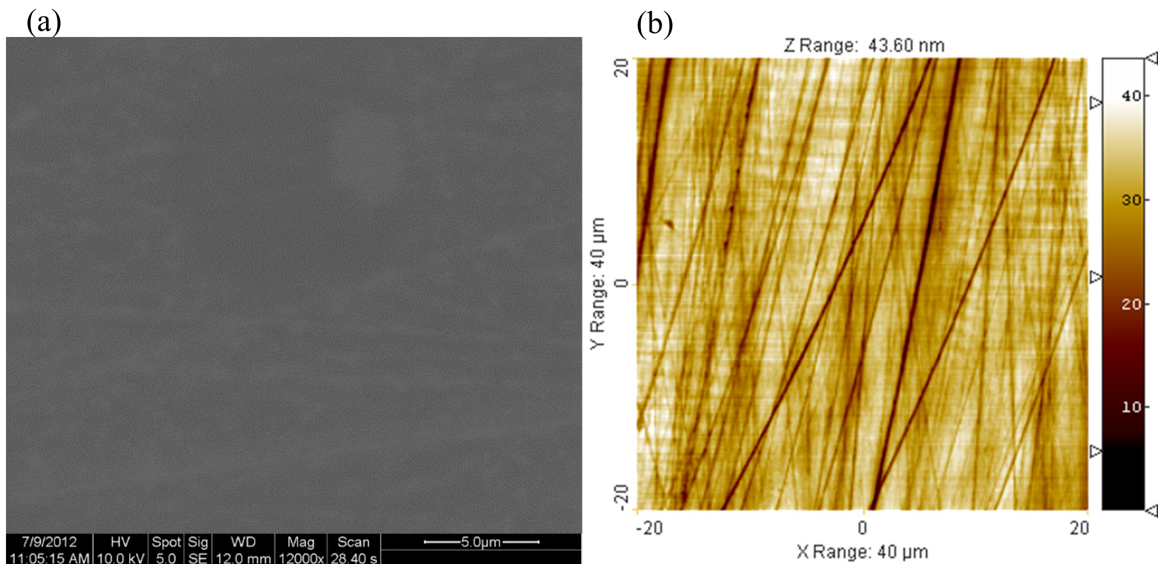


Figure 3.1. (a) SEM image and (b) AFM tapping mode image of the surface of an example of a CZT sample after polishing and etching.

Figure 3.1a shows an SEM image of the surface of an example CZT sample after polishing, while Figure 3.1b shows an AFM tapping mode topography image of the surface

of the sample. The scratches placed on the sample after polishing and etching are still present due to the use of 0.05 μm alumina powder, however are in the nanometer range. According to the AFM image, the average depth of the scratches is ~30 nm. Since there are no larger scratches present on the surface, the polishing and etching procedure used in our laboratory is a very effective method of preparing CZT semiconductor crystals for further use.

## 3.3 OPTICAL TRANSMISSION

Optical characterization was performed for the solution-growth CZT crystals using UV-Vis spectroscopy. For this study, a thin wafer of CZT was polished from a 1cm$^2$ sample down to ~30μm thickness, and transmission properties were measured from 750nm to 1500nm wavelengths.

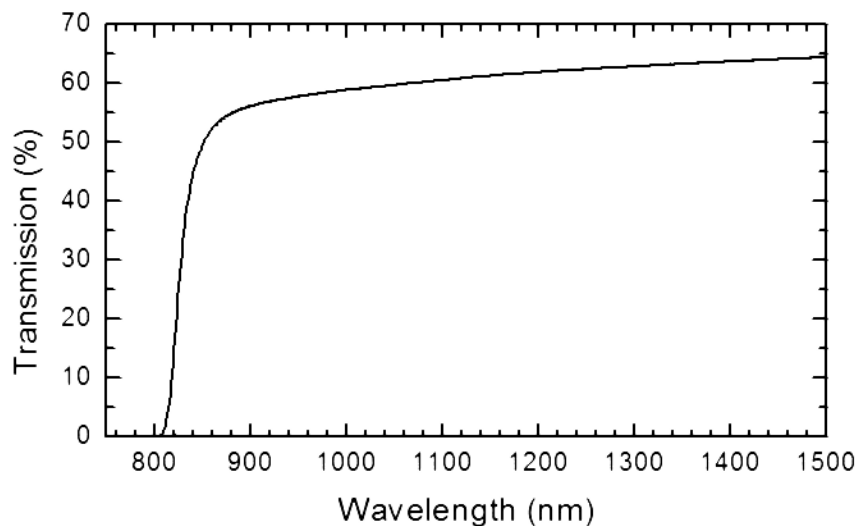


Figure 3.2. Optical transmission properties of a solution-growth CZT wafer.

Figure 3.2 shows the optical transmission properties obtained for the CZT wafer. The band gap energy can be calculated from the cut-off wavelength of the transmission spectrum, by using the following equation, also known as the Planck relation:

$$E = \frac{hc}{\lambda} \qquad 3.1$$

where h is Planck's constant, c is the speed of light, E is the band gap of the CZT crystal, and λ is the cut-off wavelength. For the optical transmission results shown in Figure 3.2, the band gap was calculated to be ~1.55 eV. This band gap is in the correct range for $Cd_{0.9}Zn_{0.1}Te$ [9], as well as for an ideal semiconductor nuclear detector, as seen in Chapter 1.

## 3.4 Energy-Dispersive X-Ray Spectroscopy

In order to determine if the grown CZT crystals are detector-grade, stoichiometry data must be acquired to ensure the proper ratio of Cd:Zn:Te are present within the crystals. Historically, stoichiometry has been a significant issue with CZT due to the segregation of Zn from the rest of the ingot [24]. This means that there is a strong possibility of Zn being in-homogeneously distributed through the grown ingot. However, methods of crystal growth similar to the solvent-growth technique, such as the travelling heater method, report homogeneous single crystal growth for CZT [19, 21]. In order to test the stoichiometry of the in-house grown CZT, energy-dispersive X-ray spectroscopy is employed.

Energy-dispersive X-ray spectroscopy (EDS) is a characterization technique performed in a scanning electron microscope (SEM) which can be used to determine the elemental composition of a material [25]. The sample to be tested is bombarded with high-energy electrons from the SEM, and inner-shell electrons within the material may be

excited and ejected from the material, creating an electron-hole pair. As electrons from the outer shell fill the holes created by the excited inner-shell electrons, X-rays are generated. The energy of these X-rays are characteristic of the atoms in which this occurred, and the energy between the two shells. Characteristic peaks on the EDS spectra appear based on these energies. Furthermore, percent element concentration of a sample can be determined by integration of the peaks corresponding to the major elements present, and taking the ratio of the area under the peaks. By using EDS, it is possible to gain approximate stoichiometry data for determining the ratio of Cd:Zn:Te present in the solvent-grown CZT crystals [26].

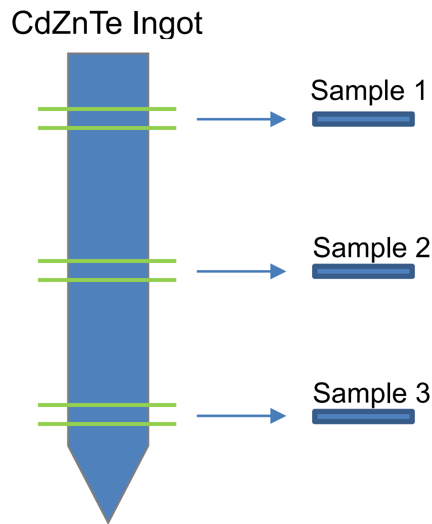


Figure 3.3. Samples harvested from CZT ingot for EDS studies.

EDS measurements were performed on three CZT samples. Sample 1 was harvested from a location near the top of a solution-growth CZT ingot, sample 2 was harvested from a location near the midpoint of the ingot, and sample 3 was harvested towards the tip of the ingot. Samples were polished using 0.05µm $Al_2O_3$ powder, but not etched. Figure 3.3 shows a schematic of the sample locations in the CZT ingot. EDS

measurements were taken using a Tescan Vega 3 SEM-EDS microscope, using 10kV SEM beam voltage with a magnification of ~70 X. Multiple positions were simultaneously taken, and values were averaged to ensure consistent results.

Table 3.1. EDS stoichiometry data for CZT samples, along with error percent. All values are given in atomic percentage (%at).

| | Cd | Zn | Te |
|---|---|---|---|
| **Sample 1** | 43.62 ± 1.73 | 0.86 ± 0.52 | 55.52 ± 2.83 |
| **Sample 2** | 38.5 ± 1.66 | 5.2 ± 0.86 | 56.2 ± 2.74 |
| **Sample 3** | 39.19 ± 1.61 | 5.9 ± 0.85 | 54.9 ± 2.62 |

Table 3.1 shows the stoichiometry data for the three CZT samples analyzed, along with their percent error. In an ideal case, the expected values for stoichiometric $Cd_{0.9}Zn_{0.1}Te$ will be 45:5:50 at%. Values seen in Table 3.1 indicate the samples are slightly Te rich, even accounting for the error percentage. However, the Cd and Te ratio values are close to literature reported values for detector-grade CZT [27]. It can also be seen that Zn concentrations for samples 2 and 3 are close to 5%, while sample 1 shows a significant deficiency in Zn concentration. This is likely due to the effects of Zn segregation, where Zn will tend to move during crystal growth [24]. Despite the lower Zn concentration towards the top of the ingot, the EDS data suggests that stoichiometric CZT crystals can be harvested from the middle to lower region of the grown CZT ingot. This means that the solvent growth method is capable of producing relatively homogeneous CZT crystals, just as reported by other modern CZT crystal growth methods (such as the modified vertical Bridgman method, and the travelling heater method) [9, 21].

## 3.5 INFRARED TRANSMISSION IMAGING

Another important characterization technique to determine the quality of CZT crystals is infrared transmission imaging. In addition to crystal growth defects, one major issue affecting CZT crystal quality grown using either stoichiometric or with excess Te is the presence of Te inclusions and precipitates uniformly distributed in the bulk crystal. Te inclusions and precipitates are Te-rich regions within the bulk crystal and surface regions, respectively. These Te inclusions/precipitates are defects which degrade the electrical properties of the CZT material, since the band gap of Te is ~0.3eV [28, 29], which is much lower than CZT. Because of the low band gap, when a CZT sample is imaged using IR, the infrared light will pass through the sample except at the locations of Te-rich sites within the crystal.

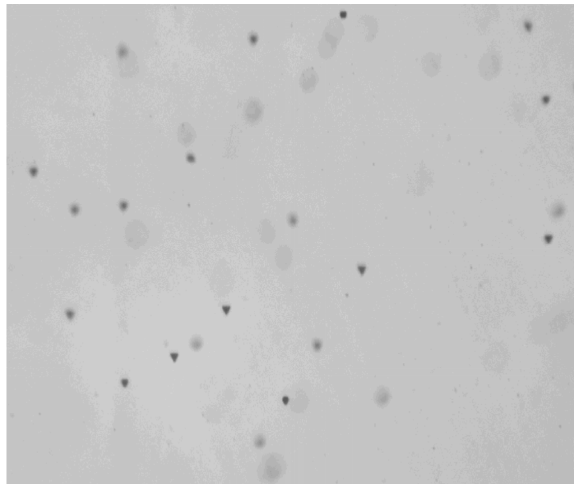

Figure 3.4. Infrared transmission image of a represntative portion of a grown CZT crystal (Scale: 1.2mm width x 1.0mm height).

Infrared transmission imaging was performed on a representative portion of a 1cm x 1cm x 1mm CZT crystal. The resulting infrared image can be seen in Figure 3.4, where dark spots appear as Te inclusions. The average size of the Te inclusions was estimated to

be ~8 μm. In the literature, it is reported that Te inclusions greater than 10 μm can act as charge trapping centers and therefore significantly degrade detector performance [29, 30]. The small size and low density of Te inclusons apparent from the infrared image indicate the good quality of the crystals, and their suitability for use as nuclear detectors.

## 3.6 Electrical Characterization

### 3.6.1 Background

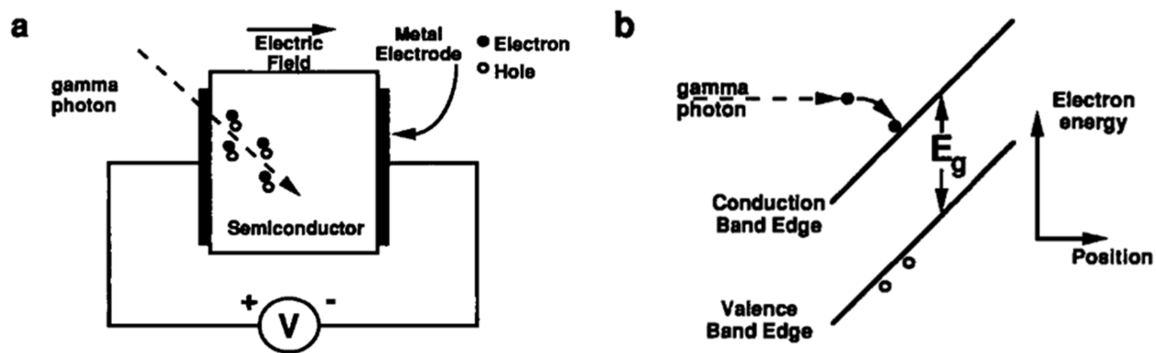


Figure 3.5. (a) Schematic [8] and (b) band diagram of a semiconductor nuclear detector under irradiation [8].

Appropriate metal contacts must be applied to a CZT crystal in order to fabricate a functional radiation detector. For nuclear detectors, an Ohmic contact is preferred in order to allow holes and electrons to travel through the semiconductor material un-impeded. Figure 3.5 shows the schematic and band diagram of an intrinsic semiconductor detector under voltage bias. Using an Ohmic contact allows the detector to have a higher charge collection efficiency, since both electrons and holes will equally contribute to the radiation detection signal without being blocked [8]. A further discussion of charge collection efficiency is given in Chapter 6. In order to use Ohmic contacts, the CZT crystal must have

a high resistivity, which will reduce the leakage current flowing through the detector when biased. For CZT crystals grown in our laboratory, indium doping is used in order to compensate for intrinsic defects present in the crystals, and place the Fermi-level as close to intrinsic as possible. However, CZT crystals grown with intentional doping to increase the resistivity are typically slightly p-type [31].

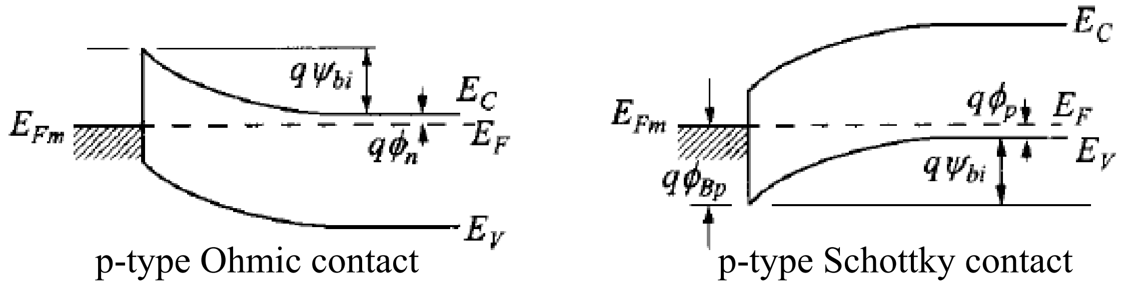


Figure 3.6. Band diagrams of Ohmic and Schottky contacts of p-type Ohmic and p-type Schottky contacts [32]

The current-voltage characteristic (I-V characteristic) of a metal-semiconductor junction is determined by the barrier height at the interface. An Ohmic contact has no barrier, and therefore produces a linear current-voltage response. A rectifying contact will produce a non-linear response. Because CZT has a large semiconductor work function (as calculated below), very few metals will produce an Ohmic contact for p-type CZT. N-type CZT has a higher compatibility with Ohmic contacts created by low work function ($\phi_m$) metals such as Al and In, however n-type CZT does not commonly have the high resistivity required for nuclear detectors [31]. Figure 3.6 shows a general band diagram of Ohmic and Schottky contacts for a p-type semiconductor material. For p-type Ohmic contacts on CZT, Au and Pt are the ideal choices due to high work functions of 4.8eV and 5.2eV respectively.

The following formulas can be used to calculate the semiconductor work function and the barrier height due to metal contacts:

$$\phi_b = \phi_m - \phi_s \tag{3.2}$$

$$\phi_s = \chi + (E_C - E_F) = \chi + \frac{Eg}{2} \tag{3.3}$$

where $\phi_b$ is the barrier height, $\phi_m$ is the metal work function, $\phi_s$ is the semiconductor work function, $E_c$ is the conduction band level, $E_F$ is the Fermi-level, $E_g$ is the band gap, and $\chi$ is the electron affinity. Using these formulas, where the electron affinity of CZT is about 4.3eV [32], and the band gap is 1.6eV; the semiconductor work function is calculated to be at 5.1eV:

$$\phi_s = \chi + (E_C - E_F) = \chi + \frac{Eg}{2} = 4.3eV + \frac{1.6eV}{2} = \sim 5.1eV \tag{3.4}$$

Table 3.2. Work Functions of selected contact metals for CZT [33].

| **Metals** | **Pt** | **Au** | **Al** | **Mo** | **In** | **Cu** | **Sn** | **Ti** | **W** |
|---|---|---|---|---|---|---|---|---|---|
| **Work Function (eV)** | 5.64 | ~5.4 | 4.1 | ~4.5 | 4.09 | ~4.5 | 4.42 | 4.33 | 4.55 |
| **Type of Contact** | Ohmic | | Schottky | | | | | | |

Table 3.2 shows the metal work function for several contact metals. To form an ohmic contact, it is required that the condition $\phi_m > \phi_s$ be satisfied [31]. From the table above, the metal work function of Pt is higher than the semiconductor work function which marginally satisfies this requirement.

When the barrier height ($\varphi_b$) is calculated for Au ($\varphi_m = 5.4$eV), for example:

$$\phi_b = \phi_m - \phi_s = \sim 5.4eV - 5.1eV = 0.3eV \qquad 3.5$$

In this example, gold barely makes an Ohmic contact with p-CZT. On the other hand, Al does not satisfy the requirements of having a high enough work function to produce an Ohmic contact. In the case of aluminum:

$$\phi_b = \phi_m - \phi_s = 4.1eV - 5.1eV = -1eV \qquad 3.6$$

Aluminum makes a Schottky barrier with p-CZT with a barrier height of 1eV. Because of the high work function requirements for Ohmic contacts with p-type CZT, very few metals can make an Ohmic contact with CZT. Also, since Au is an inert metal there is no possibility of it reacting with air or the CZT crystal. It can also be deposited by electroless deposition and sputtering. While only Au and Pt are suitable to form Ohmic contacts for detector grade p-type CZT, metals such as Al, In, Ni, and many other metals can form Schottky contacts with p-CZT [32].

### 3.6.2 Experimental

Table 3.3. CZT samples and detectors used for I-V studies.

| Sample Name | Crystal Size (L x W x H) $mm^3$ | Contacts |
|---|---|---|
| **P1** | 6.9 x 6.9 x 4.86 | Au-Au |
| **FG1** | 4.2 x 6.2 x 6.5 | Au-Au |
| **FG2** | 3 x 4 x 9 | Au-Au |
| **PGR1** | 11.3 x 11.3 x 11.1 | Au-Au |
| **CZT Schottky** | 7 x 7 x 5 | Pt-In |

Au Ohmic contacts were applied to the top and bottom of the CZT crystals by DC sputtering, using a Quorum Q150T DC sputtering unit. For Schottky contacts, In and Pt contacts were applied using DC sputtering. Table 3.3 shows a list of CZT samples which were tested using I-V characterization. Some samples listed are further explored for their detection properties, as seen in Chapter 6.

Current-voltage (I-V) characteristics were measured to show the relationship of the current flowing through the CZT material versus the applied bias voltage across the crystal. The plot generated through this measurement yields important information about leakage current in the CZT crystal. Higher leakage current at a given voltage has implications for noise that will be present during radiation detection measurements. I-V characteristics were carried out at room temperature using a Keithly 237 electrometer setup. For voltages above ±1100V, an external voltage bias was provided by a Canberra 3106D high voltage supply. The resistance of the CZT material was determined from the slope of the linear I-V plot. The resistivity was calculated using the following equation:

$$\rho = R \cdot \frac{A}{L} \tag{3.7}$$

where $\rho$ is the resistivity of the crystal in Ohm-cm, R is the resistance in Ohms, A is the contact area ($cm^2$), and L is the thickness of the CZT crystal in cm. The resistance R was determined using the inverse slope of the line produced by a linear fit of the Ohmic I-V characteristic curve.

### 3.6.3 Results for Ohmic Contacts

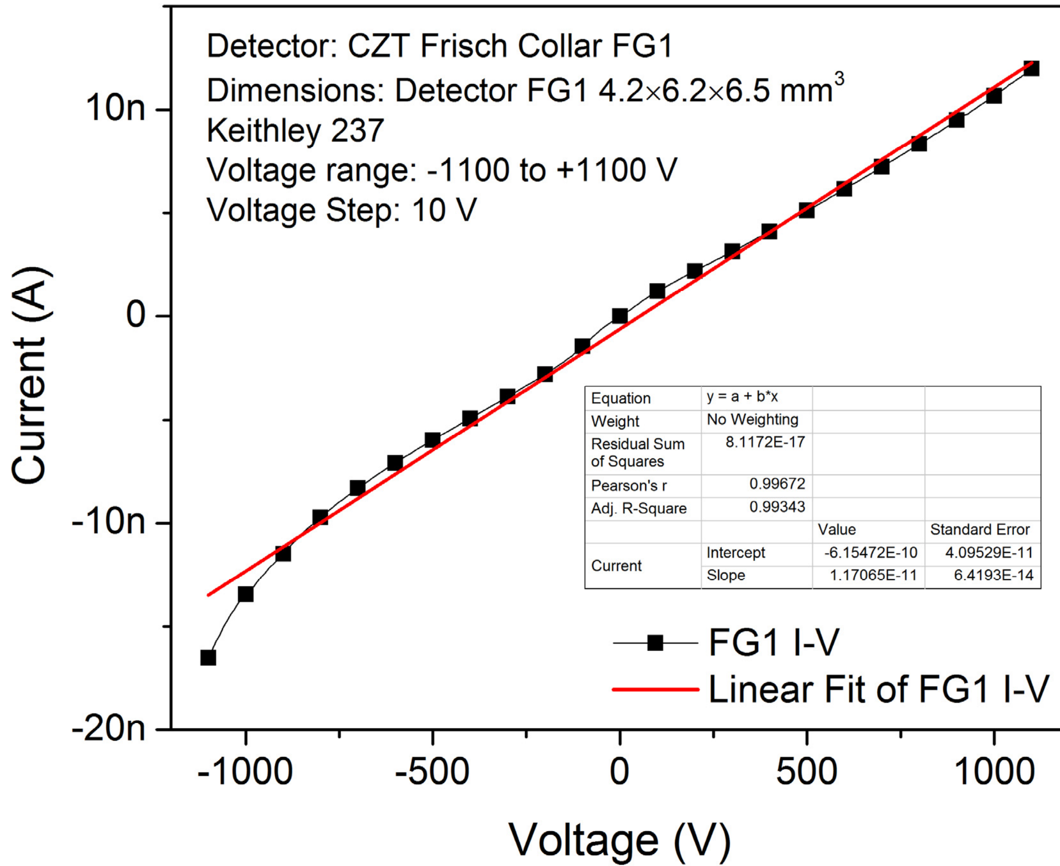


Figure 3.7. I-V characteristics of a detector-grade CZT crystal with Ohmic contacts, and a linear fit of the I-V curve used for resistivity measurements.

For a CZT crystal with Ohmic contacts, a linear I-V characteristic is obtained, as seen in Figure 3.7. By obtaining the inverse slope of the linear fit of the I-V curve, Equation 3.7 can be applied to obtain the bulk resistivity of the crystal, as follows:

$$\rho = R \cdot \frac{A}{L} = 8.54 \cdot 10^{10}\Omega * \frac{4.2mm * 6.2mm}{6.5mm} = 3.42 \cdot 10^{10}\ \Omega cm \qquad 3.8$$

The sample shown in Figure 3.7 has a calculated resistivity of $3.42 \times 10^{10}$ Ω-cm. This is in the correct range for the typical resistivities reported for detector-grade CZT crystals [9].

### 3.6.4 Results for Schottky Contacts

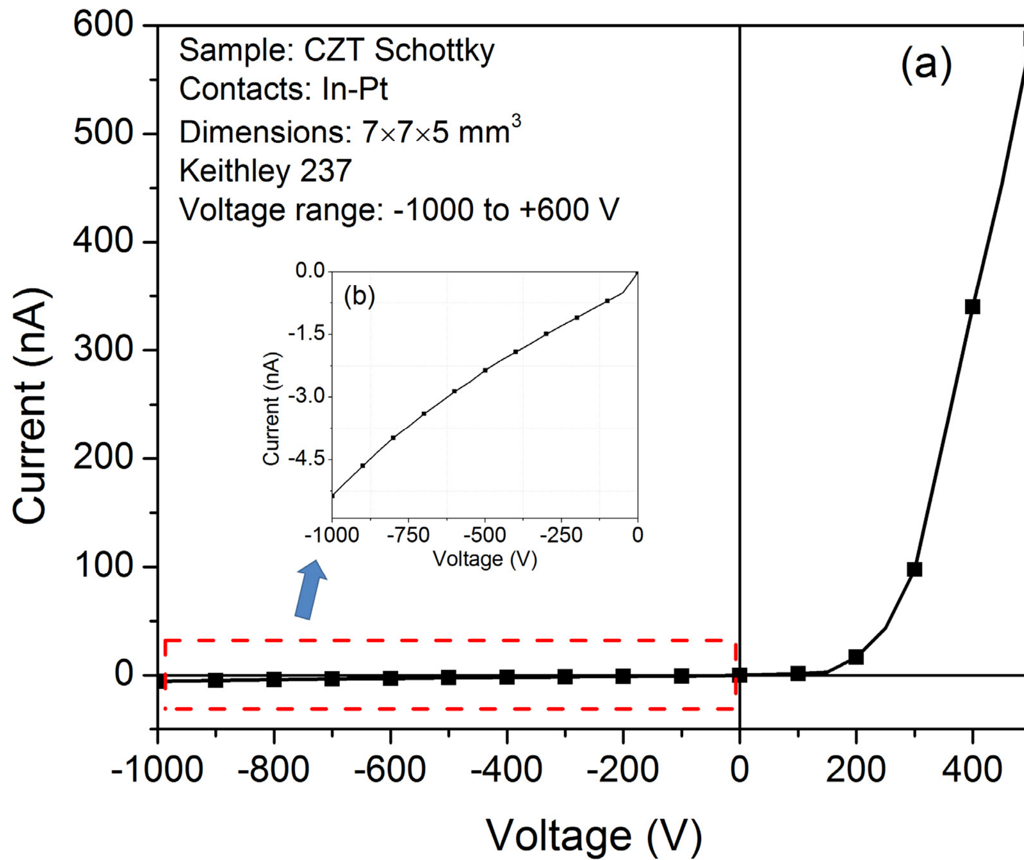


Figure 3.8. (a) I-V characteristics of a CZT crystal with Schottky contacts (indium and platinum), and (b) inset showing detailed reverse bias I-V characteristics.

Figure 3.8 shows the I-V characteristics for a CZT crystal with Schottky contacts. The results show excellent rectification properties, including a reverse bias current of 5.3 nA.

### 3.6.5 Results for Detector-grade CZT

I-V characterization and resistivity measurements are very important for fabricating CZT nuclear detectors, and predicting how well they will operate. Detectors with high resistivity and stable I-V characteristics are more likely to produce high energy resolution

under gamma-ray irradiation, by reducing the leakage current of the detector under voltage bias.

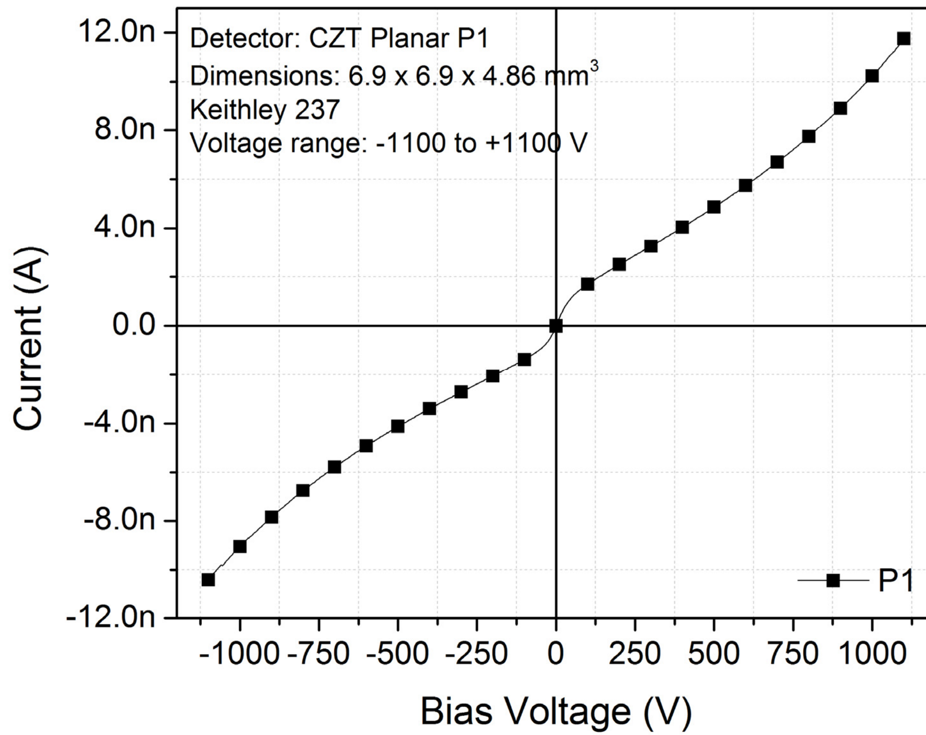


Figure 3.9. I-V characteristics of detector P1 from -1100V to +1100V.

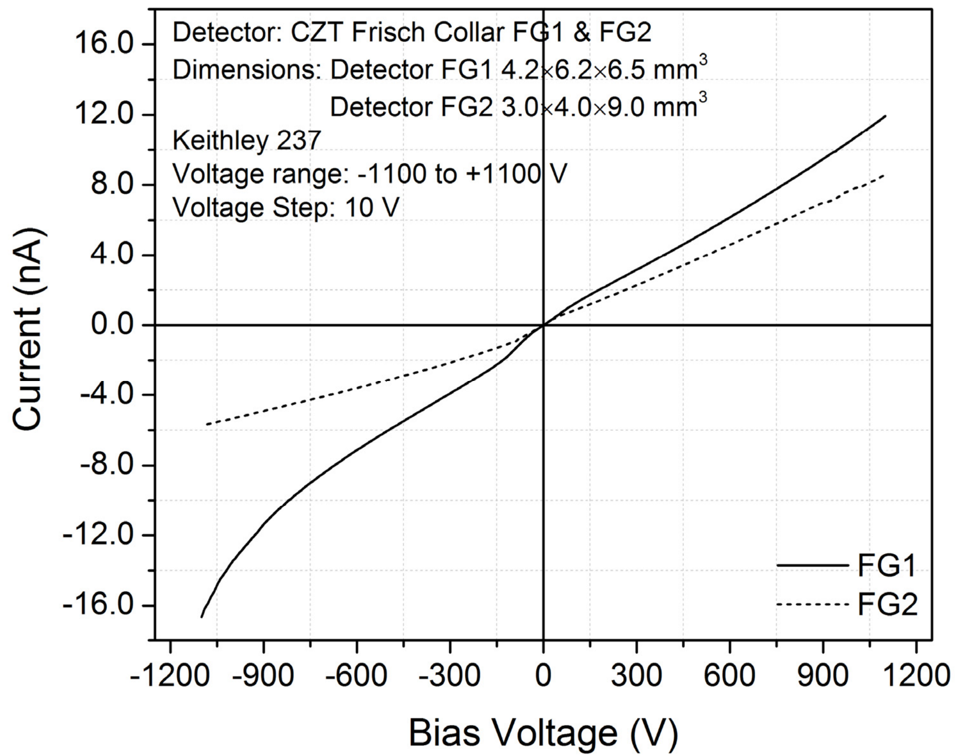

Figure 3.10. I-V characteristics of detectors FG1 and FG2 from -1100V to +1100V.

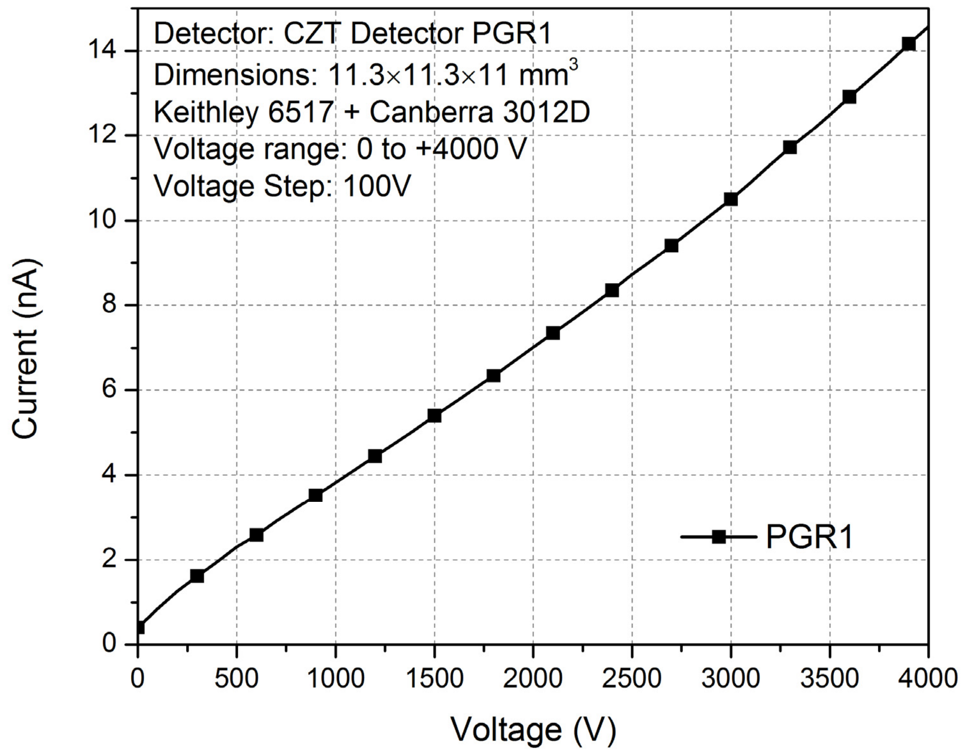

Figure 3.11. I-V characteristics of detector PGR1 from 0V to +4000V

Figure 3.9 shows the I-V characteristics of detector sample P1 from ±1100V bias, while Figure 3.10 shows the I-V characteristic comparison for detector samples FG1 and FG2 under ±1100V bias. In addition, Figure 3.11 shows I-V characteristics for detector PGR1 from 0V to +4000V bias. All four samples exhibit low leakage current, and very stable Ohmic properties with very little non-linearity. Table 3.4 shows the leakage current at +1000V bias, as well as the calculated bulk resistivity for each sample. According to the literature, in order for a CZT crystal to have sufficiently low leakage current (and therefore reduced noise, and efficient performance) when used as a nuclear detector, a resistivity value of ~$10^{10}$ Ω-cm is generally desired [9, 31]. A more in-depth discussion of the effect of leakage current on detector performance is presented in Section 6.3.4. According to Table 3.4, the samples are $10^{10}$ Ω-cm or higher, which satisfies the general resistivity requirements for being detector-grade CZT.

Table 3.4. Comparison of leakage current and resistivity of fabricated CZT detectors.

| Detector | Current at +1000V (nA) | Resistivity (Ω-cm) |
|---|---|---|
| **P1** | 10.2 | $1.04 \times 10^{11}$ |
| **FG1** | 10.7 | $3.42 \times 10^{10}$ |
| **FG2** | 7.8 | $1.99 \times 10^{10}$ |
| **PGR1** | 3.8 | $3.3 \times 10^{10}$ |

## 3.7 CONCLUSION

In this chapter, the grown CZT crystals were processed and characterized using a variety of optical and electrical techniques. The band gap of the crystals, revealed using optical transmission studies, was found to be in the correct range for detector-grade CZT. EDS studies showed that the grown CZT crystals are stoichiometric in the proportions

necessary to yield $Cd_{0.9}Zn_{0.1}Te$. Infrared transmission imaging revealed that Te precipitates/inclusions were 8 μm in size, where less than 10 μm is desirable for good quality CZT crystals [29]. Finally, electrical characterization of various CZT crystals revealed high resistivities in the range of ~$10^{10}$ Ω-cm, which is required in order to use the CZT crystals as nuclear detectors. These characterization techniques give insight on the potential performance of the CZT crystals when they are fabricated into nuclear detectors, and ensures that only the best samples are chosen to be fabricated into detectors.

# CHAPTER 4: SURFACE MODIFICATION

## 4.1 OVERVIEW

Surface modification is the act of placing an inert, non-reacting layer of material on the surface of a crystal or semiconductor, which will act as isolation from the external environment. It is typically used with semiconductors to provide stability to the electrical properties of the passivated materials, which can vary due to surface states present on the crystal. Passivation of the surface is usually done using metal oxides, organic compounds, or other similar materials, which generate a shell against corrosion while maintaining or improving the properties of the original semiconductor material [34]. This typically results in reduced leakage current, increase in breakdown voltage, and possible improvements in detection capabilities [35]. Numerous studies on surface passivation have been undertaken for CZT in the literature using $H_2O_2$ [36], KOH and $NH_4F$ [37, 38]. However, the effects of wet passivation using $Na_2S$ and $(NH_4)_2S$, which are commonly used techniques for III-V semiconductors such as GaAs [39, 40], is not well investigated for CZT.

For the studies presented in this work, sulfur passivation is investigated to reduce the surface leakage current caused by surface states. X-Ray photoelectron spectroscopy (XPS) was performed on the unmodified and modified CZT surfaces to determine the effectiveness of the passivation techniques in removing surface states. Electrical characterization before and after passivation was performed to determine if leakage current was reduced as a result of passivation the surface of the CZT crystals.

## 4.2 PASSIVATION THEORY

According to models in the literature, surface states existing between the semiconductor-metal interface can contain a number of energy levels which can appear below the conduction band [41, 42]. These surface states can be caused by surface defects, or dangling bonds reacting with the environment to form compounds. These states can cause current conduction along the surface of the semiconductor, which can be a significant contributor to the overall leakage current of a detector. Passivating ions adsorbed to the surface can form stable chemical bonds on the surface of the semiconductor, eliminating the effects of surface states and reducing the leakage current caused by surface conduction. For a Schottky diode, the benefit of passivation is a reduction of electron tunneling near the conduction band.

Figure 4.1 shows the band-diagrams of a metal-semiconductor junction with an unpassivated and passivated interface. Surface modification, through chemical passivation, provides a mechanism to split the original surface state $E_{SS}$ to the midgap state $E_{SS\text{-}ION\text{-}1}$ and the state $E_{SS\text{-}ION\text{-}2}$ present at the edge of the conduction band [41]. Electrons are unable to tunnel through the midgap state $E_{SS\text{-}ION\text{-}1}$ since the barrier is thicker. Since $E_{SS\text{-}ION\text{-}2}$ lies at or above the edge of the conduction band, electrons cannot be captured by this surface state. By eliminating the ability of electrons to tunnel through surface states, a leakage current decrement is expected in a Schottky diode fabricated using a passivated semiconductor surface.

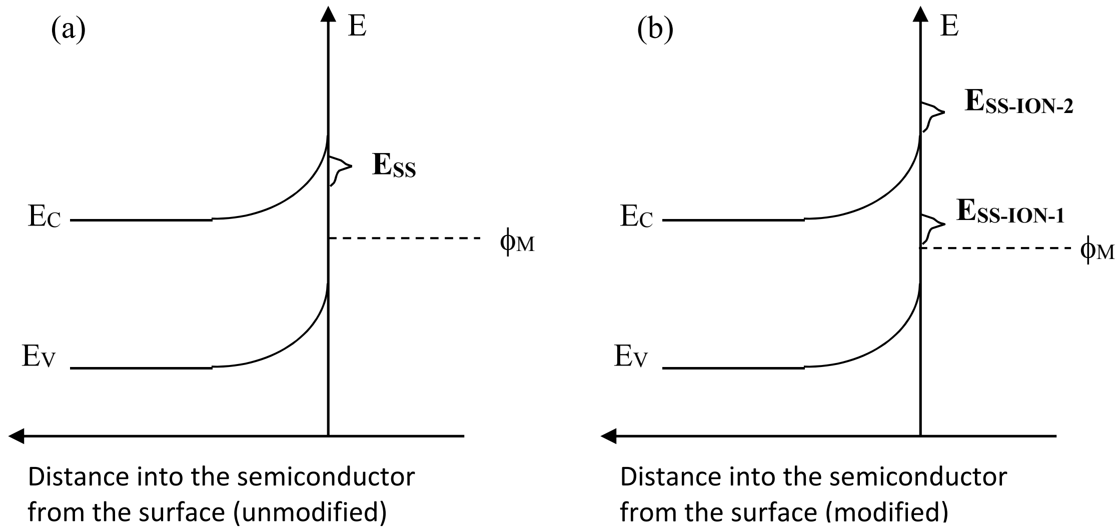


Figure 4.1. Band-diagram showing the Schottky semiconductor-metal interface for (a) an unmodified semiconductor with surface states and (b) surface state splitting due to passivation. [41]

## 4.3 EXPERIMENTAL

Three 1cm x 1cm x 1mm CZT crystals were polished and etched using Br:MeOH in preparation for passivation and XPS studies. CZT Sample 1 was unmodified (not passivated), CZT Sample 2 was passivated by placing the sample in a $Na_2S$ solution, and CZT Sample 3 was passivated by placing it in an $(NH_4)_2S$ solution. The passivated samples were placed in solution for 15 minutes at a temperature of 60°C, with argon bubbling in the solution during the entire procedure to prevent oxidation. The passivated samples were then removed, rinsed with de-ionized water, dried using argon gas, and placed under a vacuum for 1 minute to ensure moisture is removed. Gold was sputtered for 2 seconds onto all three samples in preparation for XPS studies.

## 4.4 X-RAY PHOTOELECTRON SPECTROSCOPY

### 4.4.1 XPS Theory

X-Ray Photoelectron Spectroscopy (XPS) is a surface characterization technique which can identify elemental composition, chemical states, bonding information, and types of compounds present in a material [43]. In this experiment, a photon of known energy, $h\nu$, bombards the surface of a material with the expectation of being absorbed by the material's atoms. Once absorbed, this leads to ionization and emission of an inner shell electron into the vacuum environment, according to:

$$E_k = h\nu - E_b \quad (4.1)$$

All elements exhibit characteristic binding energies, $E_b$, associated with its atomic orbit. This means that each element and molecule will give rise to specific peaks in the XPS spectrum at the kinetic energies $E_k$, depending on the photon energies and binding energies. Most modern XPS systems use monochromatic x-ray sources, which emit photons with a fixed energy. When subtracted from the kinetic energy, the binding energy of the detected photoelectrons are known, and the element and electron core level related to these counted photoelectrons can be determined.

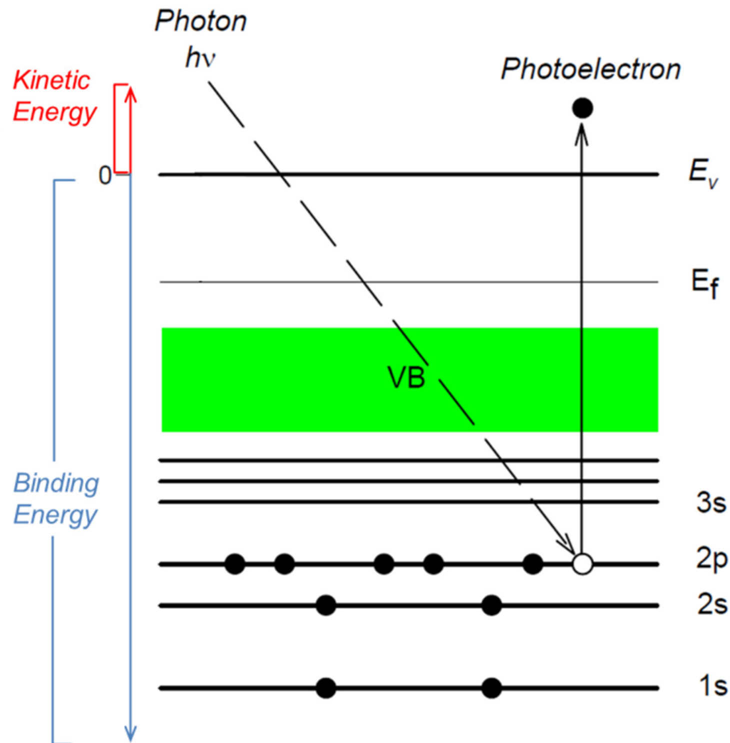


Figure 4.2. Schematic diagram of binding energy and Kinetic energy of a displaced electron due to x-ray interaction with a material.

### 4.4.2 XPS Experimental

XPS measurements were carried out on a Kratos AXIS Ultra DLD XPS system equipped with a hemispherical energy analyzer and a monochromatic Al Kα source. The monochromatic Al Kα source was operated at 15 KeV and 150 W incident on surface at 45° with respect to the surface. The pass energy was fixed at 40 eV for the detail scans, and a high performance charge neutralizer was used to compensate for the sample surface charge. The binding energy of the analyzer was calibrated using Au sputtered for 2 seconds on the surface of the scanned CZT samples. Au is used as a reference instead of C in order to improve the reliability of the calibration. The sample chamber was kept under ultra-high vacuum level of $2\times10^{-9}$ Torr.

### 4.4.3 XPS Results

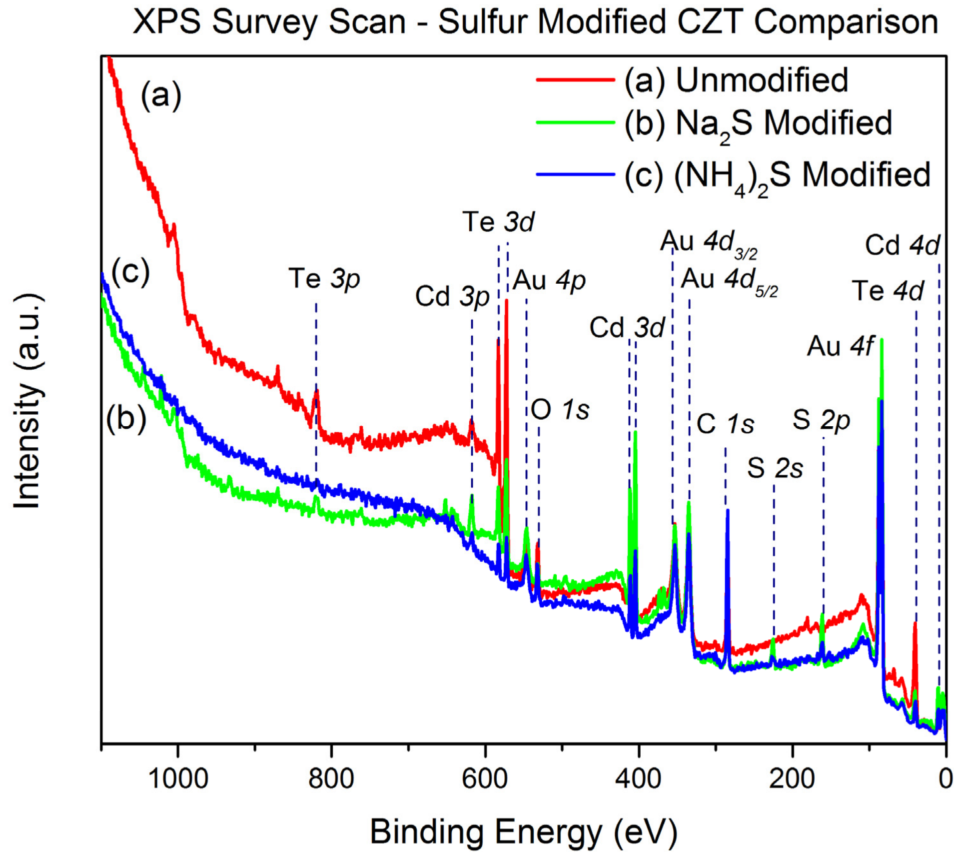


Figure 4.3. XPS survey scan for (a) unmodified CZT sample (no passivation), (b) $Na_2S$ modified CZT sample, and (c) $(NH_4)_2S$ modified CZT sample.

Figure 4.3 shows the XPS survey scan for the unmodified, $Na_2S$ modified, and $(NH_4)_2S$ modified CZT samples. The survey spectrum show typical spectral lines for CdTe and CZT for Cd, Te, O, and C. Additionally, the Au *4f* reference can be seen, as well as S *2p* and S *2s* levels for the passivated samples. To provide further insight into the effects of passivation on the samples, Te *3d*, Te *4d*, Cd *3d*, and S *2p* high resolution spectra was acquired before and after passivation.

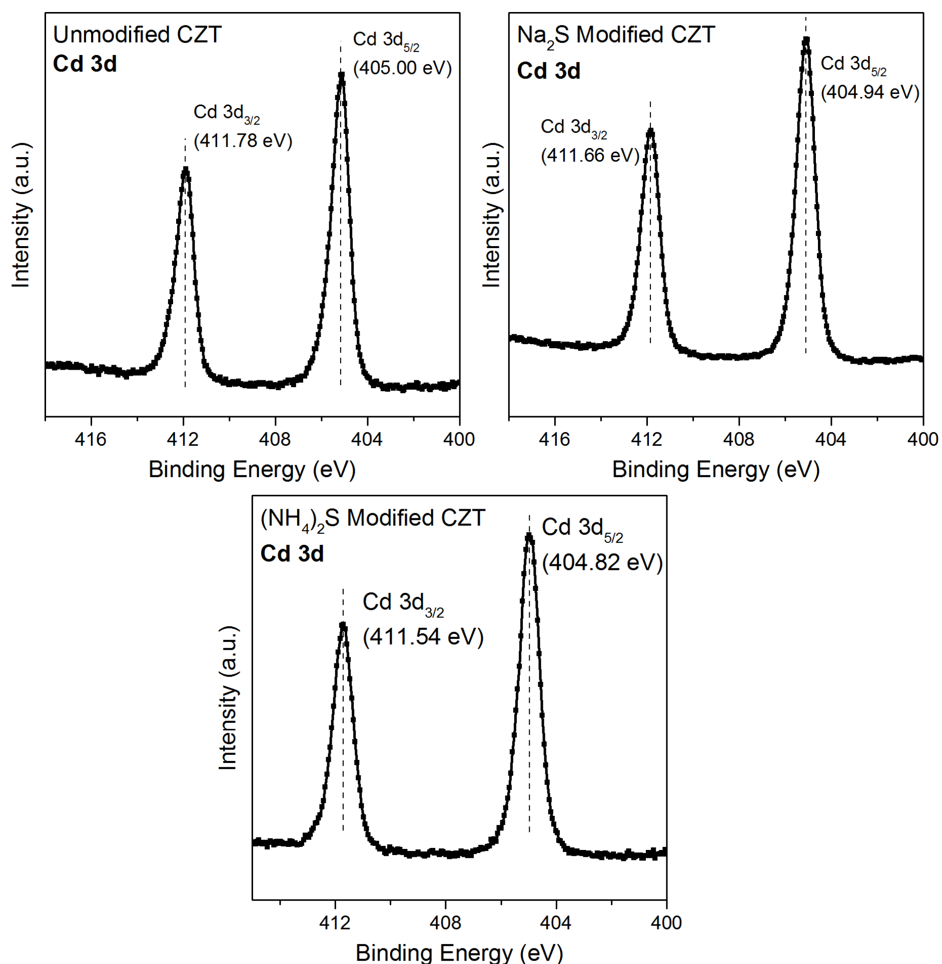


Figure 4.4. High-resolution XPS spectra of Cd *3d* core levels for unmodified, $Na_2S$ modified, and $(NH_4)_2S$ modified CZT crystals.

Figure 4.4 shows the high-resolution XPS scan of the Cd 3d core levels for unmodified, $Na_2S$ passivated, and $(NH_4)_2S$ passivated CZT. The Cd $3d_{3/2}$ core level peaks all exist at ~411-412 eV, while Cd $3d_{5/2}$ peaks reside at ~405 eV, which is in agreement with typical reported values for CdTe and CZT [44, 45]. No major peak changes are observed due to passivation. The lack of change due to passivation is consistent with literature suggesting any CdO present will either be masked by other elements and therefore difficult to deconvolute, or the amount of CdO present is insignificant [46, 47].

Furthermore, it is suggested that etching and exposure of CZT to air does not produce significant oxidation in the form of CdO [48].

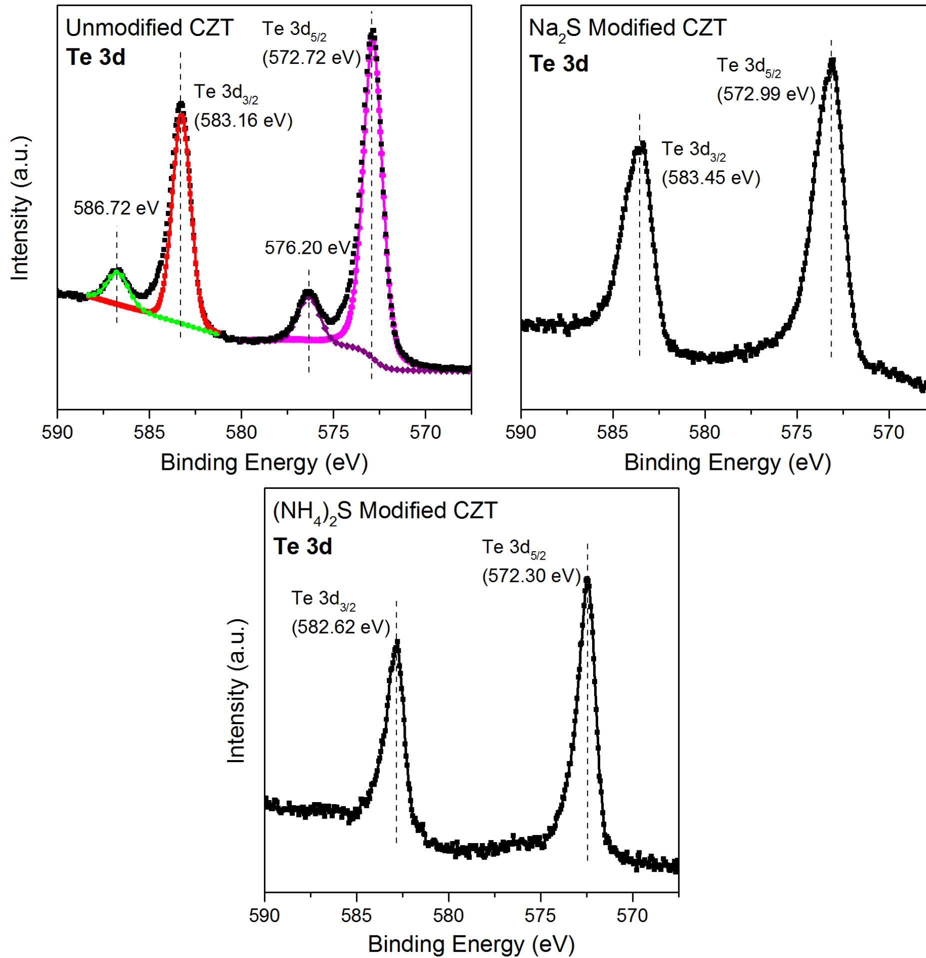


Figure 4.5. High-resolution XPS spectra of Te *3d* core levels for unmodified, $Na_2S$ modified, and $(NH_4)_2S$ modified CZT crystals.

Figure 4.5 shows the high-resolution spectra for the Te 3d core levels for the CZT samples. A $3d_{3/2}$ and $3d_{5/2}$ doublet was observed on every CZT sample at ~583 eV and ~572 eV, respectively, which is consistent with reported Te 3d levels [44], and caused by the Te-Cd bonds (the $Te^{-2}$ state) [49]. Two additional peaks are present in the spectra of the unmodified CZT at 586.72 eV and 576.2 eV, which are associated with O-Te bonding (the

$Te^{+4}$ state) caused by $TeO_2$ [50, 51]. The $Na_2S$ and $(NH_4)_2S$ passivated samples do not have the additional $TeO_2$ peaks present in the unmodified spectra. This indicates that both methods of sulfur passivation, $Na_2S$ and $(NH_4)_2S$, have removed the $Te^{4+}$ state from the surface of the CZT and formed a passivated layer.

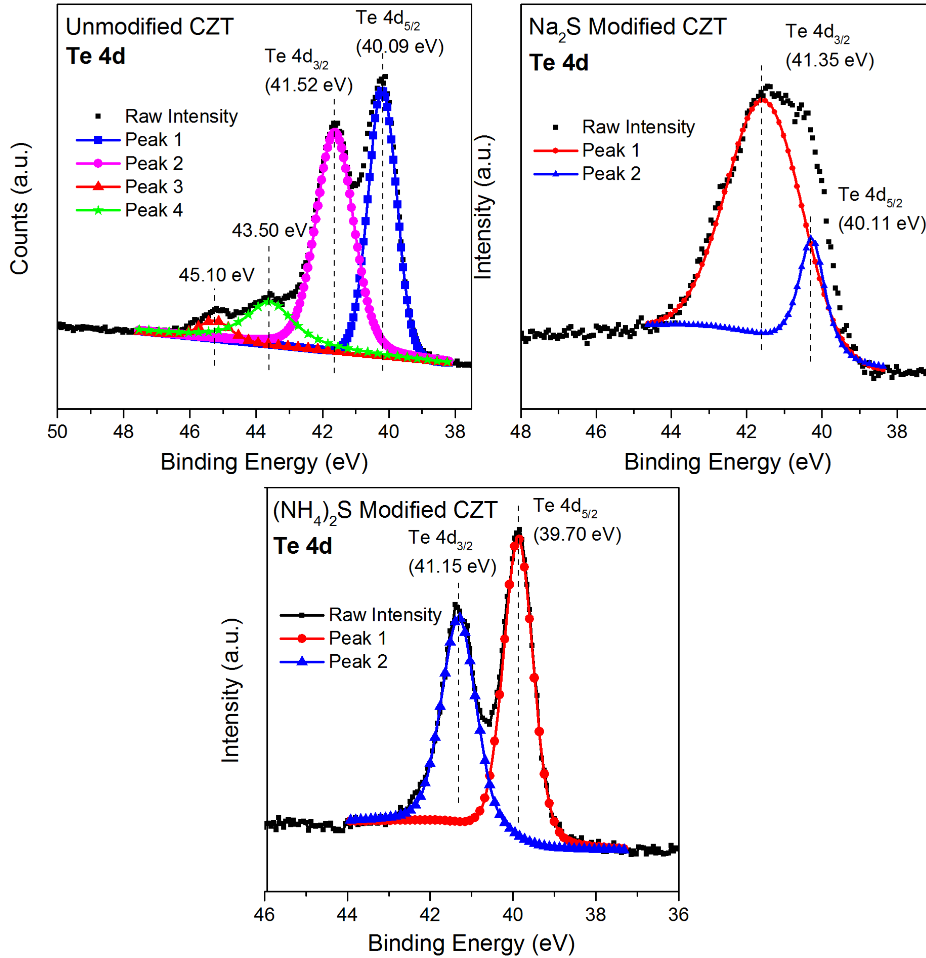


Figure 4.6. High-resolution XPS spectra of Te *4d* core levels for unmodified, $Na_2S$ modified, and $(NH_4)_2S$ modified CZT crystals.

Figure 4.6 shows the deconvoluted high-resolution spectra for the Te 4d core levels for the CZT samples. The Te $4d_{3/2}$ and $4d_{5/2}$ doublet was observed in all samples at ~41.5 – 41.1 eV and ~40.1 – 39.7 eV, respectively, which is consistent with reported values [52].

In addition, the unmodified CZT XPS spectra shows additional peaks at higher binding energies of 43.5 eV and 45.1 eV, consistent with the presence of $TeO_2$ and $CdTeO_3$ along with $Te^{+4}$ surface states [52, 27]. The $Na_2S$ and $(NH_4)_2S$ passivated samples do not have the additional oxide peaks present in the unmodified spectra, similar to the case of Te 3d. This indicates the successful passivation of the $Te^{+4}$ surface states.

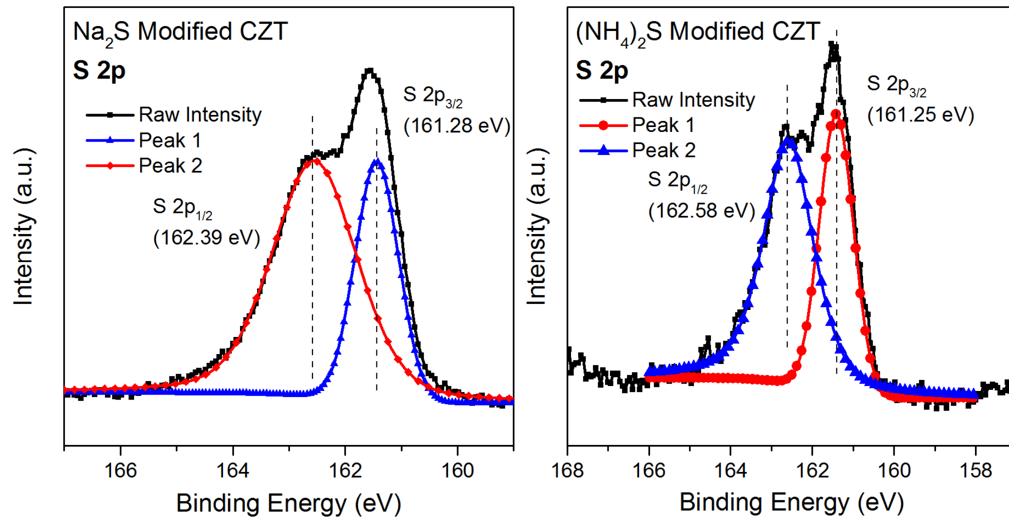


Figure 4.7. High-resolution XPS spectra of S *2p* core levels for $Na_2S$ modified and $(NH_4)_2S$ modified CZT crystals.

Figure 4.7 shows the deconvoluted high-resolution spectra for the S 2p core levels for the $Na_2S$ and $(NH_4)_2S$ passivated CZT samples. The S $2p_{1/2}$ and $2p_{3/2}$ core binding energies are located ~162 eV and ~161.2 eV respectively, which is supported by prior literature on $(NH4)_2S$ passivation of CZT [52]. The literature suggests that the S 2p peaks indicate sulfide formation when sulfur replaces tellurium, either as $CdTe_{1-x}S_x$ or CdS formation. This supports the Cd 3d, Te 3d, and Te 4d high resolution spectra, which indicate removal of Te surface states and oxides, but no change for Cd surface states.

## 4.5 PASSIVATION AND ELECTRICAL CHARACTERIZATION

In order to determine the effect of surface passivation on the electrical properties of CZT, four CZT samples were characterized using I-V measurements before and after $Na_2S$ passivation. Samples A (7.3 x 7 x 1.1 mm) and B (4.6 x 3.5 x 0.87 mm) were tested with Ohmic contacts (Au), while samples C (7.2 x 5.8 x 1.09 mm) and D (7.3 x 7 x 1.1 mm) were tested with Schottky contacts. Sample C used Pt-Al top and bottom contacts to form a Schottky barrier, while sample D used Pt-Sn contacts. Samples were polished and etched with bromine methanol according to the procedure in Section 3.2. Au, Pt, Sn, and Al contacts were applied using DC sputtering. After performing I-V characterization on the samples without passivation, samples were re-polished, re-etched, and passivated using an $Na_2S$ solution for 15 minutes. Contacts were then re-applied and I-V measurements were repeated.

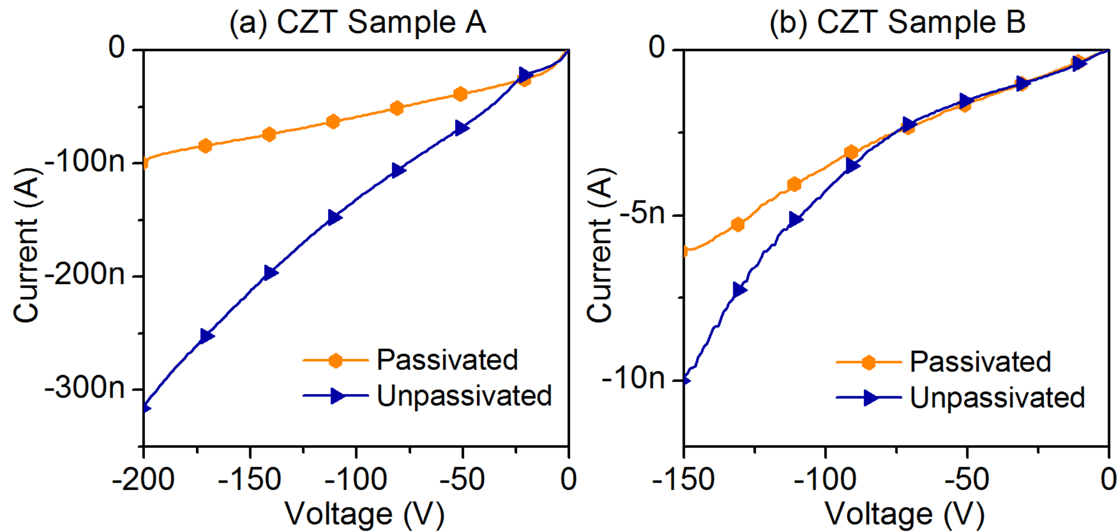


Figure 4.8. I-V characteristics of (a) CZT sample A, and (b) CZT sample B, showing unpassivated and passivated electrical properties for Ohmic contacts.

Figure 4.8 shows the I-V characteristics of samples A and B before and after passivation. Figure 4.8a shows that the unpassivated leakage current for sample A to be 313 nA at -200V, while passivated leakage current is 98 nA at -200V, showing a 219% reduction in leakage current due to passivation. Figure 4.8b shows the unpassivated leakage current for sample B to be 10 nA at -150V, while passivated leakage current is 6 nA at -150V, showing a 66% reduction in leakage current due to passivation. The reduction in reverse bias leakage current for Ohmic contacts can be attributed to the reduction of oxidized surface states shown by the XPS results. Conductive oxides such as $TeO_2$ can influence the surface conduction currents contributing to overall leakage current [9]. The XPS results show that these surface oxides are removed through passivation, which explains the lower leakage current seen after passivation.

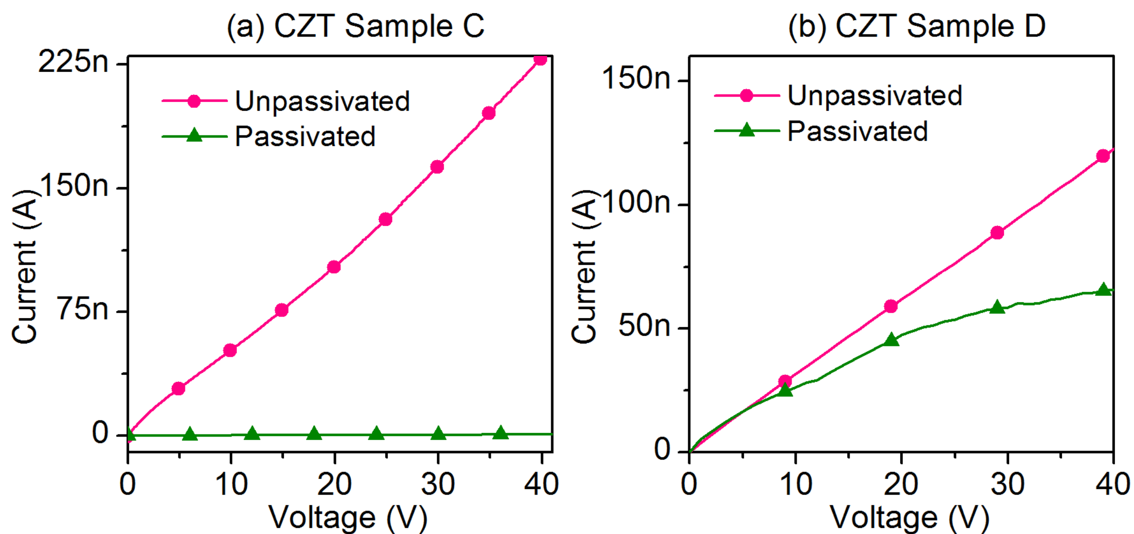


Figure 4.9. I-V characteristics of (a) CZT sample C and (b) CZT sample D, showing unpassivated and passivated electrical characteristics for Schottky contacts.

Figure 4.9 shows the I-V characteristics of samples C and D before and after passivation. Figure 4.9a shows that the unpassivated leakage current for sample C with Pt-Al contacts to be 238 nA at 40V, while passivated leakage current is 0.63 nA at 40V, showing a very large $10^3$ order-of-magnitude reduction in leakage current due to passivation. Figure 4.9b shows the unpassivated leakage current for sample D with Pt-Sn contacts to be 122 nA at 40V, while passivated leakage current is 65 nA at 40V, showing an 87% reduction in leakage current due to passivation. In the case of Schottky contacts on CZT, the reduction of leakage current can be attributed to the splitting of surface states [41]. By splitting the surface states, electrons are not able to tunnel through the barrier provided by the rectifying contacts, and leakage current in reverse bias is therefore reduced.

## 4.6 Conclusion

In this chapter, passivation was explored as a means to reduce the effects of surface states contributing to surface leakage current in CZT. Two sulfur passivation techniques were applied and their effects were studied using XPS. The XPS studies confirmed that sulfur passivation was effective at removing native oxides from the CZT surface. Electrical characterization revealed that overall leakage current has been reduced by at least ~200% as a result of passivation for both Ohmic and Schottky contacts applied to CZT. These results show that sulfur passivation has good promise to reduce overall detector leakage current, and can thereby improve overall detector performance.

# CHAPTER 5: DEFECT CHARACTERIZATION

## 5.1 OVERVIEW

The most problematic impediment to the commercialization and high-volume production of detector-grade CZT is the presence of defects within the crystal structure. This includes impurities, dislocations, point defects, and macroscopic defects created during the crystal growth process [53, 54]. Macro-defects such as cracks, grain-boundaries, and twin-boundaries can lower the usable single-crystal volume of a CZT ingot down to 25% [9]. Surface defects can cause increased leakage current and poor noise performance for a fabricated CZT detector [31]. Furthermore, deep defect levels within the CZT semiconductor can act as charge traps (electron or hole), which can trap the charges generated due to interaction with nuclear radiation [55]. In particular, the poor hole transport properties of CZT caused by deep-level defects require that special detector geometries be applied to CZT-based detectors.

An analysis of surface and deep-level defects was performed in order to determine the presence and cause of defects within the CZT crystals grown in the laboratory. Thermally Stimulated Current (TSC) experiments were performed to reveal deep-level defects in the CZT crystals. TSC characterization is commonly applied to semi-insulating materials which can reveal information about electron and hole traps, such as the activation energy and capture cross section [56, 57]. Chemical etching in combination with atomic force microscopy and optical microscopy was performed to reveal the density of defects

present on the surface of representative portions of CZT samples [58, 59]. Finally, Electron Beam Induced Current studies were performed on a fabricated CZT Schottky diode to observe deep-level defects present in the bulk CZT material [60]. These studies will give insight into the type of defects and their possible degradation of the electrical and detection properties of the grown CZT crystals.

## 5.2 THERMALLY STIMULATED CURRENT

### 5.2.1 Background and Experimental

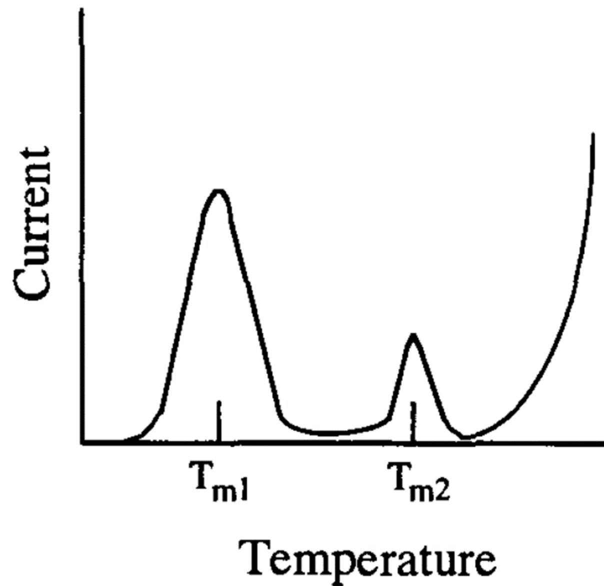


Figure 5.1. Schematic of TSC spectrum showing trap centers at temperatures $T_{m1}$ and $T_{m2}$ [56].

Thermally stimulated current (TSC) spectroscopy is a technique used to study deep energy levels in semiconductor materials [56]. In TSC, a semiconductor sample is cooled to a low temperature (below 100K). At this temperature, trap centers for holes/electrons are filled using light of a wavelength greater than or equal to the band-gap of the material.

Once the trap levels are filled, the energy stored in the traps are released by slowly heating the sample at a constant rate. The semiconductor sample is connected to an ammeter and a PC, which records the current generated by the trapped charges during sample heating. This current when plotted as a function of temperature produces a TSC spectrum.

Peaks present in the generated TSC spectrum represent trap levels within the semiconductor, which have released their energy as current due to constant heating of the sample. Figure 5.1 shows a schematic of TSC spectrum, showing trap centers revealed as peaks $T_{m1}$ and $T_{m2}$ in the current vs. temperature curve [56]. These trap centers, which will appear at various heating rates, can be plotted on an Arrhenius plot. The activation energies of the trap centers can then be determined from the slope of the Arrhenius plot, generated from the trap centers $T_m$, using the following equation [61]:

$$\frac{E_T}{kT} = \ln\left(\frac{T_m^4}{\beta}\right) + \ln\left(\frac{10^{17} * \sigma}{E_T}\right) \qquad 5.1$$

where $E_T$ is the activation energy of the trap level, $\beta$ is the heating rate, $\sigma$ is the capture cross section, and $k$ is the Boltzmann's constant. After determining the activation energy, TSC peaks were fit using the following equation [61, 62] to determine the trap capture cross section:

$$I_{TSC} = CV_b q\mu\tau N_T e * \exp\left(-\int \frac{e}{\beta \mathrm{d}T}\right) \qquad 5.2$$

where C is the constant related to the sample geometry, q is electronic charge, $\mu$ is the carrier mobility, $\tau$ is the carrier lifetime, $N_T$ is the trap capture cross section, $V_b$ is the bias voltage, e is the emission rate of trapped carriers, and $\beta$ is the heat rate.

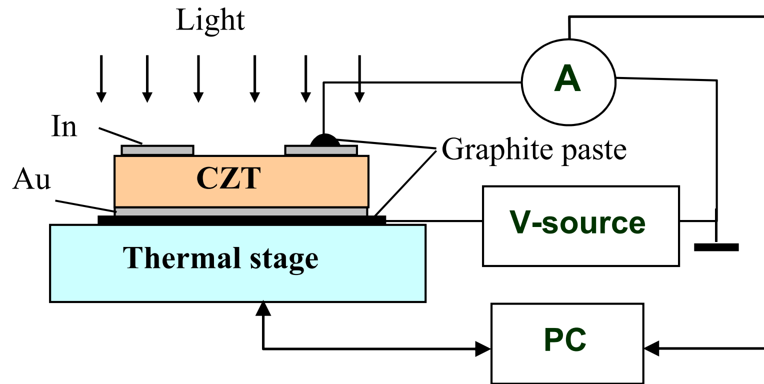


Figure 5.2. Schematic of the TSC experimental setup.

The TSC experiment was performed using a 1cm x 1cm x 1mm CZT Schottky diode with Au-In metal contacts. Figure 5.2 shows the TSC experiment schematic. The CZT diode was attached to a thermal stage using graphite paste to ensure thermal and electrical conductivity. TSC measurements were conducted from a temperature range of 94 to 400K under a $10^{-5}$ vacuum inside a low temperature microprobe station. An MMR wide range thermal stage provided temperature variation, and the generated TSC spectrum was controlled and recorded using a Keithley 6517A electrometer connected to a PC running LabVIEW software. Traps in the CZT diode were filled by illumination at 94K for 2 minutes using a 10W white halogen light bulb through a microscope window.

### 5.2.2 Results

Figure 5.3a shows the TSC spectra obtained from the CZT diode at sample heating rates of 4, 8, and 15 K/min under 10V reverse bias. Figure 5.3b shows the same TSC spectra with the dark current subtracted, which more clearly shows TSC peaks in the spectra.

Figure 5.4a shows TSC spectra at 0, 1, and 10V bias voltage for the CZT diode, with a constant heating rate of 15K/min, while Figure 5.4b shows TSC spectra at 4, 8, and 15K/min heating rates under 0V bias. As the sample bias voltage is increased, the resulting

TSC spectra shows an increase in the TSC peak intensity, due to the increase of the depletion region width and therefore an increase in the number of traps which can contribute to the TSC spectra. This shows that the TSC spectra are due to traps in the bulk, and therefore crystalline defects, as opposed to traps at or near the surface of the sample.

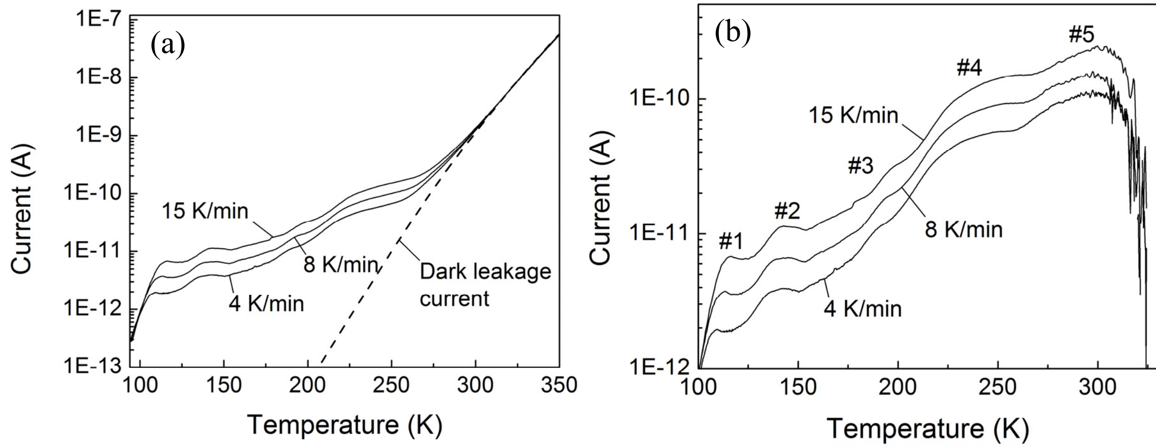


Figure 5.3. (a) TSC spectra obtained using CZT Schottky diode at 4, 8, and 15 K/min heat rates and 10 V bias, (b) TSC spectra from panel (a) with subtracted leakage current.

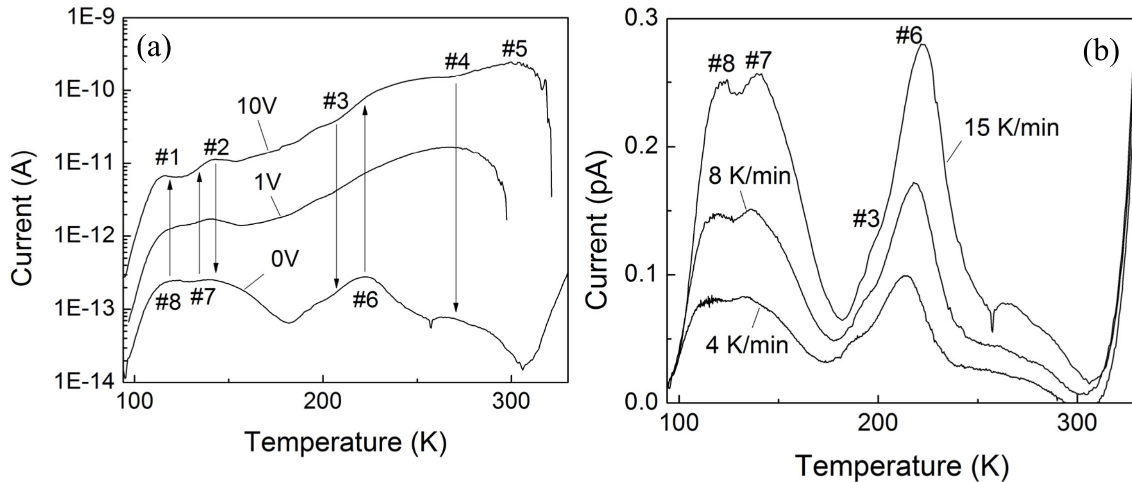


Figure 5.4. (a) TSC spectra for the CZT crystal at 0, 1, and 10 V reverse bias voltage and 15 K/min heat rate. (b) TSC spectra for CZT crystal at 4, 8, and 15 K/min and 0 V bias.

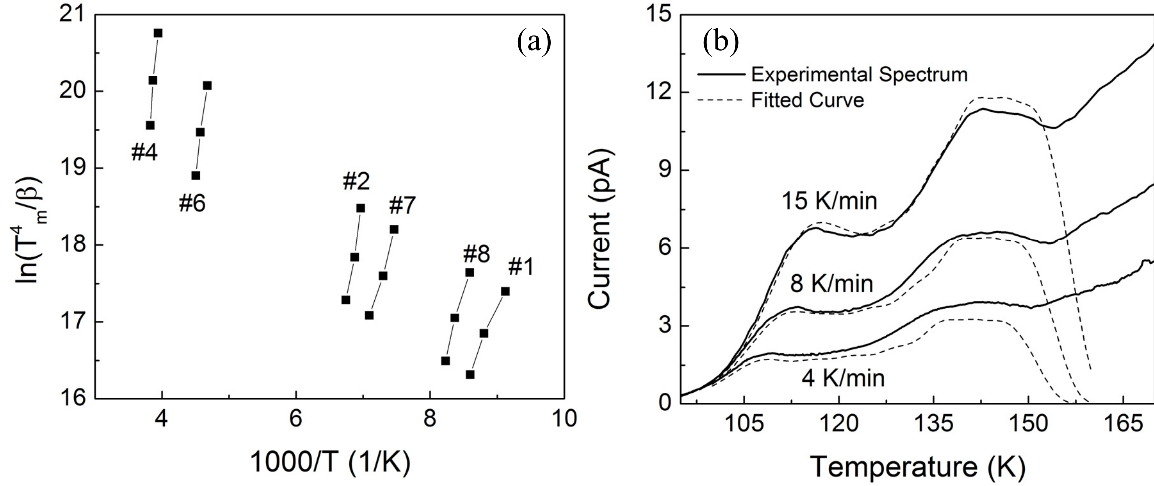


Figure 5.5. (a) Arrhenius plot deduced from the TSC spectra at 10 V and 0 V bias shown in Figure 5.3b and Figure 5.4b respectively. (b) Theoretical fit of peaks # 1 and #2 in Figure 5.3b using nine energy levels in the range 0.18 – 0.47 eV.

From the TSC peaks observed in Figure 5.3 and Figure 5.4, the Arrhenius plot shown in Figure 5.5a was generated. Using the slope of the Arrhenius plot (seen in Figure 5.5a) and Equation 5.1, the activation energies $E_T$ of the trap centers were calculated and are shown in Table 5.1. The TSC peaks and their activation energies were attributed to impurities and intrinsic defects based on prior work and data on deep level traps in CdTe and CZT [63, 64].

TSC peaks #2 and #4 are of special interest, due to their contribution to hole trapping effects in the CZT sample. Peak #2 can be correlated to $(Te_{Cd}+2V_{Cd})^{2-/-}$ with an ionization energy ~ 0.45 eV above the valence band [64], with a large capture cross section of $10^{-12}$ $cm^{-2}$. Peak #4 can be attributed to a complex of a single or double $V_{Cd}$ bound to a Te anisite ($(Te_{Cd}+2V_{Cd})^{3-/2-}$or $(Te_{Cd}+V_{Cd})$, ~ 0.9 eV below $E_c$) [64]. Peak #4 has a high intensity seen on the TSC spectrum, which indicates a high concentration of these complexes.

Table 5.1. Trap parameters deduced from TSC measurements of the fabricated CZT Schottky diodes related to major defect levels.

| TSC peak # | $T_m$ (K) | Activation energy (eV) | Capture cross section ($cm^2$) | Possible defect |
|---|---|---|---|---|
| 1 | 116* | 0.18 | $10^{-19} – 10^{-16}$ | $V_{Cd}^{0/-}$ |
| 2 | 145* | 0.46 | $10^{-12}$ | $(Te_{Cd}+2V_{Cd})^{2-/-}$ |
| 4 | ~261* | 0.86 | - | $(Te_{Cd}+2V_{Cd})^{3-/2-}$ or $(Te_{Cd}+V_{Cd})^{-/0}$ |
| 6 | 222** | 0.58 | $4\times10^{-14}$ | $Te_{Cd}^{+2/+}$ |
| 7 | 140** | 0.26 | $10^{-18}$ | $Te_{Cd}^{0/+}$ |
| 8 | 121** | 0.27 | $10^{-15}$ | $V_{Cd}^{2-/-}$ |

* from TSC spectra at 15 K/min heat rate and 10 V bias
** from TSC spectra at 15 K/min heat rate and 0 V bias

The large capture cross section, intensity, and negative charge state of TSC peaks 2 and 4 indicate the presence of strong hole traps within the CZT diode, which can adversely affect the hole transport properties. This assertion is consistent with the common issue of hole trapping with CZT nuclear detectors, which requires that special detector geometry be used to avoid the resulting poor hole transport properties. While electron traps have been deduced from the TSC spectra, their capture cross section, intensity, and number of traps are far less than the detected hole traps.

## 5.3 Chemical Etching

### 5.3.1 Background and Experimental

Chemical etching is a method used to remove layers of a material from its surface using suitable chemical reactants or etchants. In the case of defect analysis, suitable etchants are chosen which will preferentially etch along dislocations and defects at a greater rate than the defect-free regions of the material. This results in pits and depressions on the

surface of the crystals. Atomic force microscopy (AFM), along with scanning electron microscopy (SEM), is used to examine the etch pits visually. In brief, AFM uses a cantilever and various forces between the tip and sample to deflect the cantilever, which is measured using a laser reflected onto a photodiode [65]. Two modes were used in this study: contact mode and tapping mode. In contact mode, the tip deflection caused by the force between the tip and surface is used as the signal. In tapping mode, the tip oscillates up and down the sample, and imaging is obtained through the intermittent contact with the surface.

Two CZT samples, E1 and E2, were examined for surface defects using etching studies. For this study, the EAg-2 etchant [59] was used to study surface defects for CZT. CZT sample E1, 7.0mm x 7.3mm x 1.0mm, and CZT sample E2, 7.8mm x 4.6mm x 2.4mm, were etched using the EAg-2 solution, consisting of 10mL $H_2O$ : 5mL $HNO_3$ : 2g $K_2CrO_7$ : 1mL of 0.1N $AgNO_3$, for 1 minute under room light. Characterization of the chemically etched surface was performed using atomic force microscopy (AFM) and scanning electron microscopy (SEM). AFM images were produced using an Agilent PicoPlus microscope. SEM images were acquired using an FEI Quanta 200 microscope. Prior to etching, both samples E1 and E2 were characterized using I-V measurements with Au top and bottom contacts to determine their resistivity.

### 5.3.2 Results

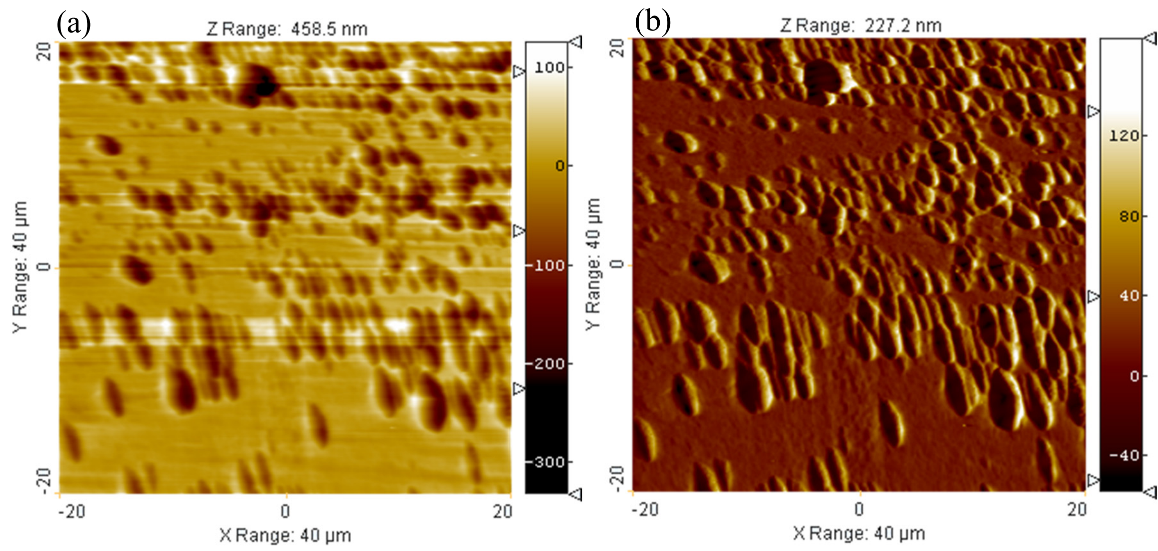


Figure 5.6. (a) Topography and (b) deflection contact-mode AFM images of CZT Sample E1.

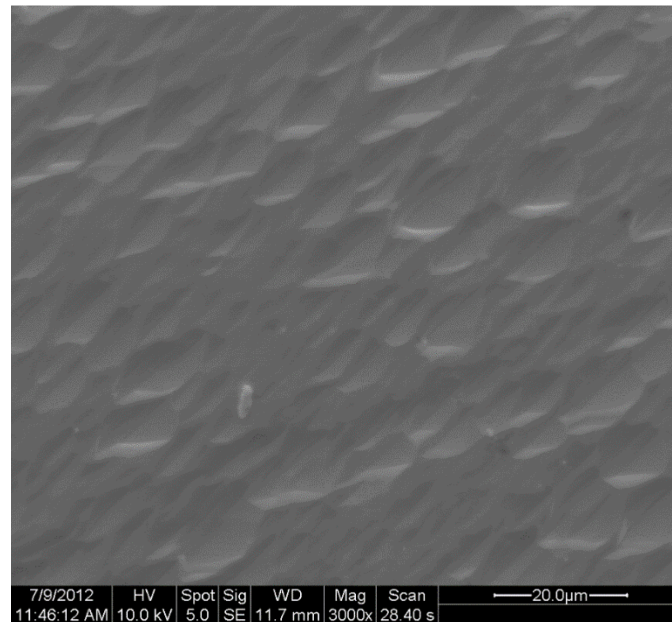


Figure 5.7. SEM image of CZT Sample E1.

Figure 5.6 shows contact-mode AFM images of the etched surface of sample E1 while Figure 5.7 shows an SEM image of the etched surface of sample E1. Both sets of

images depict oval shaped etch pits, approximately 1 to 4 μm in diameter, and ~70 nm deep. Based on the frequency of etch pits seen in the images, the etch pit density of this sample is calculated to be ~$7.5 \times 10^{6}$ $cm^{-2}$.

Figure 5.8a shows a tapping mode AFM topography image of the etched surface of CZT sample E2, and Figure 5.8b shows an SEM image of the etched surface of E2. Both images show triangular etch pits, about 3 to 7 μm in width, and ~80 nm deep. The etch pit density for sample E2 was calculated to be ~$1.2 \times 10^{6}$ $cm^{-2}$.

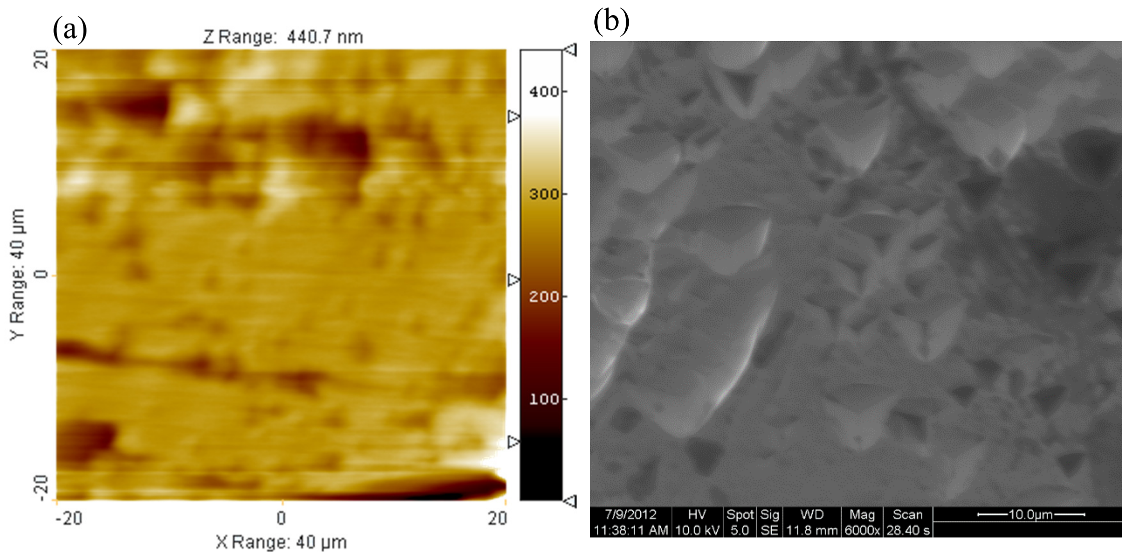


Figure 5.8. (a) Tapping-mode AFM topography image, and (b) SEM image of CZT Sample E2.

Prior to etching the samples using EAg, I-V characteristics were measured from each sample, seen in Figure 5.9. Sample E1 has a calculated resistivity of $2.8 \times 10^{8}$ Ω-cm, while sample E2 has a calculated resistivity of $1.33 \times 10^{10}$ Ω-cm. A summary of the results gathered through etch pit studies is shown in Table 5.2.

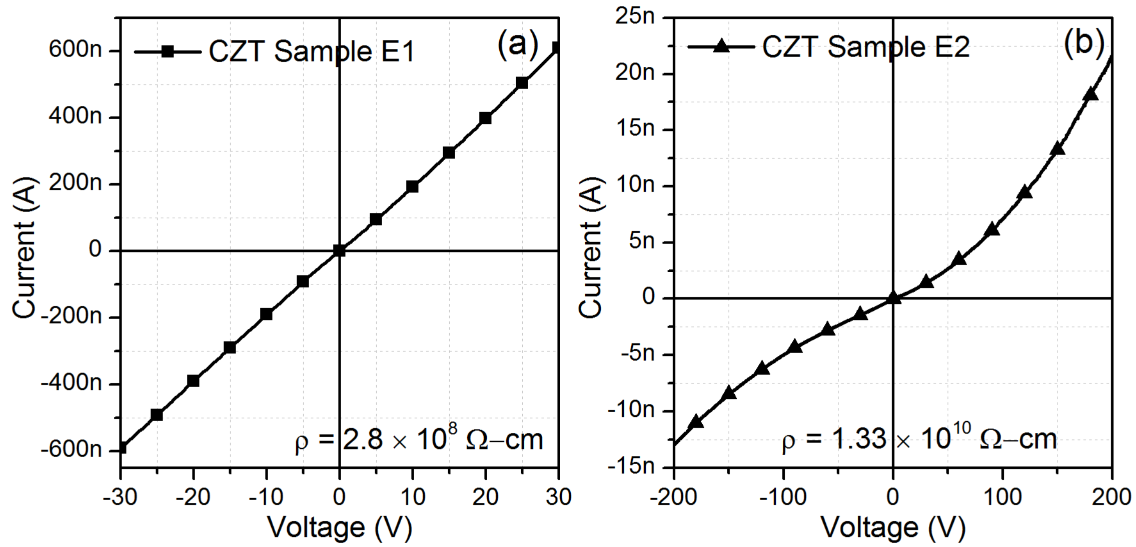


Figure 5.9. I-V characteristics and resistivity calculations for CZT samples (a) E1 and (b) E2.

Table 5.2. Summary of results for etched CZT samples E1 and E2.

| | **Resistivity** | **Etch Pit Density** | **Pit Size** |
|---|---|---|---|
| **E1** | $2.8 \times 10^{8}$ Ω-cm | $7.5 \times 10^{6}$ $cm^{-2}$ | 1 to 4 μm |
| **E2** | $1.33 \times 10^{10}$ Ω-cm | $1.2 \times 10^{6}$ $cm^{-2}$ | 3 to 7 μm |

The etch pit densities for samples E1 and E2 are within one or two orders of magnitude of reported values for CZT in the literature [66]. The etch pits seen on E1 closely resemble flat-bottomed triangular etch pits reported previously [58]. The etch pits seen on E2 resemble pyramidal large-size etch pits, which typically form on (111)B CZT surfaces (Te surface), and etches to a point showing the (110) surface [58, 59]. Both etch pit types are attributed to tellurium edge dislocations [58]. Sample E1 had a much larger concentration of etch pits than sample E2, although the size of etch pits in E1 was smaller than in E2.

The number of etch pits present on the surface of the material has conventionally been used as a measure of crystal quality for semiconductor materials [67, 68]. The resistivity values for E1 and E2 correlate with the etch pit densities, since E1 has a higher concentration of etch pits and a lower resistivity. Sample E2, which has a lower etch pit density, has a higher resistivity and lower leakage current with Ohmic contacts.

## 5.4 Electron Beam Induced Current

### 5.4.1 Background and Experimental

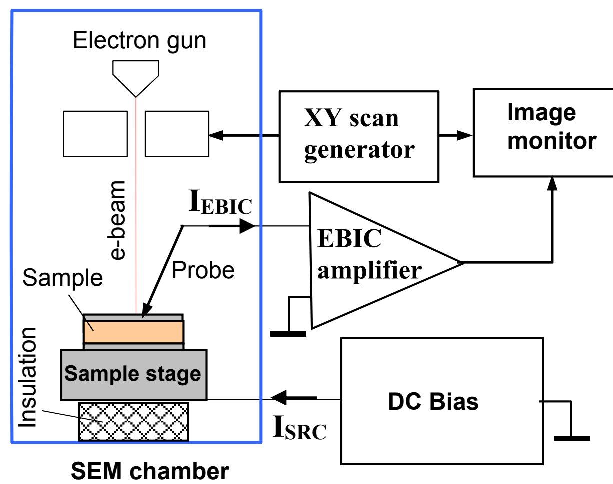


Figure 5.10. Schematic of EBIC setup.

Electron beam induced current (EBIC) is a semiconductor characterization technique which is performed using a scanning electron microscope (SEM). See Figure 5.10 for the schematic of the EBIC setup. In this experiment, the electron beam from the SEM electron gun strikes a p-n or Schottky junction semiconductor device. As the beam scans across the sample, electron-hole pairs are generated in the semiconductor sample, and separated by the internal electric field due to the built-in space-charge region [60]. The resulting signal from the generation of electron-hole pairs at various sample locations is sent to a current amplifier and used as an image signal for the SEM image, creating an

EBIC contrast image. Variations in the generation, recombination, and drift of the electron-hole pairs will result in variations in the contrast of the EBIC image. These variations are most likely caused by the spatial differences in crystal quality and defects within the semiconductor material.

According to the EBIC theory [69], the EBIC contrast of the defect depends on the defect strength $\gamma$ and the point spread function $H^*$ according to the following equations [69]:

$$I_1(\xi,\eta,E) = I_0(E) + I^*(\xi,\eta,E) \quad 5.3$$

$$I^*(\xi,\eta,E) = \iiint_F dxdydz\, \gamma(x,y,z) H^*(x-\xi, y-\eta, z; E) \quad 5.4$$

where $I_1(\xi, \eta, E)$ is the total collected current, x, y, z are Cartesian coordinates, $\xi, \eta$ are the point coordinates in the XY plane where the EBIC current is considered, $I_0(E)$ is the EBIC current in the defect-free semiconductor forming background of EBIC image, $E$ is the energy of the electron beam, $F$ is the region of space occupied by defect, $I^*(\xi, \eta, E)$ is the current contributed by the defect to the total collected current. In the classical theory of EBIC, $\gamma$ and $H^*$ are given by the following equations [69]:

$$\gamma(x,y,z) = 1/L'(x,y,z)^2 - 1/L^2 \quad 5.5$$

$$H^*(x-\xi, y-\eta, z; E) = -qD\exp(-z/L)p_0(x-\xi, y-\eta, z; E) \quad 5.6$$

where $D$ is the minority carrier diffusion coefficient, $L=\sqrt{D\tau}$ is the minority carrier diffusion length in the defect-free semiconductor, $\tau$ is the minority carrier lifetime, $L'(x,y,z)$ is the minority carrier diffusion length in the defective region, $q$ is the magnitude of electronic charge, $p_0$ is the minority carrier distribution. Crystallographic defects often

introduce deep energy levels into the band gap and therefore act as effective recombination centers. Therefore, the minority carrier lifetime in the defect-rich region is lower than that in the defect-free region of the semiconductor and hence $L' \leq L$ resulting in a positive defect strength function and negative $I^*$. Therefore the total collected current in the defect-rich region is lower than that in the defect-free region of the semiconductor. However, this theory does not account for the leakage current which might be significant under electron irradiation and under high bias voltage applied to the sample during EBIC measurements performed in the laboratory. Under bias voltage, current in the defective regions will be higher than current in defect-free regions [70].

EBIC contrast images were taken on a CZT diode using a Schottky contact formed using In and Pt metal electrodes. EBIC imaging was performed using a JEOL-35 SEM, with the CZT sample operated in reverse bias voltage from 50-100V. The sample was then chemically etched using the EAg-2 etching solution (see Section 5.3.1) [59] for 1 minute under room light.

### 5.4.2 Results

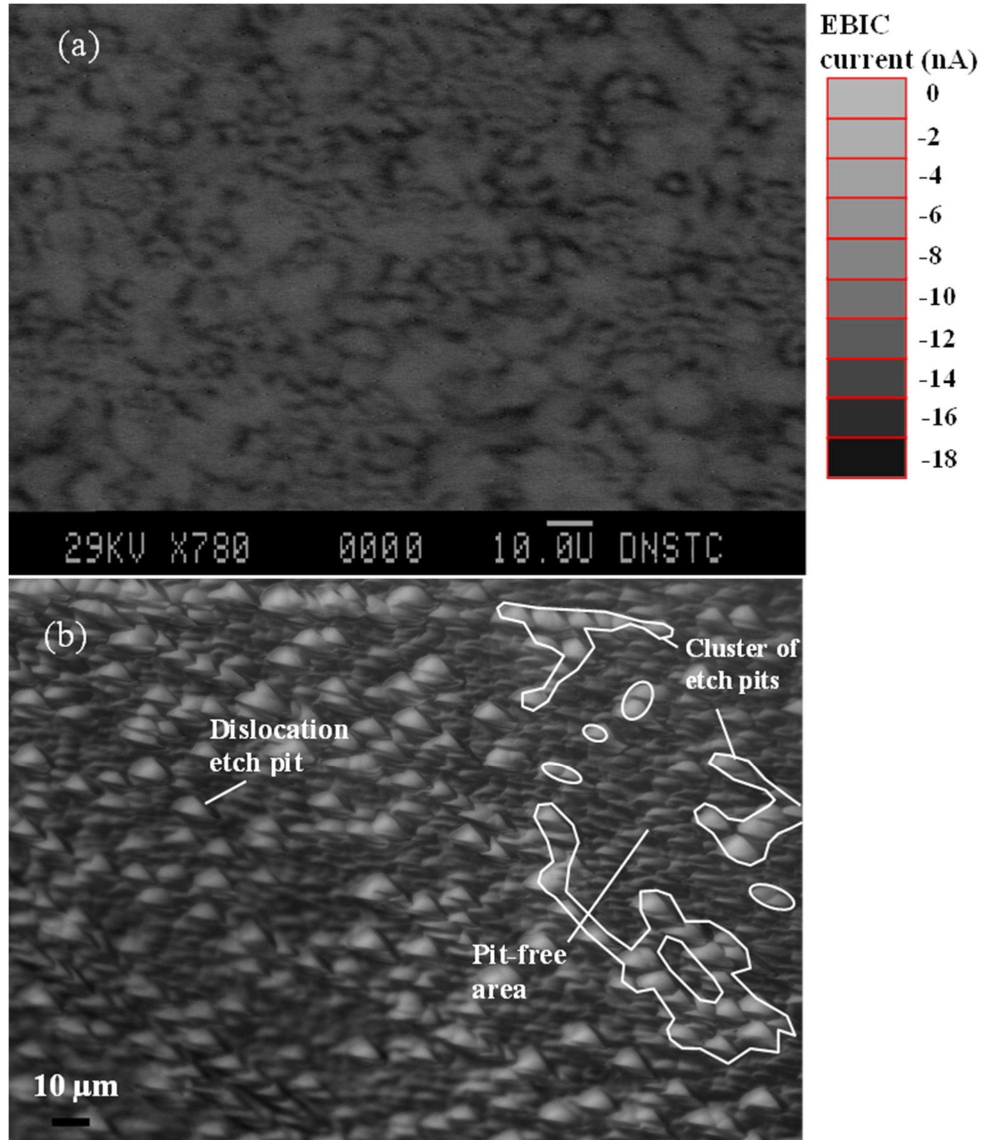


Figure 5.11. (a) EBIC image of a CZT crystal at 80 V reverse bias, and (b) 500X optical image of the of the CZT crystal after chemical etching.

Figure 5.11a shows an EBIC contrast image of the fabricated CZT diode under reverse bias voltage. The image shows interpenetrating dark and white regions, which correspond to high EBIC current and low EBIC currents respectively. EBIC measurements on semi-insulating SiC under voltage bias show that defective regions show higher leakage

current in the contrast image [70]. Therefore, dark regions in Figure 5.11a represent defective regions having high leakage current, while white regions represent areas devoid of any defects. Figure 5.11b shows an optical image of the CZT crystal after defect delineating etching. From this image, it can be seen that the spatial distribution of dislocation etch pits is not uniform with the etch pits that form clusters. When compared to the EBIC image in Figure 5.11a, the dislocations and clusters shown in Figure 5.11b are believed to produce the irregular patterned dark EBIC contrast [71]. Additionally, areas free of etch pits correspond to the white EBIC contrast of the defect-free portions of the CZT crystal. Correlation with the literature suggests the morphology seen in the EBIC image are caused by clusters of point defects and dislocations [72]. This supports the results correlating the EBIC contrast image with defects revealed using the chemical etching.

## 5.5 CONCLUSION

In this chapter, surface and bulk defect analysis was performed on the grown CZT crystals. TSC experiments revealed deep-level defects in the crystal which contribute to hole trapping. Chemical etching, in conjunction with SEM and AFM images, yielded information about the types of surface defects present, and showed a negative correlation between the etch pit density of a CZT crystal and its electrical resistivity. Finally, EBIC results correlated with chemical etching images show that clusters of dislocations and point defects can be seen within the bulk of the CZT crystals. These results give insight on the type and severity of defects present within the solution-growth CZT crystals, which may assist in reducing defects present in future crystal growths.

# CHAPTER 6: DETECTOR FABRICATION AND CHARACTERIZATION

## 6.1 THEORETICAL DISCUSSION OF RADIATION INTERACTION

### 6.1.1 Introduction

Gamma-rays are a form of electromagnetic radiation produced through radioactive decay of the nucleus of an atom. Gamma radiation has frequencies of above $10^{19}$ Hz and energies typically above 10 keV. For radiation detection purposes, gamma photons must first interact with the detector material to produce fast moving electrons within the detector. These fast moving electrons can then be read by front-end electronics to provide information about the incident radiation. Detector materials, such as semiconductors, interact with gamma-ray radiation to produce these fast electrons by one of three methods: photoelectric absorption, Compton scattering, and electron-positron pair production [73]. These three processes are responsible for converting the photon energy of the gamma-ray into electron energy either by causing the photon to disappear completely or to be scattered within the material.

The primary mechanism for converting gamma radiation below 1 MeV is photoelectric absorption, where a photon interacts and energizes an electron within the semiconductor material [73]. This “photo-electron” is ejected from one of the atom’s tightly bound electron shell, with an energy $E_{e-}$, given by:

$$E_{e-} = h\nu - E_b \qquad 6.1$$

In this equation, $E_b$ is the binding energy of the electron ejected from the electron shell. The emission of the photoelectron will produce a vacancy in the bound electron shell, which will be filled through either a free electron or rearrangement of electrons from the outer shells, which will cause the emission of X-ray photons. These X-rays will also undergo photoelectric absorption within the detector material, through a less tightly bound electron shell. This photoelectric process works well for gamma-rays and X-rays, but is enhanced significantly when the material interacted with has a high atomic number (also known as Z). The use of high Z materials increases the probability of interaction of the gamma-ray or X-ray with the material. This is why high Z materials such as cadmium zinc telluride are highly sought after for gamma-ray detection applications.

The second type of process relevant to gamma-ray interaction in matter is Compton scattering. In Compton scattering, the gamma-ray photon interacts within the material, and is scattered relative to its original trajectory [73]. The energy of the scattered gamma-ray is given by the following equation:

$$h\nu' = \frac{h\nu}{1 + \left(\frac{h\nu}{m_0 c^2}\right)(1 - \cos\theta)} \qquad 6.2$$

where θ is the angle of deflection of the gamma-ray, $m_0c^2$ is the rest mass energy of the electron (0.511 MeV), and hν' is the energy of the scattered gamma-ray. Some energy is transferred to an electron present in the material, known as the recoil electron, which depends on the angle of deflection, as seen in the following equation:

$$E_{e-} = h\nu - h\nu' = h\nu\left(\frac{\left(\frac{h\nu}{m_0c^2}\right)(1 - \cos\theta)}{1 + \left(\frac{h\nu}{m_0c^2}\right)(1 - \cos\theta)}\right) \qquad 6.3$$

In this equation, $E_{e-}$ is the kinetic energy of the recoil electron. The more deflected the photon (higher angle), the more energy will be transferred to the electron. In an extreme case, where the gamma-ray has a head-on collision with an electron, and $\theta = \pi$ (meaning a maximum deflection of 180°), the kinetic energy of the recoil electron can be expressed as follows:

$$E_{e-}|_{\theta=\pi} = h\nu\left(\frac{2\left(\frac{h\nu}{m_0c^2}\right)}{1 + 2\left(\frac{h\nu}{m_0c^2}\right)}\right) \qquad 6.4$$

Any angle of scattering is possible within a detector material, with the energy varying for the resulting photon and recoil electron based on the above equations. The probability of a photon being scattered depends on the number of electrons present in the detector material, and is therefore proportional to the atomic number or Z of the material.

In addition to photoelectric absorption and Compton scattering, gamma-rays which have energy above 1.02 MeV (the rest-mass energy of an electron) will undergo pair production. In pair production, the gamma-ray generates an electron-positron pair [73]. However, this research will concentrate on photoelectric absorption and Compton scattering. For all three types of interaction, if a strong enough electric field is applied to the semiconductor, the resulting electron-hole pair will be separated to the contact electrodes and subsequently read out by the detector's front-end electronics as charge.

### 6.1.2 Effect of Detector Size on Gamma Ray Spectroscopy

One important consideration of secondary gamma-ray interactions, or Compton scattering, is that the size of the detector plays a major role in how detrimental Compton scattering affects the primary detection signal. These considerations are very important for CZT, because detector sizes ≥ 1-2 cm$^3$ are very difficult to grow and produce. Furthermore, due to the unique properties of CZT as a radiation detector material, there is significant interest in its performance as a high energy gamma-ray detector. Therefore, the effects of Compton scattering are very important and very significant when using CZT as a nuclear radiation detector, and play a major role in its performance.

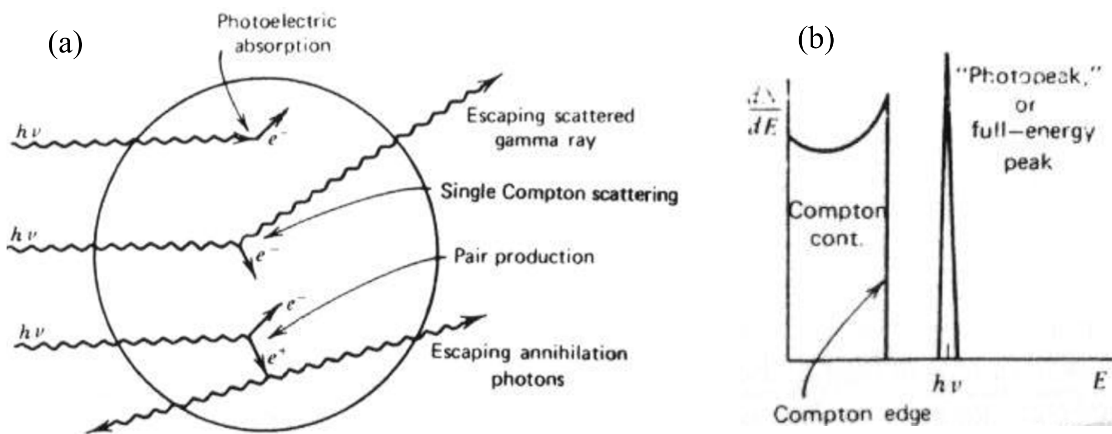


Figure 6.1. (a) Schematic of gamma-rays escaping a detector material after Compton scattering, before having a chance to interact with the detector again [73]. (b) Effect of Compton scattering on detection signal [73].

In Compton scattering, the resulting scattered gamma-ray can travel for several centimeters before interacting with the material again. When a gamma-ray is Compton scattered in a large detector (greater than tens of centimeters), it is likely that all of the energy created by the gamma-ray interaction, whether it be photoelectric absorbed or Compton scattered, is deposited in the detector [73]. This is because even if the gamma-

ray is Compton scattered, the resulting gamma-ray will likely interact with the detector again before escaping outside of the detector.

Detectors in the real world are not realistically tens of centimeters, and so one consequence of this is that the gamma-rays resulting from Compton scattering can escape the detector material, and the detector will not see the escaped energy. Figure 6.1a shows how gamma-rays will escape a small detector before interacting with the detector again. This results in signals lower in energy than what actually interacted with the detector material. Figure 6.1b shows the effects of Compton scattering on the detection signal if not all of the energy is deposited in the detector material. This lower energy region is called the Compton continuum, and the probability of Compton interactions in this region depends on the detector size, as well as the energy of the gamma-rays interacting with the detector.

When gamma-rays of higher energy are Compton scattered, the resulting scattered gamma-rays are more likely to travel farther before interacting with the detector material again. High energy gamma-rays (i.e. > 100keV) will travel longer distances before being scattered than lower energy gamma-rays [73]. If the detector is sufficiently large (> $10cm^3$), the effects of Compton scattering are reduced or eliminated because the scattered photons have a higher probability of interacting with the detector again, and the total charge will be collected. In the case of a detector which is neither big nor small (less than $10cm^3$, but larger than $1cm^3$), some gamma-rays which are Compton scattered will interact again with the detector, while others will escape the detector without further interaction. In this case, only a portion of the radiation signal will be seen in the Compton continuum.

### 6.1.3 Shockley-Ramo Theorem: Output Signal Evaluation

Within a radiation detector, once charge carriers are generated by radiation, they are collected by applying an external electric field. The movement of charge, $q$, through the detector material induces a charge $Q$ on the contact electrodes of the detector, which is then read out by the front-end detection electronics. The charge $Q$ seen by the electrodes depends on the position of the charge carrier inside the detector. The charge $Q$ sensed by the detector can be predicted by calculating the electric field $E$ at every point where the charge $q$ moves through the detector, using Equation 6.5:

$$Q = \oint_S \varepsilon E \cdot \mathrm{d}S \qquad 6.5$$

where $S$ is the surface surrounding the electrode, and $\varepsilon$ is dielectric constant of the detector. Calculating the induced charge $Q$ in this manner is possible, but tedious, since the electric field $E$ will vary as the charge $q$ moves through the detector, and because of the presence of space charges. This means that the electric field will need to be recalculated for every position the charge $q$ moves to within the detector and integrated at every position, until the charge $Q$ is determined for all of the positions, in order to obtain accurate values for the charge $Q$ [74].

A simpler method to determine the induced charge $Q$ caused by a moving charge $q$ was developed by Shockley [75] and Ramo [76]. According to the Shockley-Ramo theorem, the charge $Q$ seen by the electrodes and the induced charge $q$ are related by the following equations:

$$Q = -q * \varphi_0(x) \quad 6.6$$

$$i = qv \cdot E_0(x) \quad 6.7$$

where ν is the velocity of $q$, and $i$ is the current induced at the detector electrodes. $\varphi_0(x)$ and $E_0(x)$ are called weighting potential and weighting field, respectively. The weighting potential and weighting field describe the coupling of charge at any position at the read-out electrode, and the Shockley-Ramo theorem requires the assumption that the read-out electrode have unity potential, and all other electrodes have zero potential [77]. According to the proof of the Shockley-Ramo theorem [74], only one field needs to be calculated, which is independent of the moving charge $q$ and independent of the space charge, as opposed to the prior calculation which required repeated calculations of the electric field. Furthermore, the induced charge $Q$ produced by the moving charge $q$ depends only on the location of the moving charge and the structure or configuration of the device, and not on the voltage applied to the contact electrodes or the space charge. In the following section, it will be discussed how detector structures help in modifying the weighting potential of fabricated detectors.

## 6.2 DETECTOR STRUCTURES

### 6.2.1 Planar Detector

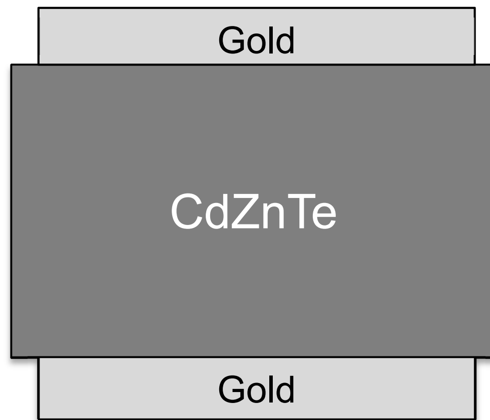


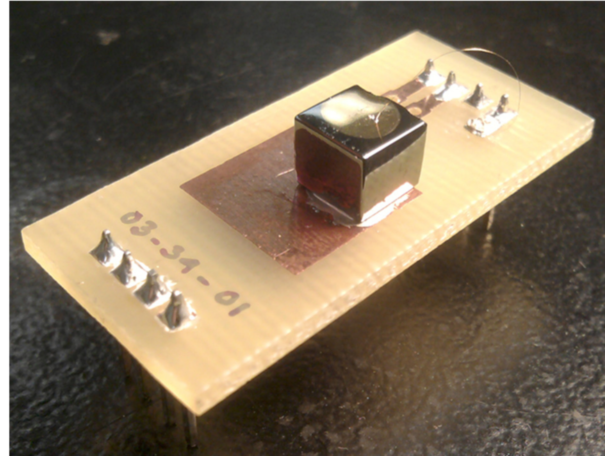


Figure 6.2. Left: Contact electrode schematic of a CZT planar detector. Right: The CZT planar detector P1 fabricated in the laboratory, and mounted on a PCB.

A planar detector, also known as a conventional detector, is the simplest contact electrode structure used to create a radiation detector. The contact schematic, as well as a photograph of the planar detector P1 fabricated in our laboratory, is shown in Figure 6.2. In this structure, large metal contacts are placed on both sides of the detector material. In the planar configuration, gamma-rays will interact with the semiconductor material to produce electron-hole pairs. Assuming positive voltage bias on the anode, electrons will move towards the anode, and holes will move towards the cathode. If the readout signal is taken from the anode, then the weighting potential is considered to be 1 at the anode and 0 at the cathode. For a planar detector configuration, the weighting potential is taken to be a linear function of the interaction location $Z$ within the detector, as seen in Figure 6.3, and given by the following equation [74]:

$$\varphi_0(z) = Z\,, 0 \leq Z \leq 1 \qquad 6.8$$

For a detector where neither holes nor electrons are lost when travelling to the contact electrodes, the charge seen by the electrodes $\Delta Q$ is expressed as follows:

$$\Delta Q = -(he_0)(0 - Z) + (ne_0)(1 - Z) = ne_0 \qquad 6.9$$

where h is the number of holes detected, n is the number of electrons detected, $e_0$ is the electronic charge induced by the radiation, and $Z$ is the interaction depth [74]. In this equation, the energy of the holes and the energy of the electrons sum to equal the total energy seen by the detector before travelling through the semiconductor material. In this case, because both holes and electrons are being read without loss of information, the charge read at the contact electrodes is independent of the depth of interaction.

However, detectors made from CZT suffer from the issue of poor hole transport properties [9]. If the holes are unable to move to the collecting electrode quickly without being lost, then Equation 6.9 is simplified to the following expression for the induced charge seen by the anode:

$$\Delta Q = (ne_0)(1 - Z) \qquad 6.10$$

In this equation, the contribution of holes to the detection signal has been neglected. This means that the charge, and resulting detection signal, is dependent on the interaction depth $Z$ of the moving charge $e_0$. If gamma-rays interact at any depth within the detector, the charge seen by the anode of the detector will vary anywhere between 0 and $ne_0$, due to the dependence on the interaction depth. As a result of this, no useful detection signal can be generated, since even if gamma radiation with a single energy interacts with the detector,

it will appear to have energy equally across the range from 0 to $ne_0$. This limitation of the planar detector structure necessitates the use of other detector structures, which will compensate for the poor hole transport properties present in CZT and similar detectors.

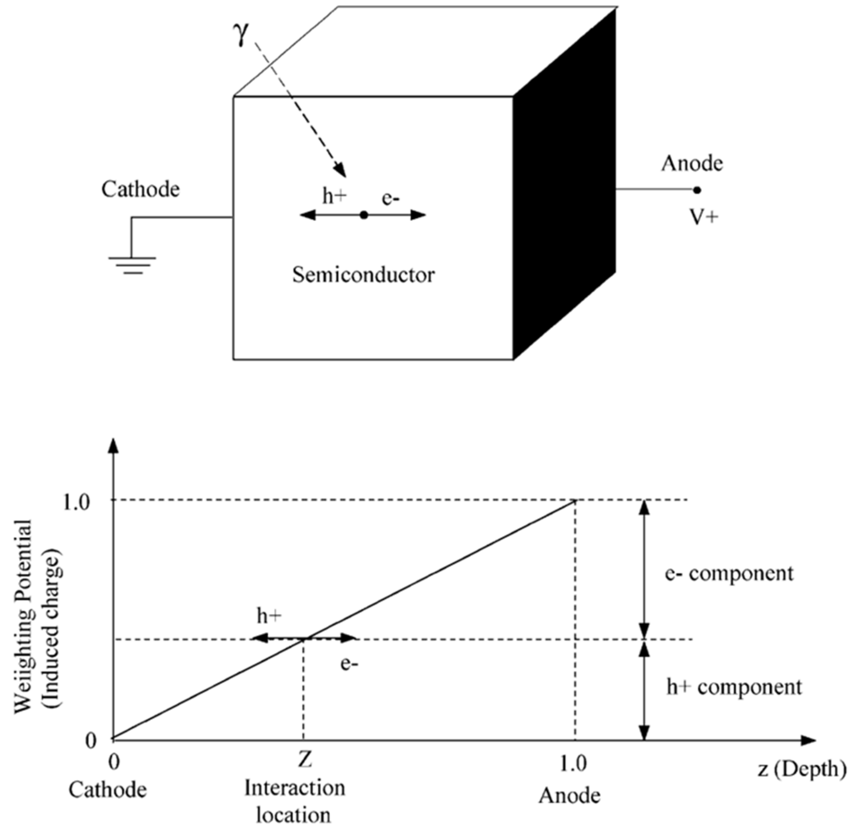


Figure 6.3. Schematic showing the weighting potential seen by the anode of a planar detector, and the contribution of electrons and holes to detection signal [74].

### 6.2.2 Pixel Guard Ring Detector

In order to compensate for the effects of poor hole trapping in planar CZT detectors, specialized detector geometries must be applied to the detectors to have the charge readout to be only due to a single polarity (electron movement in the case of CZT). One such single polarity charge sensing device structure is the small pixel detector. In a small pixel detector, several smaller metal electrodes, separated by a gap, are placed on the detector in a

geometric pattern. These small electrodes are known as pixels. In this configuration, the size of the pixel compared to the detector thickness plays a major role in the charge induced at the anode. The induced charge $Q$ in a small pixel detector can be described by the following equation [78]:

$$Q = q\left[1 - \frac{1-Z}{\sqrt{\alpha^2 + (1-Z)^2}}\right] \quad 6.11$$

where $q$ is the electronic charge, $Z$ is the distance the charge has to travel to reach the anode, and $\alpha$ is the ratio of the approximate pixel radius/width to the detector thickness. The weighting potential for a small pixel detector can thus be written:

$$\varphi_0(z) = \frac{Q(Z=1-z) - Q(Z=0)}{Q(Z=1) - Q(Z=0)} \quad 6.12$$

The weighting potential equation depends on the value of $\alpha$ chosen during detector fabrication. Figure 6.4 shows the variation of the weighting potential as a function of the depth of radiation interaction in a small pixel detector for different pixel size/detector thickness ratios. For large values of $\alpha$ which approach a standard planar configuration, the weighting potential is the same as a planar detector. When $\alpha$ is reduced, the weighting potential near the pixels at a distance of Z = $2\alpha$ becomes far larger than $2\alpha$ away from the pixels. This effect is known as the small pixel effect [79], and because of its effect on the weighting potential, can be used to improve the resolution of a semiconductor radiation detector.

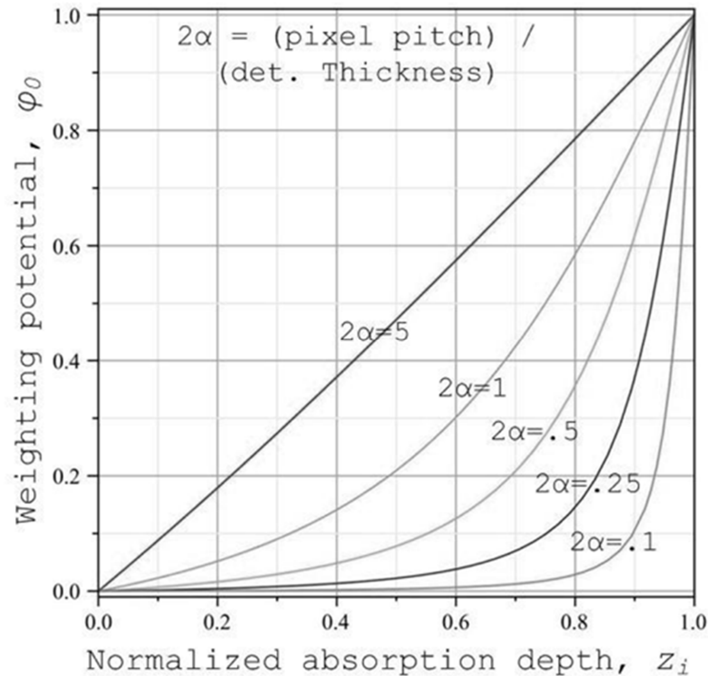


Figure 6.4. Weighting potential of a small pixel detector shown with different pixel pitch/detector thickness ratios [78].

Additionally, one commonly used method to reduce surface leakage current in nuclear detectors is the use of a guard ring. A guard ring structure involves the use of an anode contact electrode, surrounded by a space where only the bare semiconductor surface exists (no contact electrode). After the bare surface, another metal contact is placed, known as the guard ring. Figure 6.5a and b shows the side and top view schematic of a guard ring structure, respectively. Figure 6.5c shows a small pixel detector with a guard ring, detector PGR1, fabricated at Fisk University.

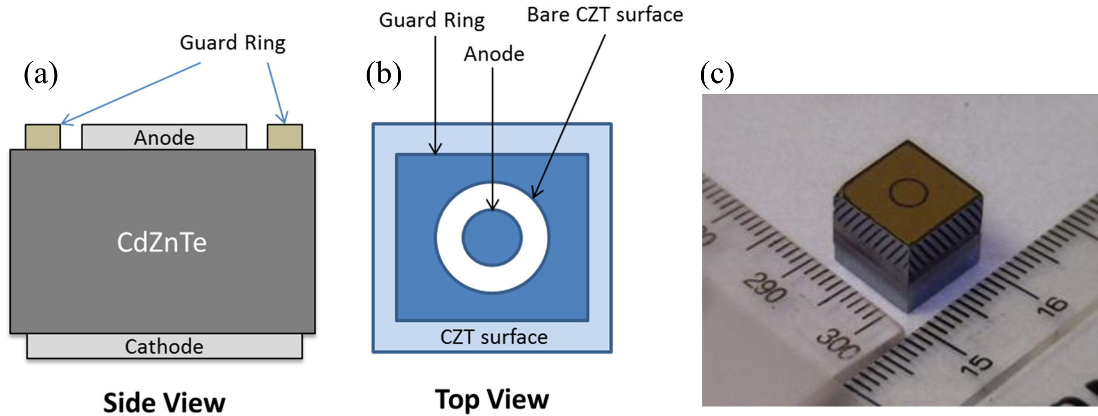


Figure 6.5. (a) Side and (b) Top view schematics of a guard ring structure, (c) Picture of CZT detector PGR1.

In a guard ring structure, the anode is connected to the read-out electronics. The guard ring is kept at the same voltage potential as the anode. In semiconductor detectors, leakage current can flow through the detector bulk or on the detector surface. In both cases, this current will affect the noise performance of the detector. Since the guard ring is not connected to the anode, all current caused by surface conduction will be blocked by the guard ring, and therefore not interfere with the resulting detection signal from the anode. The guard ring structure does not assist with the issue of poor hole transport properties in CZT. It is used to reduce the noise caused by surface leakage current within a detector. It is commonly used in conjunction with another detector structure, such as the planar or small pixel detector geometry. Detector PGR1, seen in Figure 6.5c, utilizes the guard ring with a single small pixel 3.2mm in diameter. The guard ring should improve the signal to noise performance of the detector as compared to a detector where the guard ring is not used.

### 6.2.3 Frisch Collar Detector

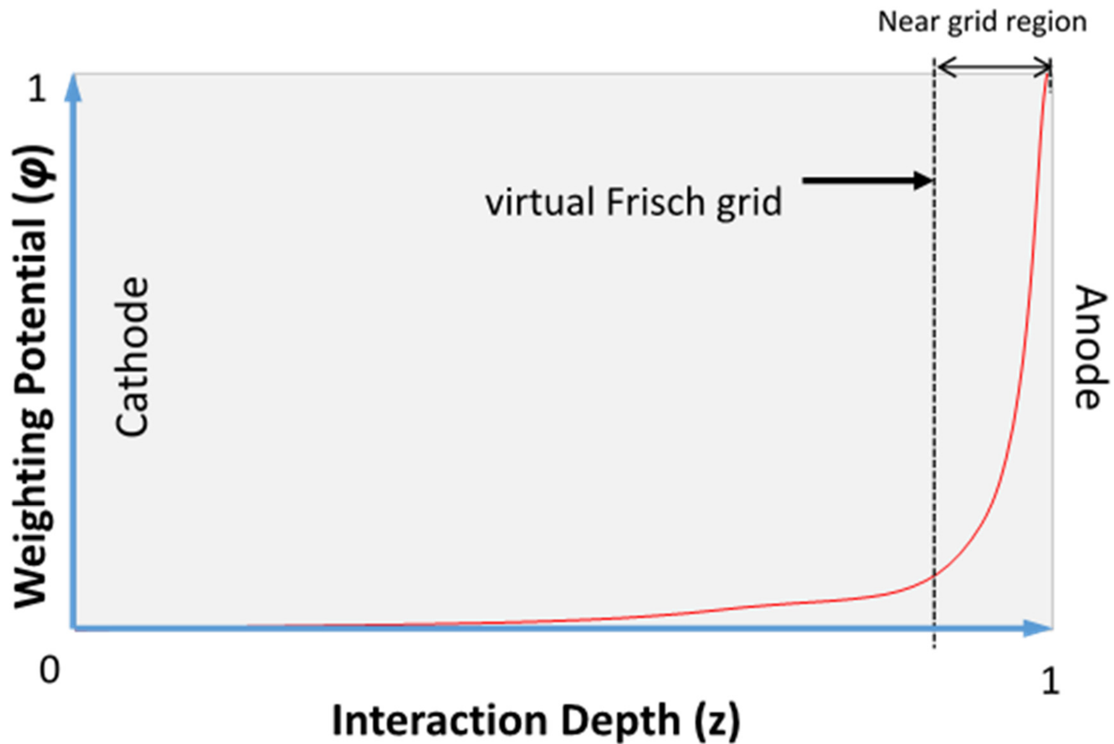


Figure 6.6. Weighting potential of a virtual Frisch grid detector.

The Frisch collar detector structure, also known as a virtual Frisch grid detector, was discovered by D. S. McGregor et.al. for use in semiconductor devices used as nuclear detectors [80]. The origin of this detector structure comes from the Frisch grid ionization chamber, a gas-filled detector used to detect alpha particles [81]. In the Frisch grid ion chamber, alpha particles ionize the gas inside the chamber, which generates electron-ion pairs. Within the chamber is a physical mesh grid placed near the anode, known as the Frisch grid. This grid has an applied positive voltage, which allows electrons to drift towards the grid. Electrons will pass through the Frisch grid and be collected by the anode. The induced charge at the anode as a function of detector depth can be visualized by the

weighting potential diagram shown in Figure 6.6, which applies to both a virtual and physical Frisch grid detector. In this configuration, charge moving between the cathode and grid causes no induced charge on the anode. Only electrons passing through the grid induce a charge on the anode.

The Frisch collar detector structure is a method to create a virtual Frisch grid within a semiconductor device. As seen in Figure 6.7a, the Frisch collar structure is created by using a copper sheath wrapped around a CZT crystal such that the length of the sheath covers the entire detector thickness. The collar is electrically insulated from the CZT crystal by covering the crystal sides with Teflon tape before sheathing in copper, which reduces surface leakage current and prohibits leakage current from flowing through the collar. The copper sheath, also known as the collar, is then connected to the cathode to hold both the cathode and the collar at equal potential. This modifies the electric field lines within the CZT crystal [82] in such a manner that charge due to interactions away from the virtual Frisch Grid will not induce a charge on the anode until the charge reaches the near-grid region of the detector, as seen in Figure 6.6. Figure 6.7b shows the focused electric field present within the CZT detector, which is created by the virtual Frisch grid. This is because, just as in a physical Frisch Grid detector, the electric potential induced by a charge before the near-grid region will not have an effect on the readout electrode since the grid acts as a screen that filters electric potential [82]. Figure 6.7c shows the modeled location of a virtual Frisch grid in the semiconductor bulk due to the modified electric field lines within a Frisch collar detector [82].

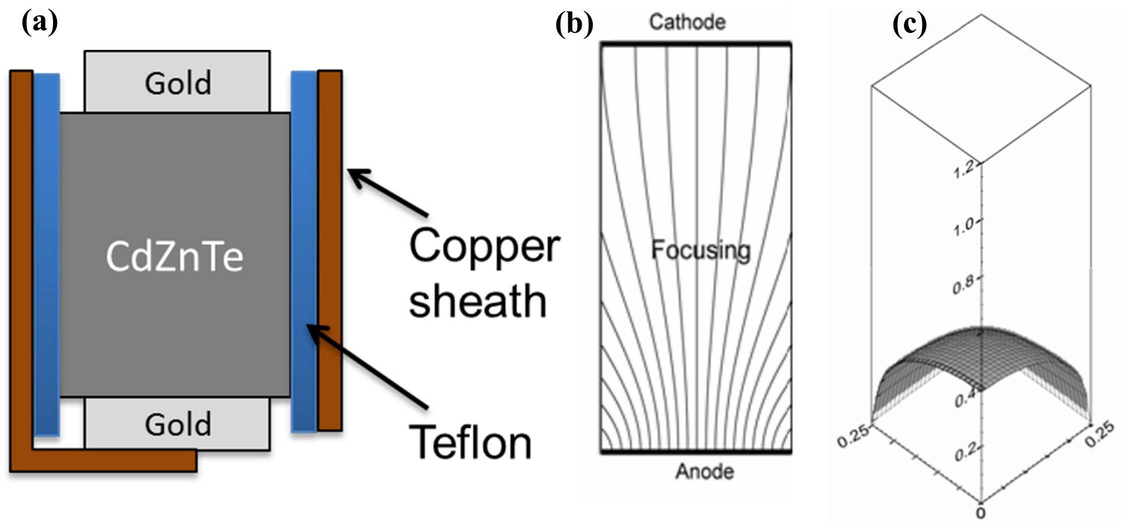


Figure 6.7. (a) Cross-sectional schematic of a Frisch collar CZT detector. (b) Schematic showing the focused electric field within a Frisch collar detector [82]. (c) Schematic showing the location of the virtual Frisch grid within a Frisch collar detector [82].

The Frisch Collar detector structure has several advantages over other structures. It does not require complex data analysis, as seen in the co-planar grid structure. It operates similarly to a planar detector, and is therefore requires less front-end electronics and software development. However, there are geometric limitations on the CZT crystal sizes, due to the focusing of electric field lines caused by the collar. Detectors are preferred to be of smaller size and thicker, in order to create a virtual Frisch Grid in an appropriate location [82]. Two Frisch collar detectors, FG1 and FG2, were fabricated in the lab and are shown in Figure 6.8.

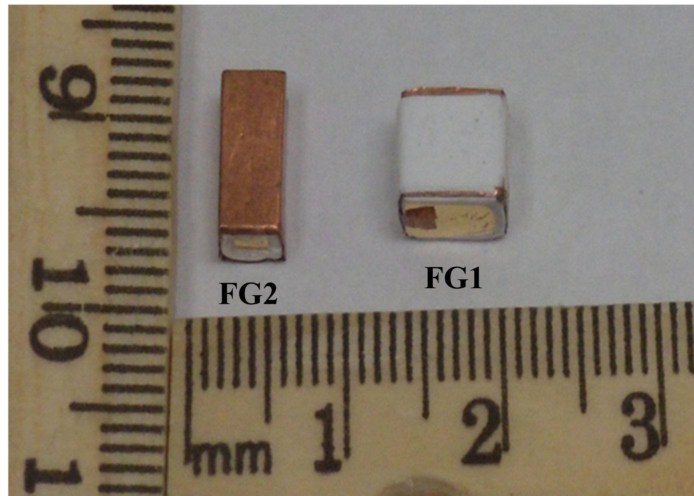

Figure 6.8. Two virtual Frisch grid CZT detectors fabricated in the laboratory. Detector on right is named FG1; detector on left is named FG2.

### 6.2.4 Overview of Studied Detectors

Table 6.1. CZT detectors used for nuclear spectroscopy studies.

| Detector Name | Detector Type | Detector Size (L x W x H) $mm^3$ | Figure Depiction |
|---|---|---|---|
| **P1** | Planar | 6.9 x 6.9 x 4.86 | Figure 6.2 |
| **FG1** | Frisch Grid | 4.2 x 6.2 x 6.5 | Figure 6.8 |
| **FG2** | Frisch Grid | 3 x 4 x 9 | Figure 6.8 |
| **PGR1** | Single Pixel with Guard Ring | 11.3 x 11.3 x 11.1 | Figure 6.5 |

Table 6.1 lists the detectors studied in this chapter. Depending on the detector configuration, some detectors were mounted on PCB boards in order to decrease contact degradation and to improve stability of the detectors. Detectors P1, FG1, CP1, and GR1 are from the same region of one grown CZT ingot, while SP1 and FG2 are originated from other CZT ingots. The differences between grown CZT ingots may result in performance differences between detectors.

## 6.3 ANALOG RADIATION DETECTION

### 6.3.1 Pulse Height Spectrum

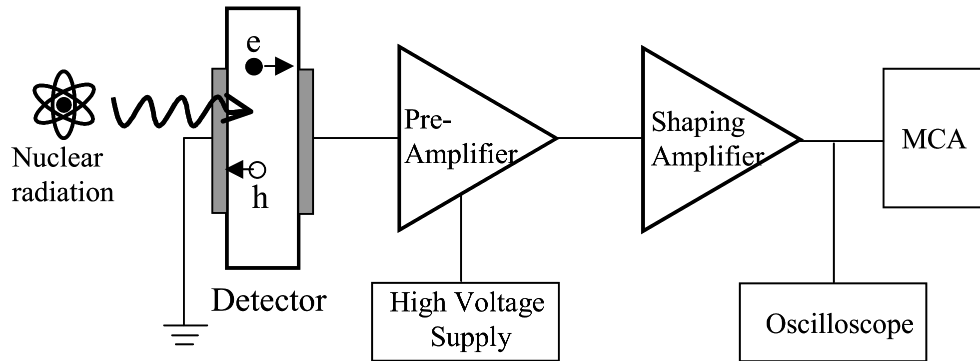


Figure 6.9. Schematic diagram of an analog nuclear detection measurement system.

Once a gamma-ray has deposited its energy into a detector in the forms of electron-hole pairs, the signal is ready to be read by the front-end electronics. Figure 6.9 shows a typical radiation detection measurement setup, which will process the signals produced by the detector into a usable form. The charge signal seen by the detector requires immediate amplification to prevent signal loss, due to the small amounts of charge involved. A preamplifier performs this initial amplification, which will allow the charge signal to be converted to a voltage signal, which can be sent over standard BNC cables to a shaping amplifier.

Preamplification is a mission-critical step in the detection system, because noise introduced in this stage of the detection setup can have a significant effect on the resulting detection spectrum. Figure 6.10 shows a basic charge sensitive preamplifier circuit and the effect the preamplifier has on the signal coming from the detector. A charge sensitive preamplifier at its basic level consists of a high gain amplifier with a feedback capacitor and feedback resistor. The feedback capacitor makes the preamplifier insensitive to

changes in the capacitance of the detector, while adding some noise to the circuit. Furthermore, an FET is usually used at the input of the high-gain amplifier, which must be carefully selected for noise consideration purposes. Preamplifier selection considerations are given in more detail in the section on 'Electronic Noise'.

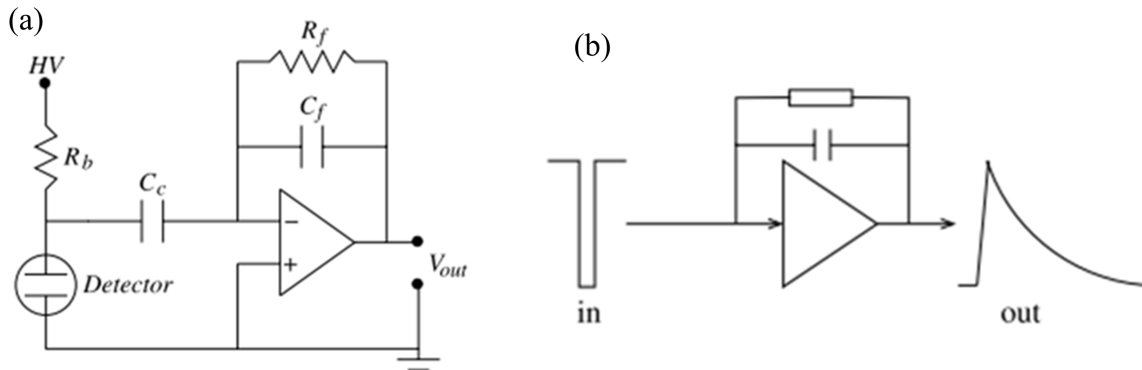


Figure 6.10. (a) Simplified circuit diagram for a charge sensitive preamplifier used in a detection system. (b) Typical input and output pulse shapes seen by a preamplifier [90].

After preamplification, the signal is sent to a shaping amplifier. The preamplifier pulse output contains background noise generated by both the preamplifier circuit and the detector itself. For this reason, these pulses are shaped by a shaping amplifier, which will filter as much noise as possible while preserving information about the energy of the radiation seen by the detector. This is done by passing the preamplifier signal through one stage of differentiation (using a CR, or high pass circuit) and several stages of integration (using an RC, or low pass circuit). Figure 6.11 shows the effect of a shaping amplifier on a preamplifier input signal, as well as the analog circuitry and stages of CR and RC shaping used in a shaping amplifier. The shaping amplifier will spend a certain amount of time, $\tau_m$, measuring the signal, which is also known as the shaping time. This has greater implications for noise, as will be seen in Section 6.3.4, titled 'Electronic Noise'.

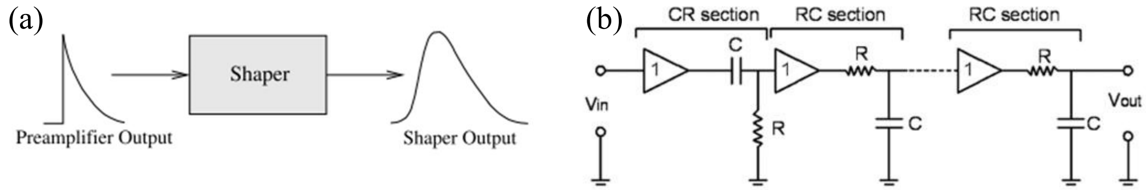


Figure 6.11. (a) Typical input and output pulse shapes seen by a shaping amplifier. (b) Simplified circuit diagram for the various stages of differentiation (CR) and integration (RC) used by an analog shaping amplifier [90].

After shaping, the amplified pulses are sent to a multi-channel analyzer (MCA). The MCA converts the analog signals into digital information containing the height of the shaped pulse (the "pulse height"), and record the number of pulse heights acquired within a given range. The resulting histogram, produced by the MCA is called "Pulse Height Spectrum", which depicts how many counts of radioactive photons interacted with the detector in a given energy window.

## 6.3.2 Experimental

The analog radiation detection experiments are conducted according to the schematic shown in Figure 6.9. A Canberra 3106D high voltage supply biases the CZT radiation detector through an SHV bulkhead. The CZT detector is housed in an aluminum RFI/EMI shielded test box. Inside the box, the detectors are placed either in a PCB holding mount, or one electrode is placed on a gold foil test pad and the other electrode is connected to a pogo-pin contact. Underneath the detector, a $^{241}$Am or $^{137}$Cs nuclear source is placed to irradiate the detector. $^{241}$Am provides low-energy gamma-rays at 59.6keV or alpha particles at 5.486 MeV, while $^{137}$Cs is used for high-energy gamma-rays at 662 keV. See Figure 6.12a for the basic schematic showing the configuration of and connections to the CZT detector. The shielded test box (shown in Figure 6.12b) is connected without using cables to an Amptek A250CF preamplifier through a BNC male-to-male connector, which

is then connected to an Ortec 671 Spectroscopic Amplifier for shaping. The shaping amplifier is then connected to an oscilloscope and a Canberra Multiport IIe multi-channel analyzer. The entire radiation detection setup in our laboratory at USC is shown in Figure 6.12c. Data from the multi-channel analyzer is sent to the Genie 2000 PC software, which generates the pulse height spectrum.

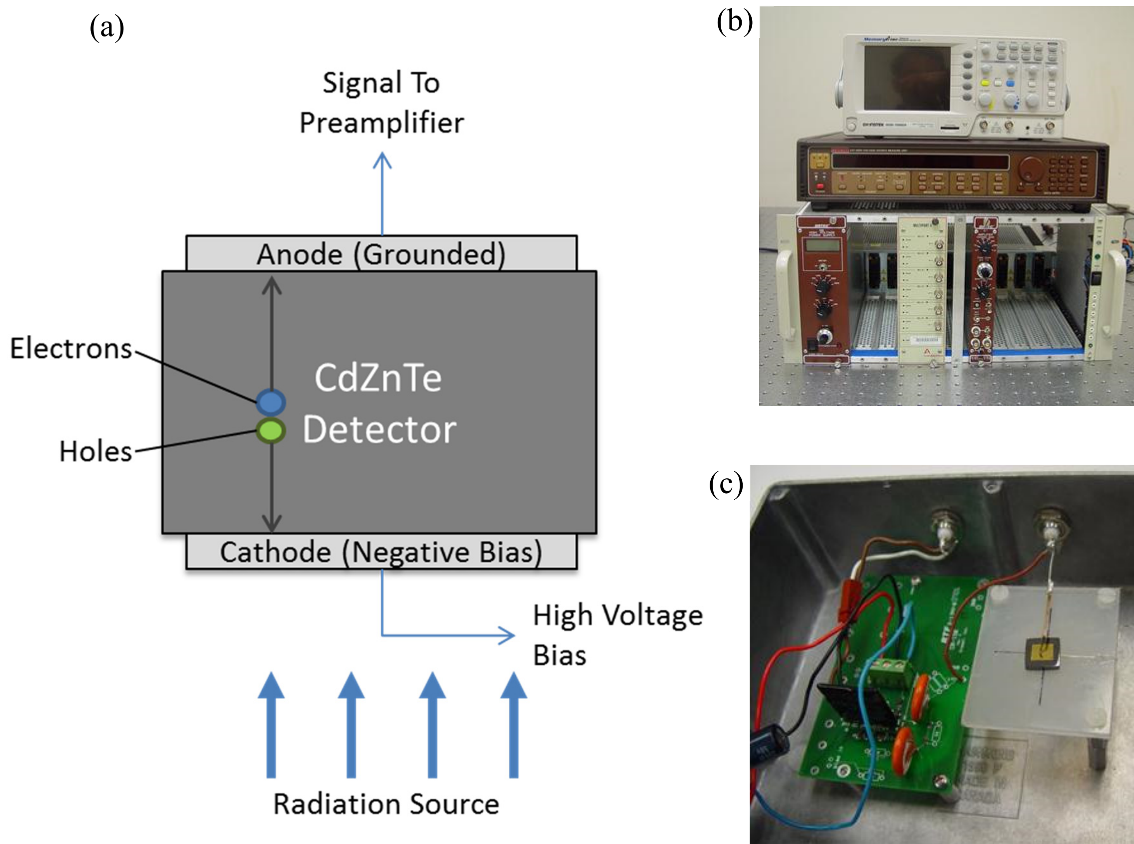


Figure 6.12. (a) Basic connection diagram for a CZT nuclear detector inside of the shielded test box, (b) picture of the radiation detection system at USC, and (c) picture of the shielded aluminum testing box with CZT detector.

Once pulse height spectrum is generated, the full width at half maxima (FWHM) of the gamma-ray energy peak is calculated through Gaussian peak fitting using the Origin

plotting software. The energy resolution of the detector is calculated by the following equation:

$$\% \, Energy \, Resolution = \frac{FWHM \, (keV)}{Incident \, Energy \, (keV)} * 100\% \qquad 6.13$$

where the incident energy is the centroid of the energy peak observed in the pulse height spectrum. Lower values of energy resolution and FWHM indicate better detector performance.

### 6.3.3 Energy Calibration

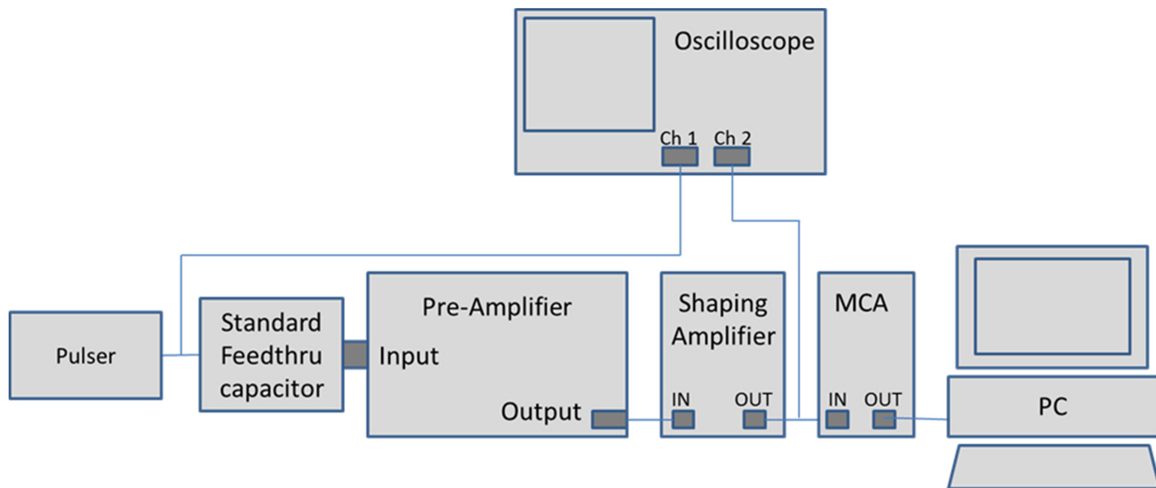


Figure 6.13. Schematic of a radiation detection system under calibration conditions.

Before the detection system can give relevant information about the energy of detected radiation, it must be calibrated. This is because the various parameters within a detection system, such as the gain of the preamplifier and shaping amplifier, the shaping time of the amplifier, and the noise present in the system, will contribute to changes in the pulse heights seen at the output of the shaping amplifier. In order to correlate the pulse

height of a detection signal with its corresponding energy, calibration must be done under the same settings and similar configuration as the setup used to test a radiation detector.

In order to calibrate the system, a pulser, which generates waveforms and simulates the output of a radiation detector, is connected to the detection system through a capacitor. Figure 6.13 shows the configuration of the detection system during calibration. Pulses of fixed heights ($V_{pulser}$) are fed into the pre-amplifier input generated by the pulser through a feedthrough standard/calibrated capacitor ($C_{test}$) and pulse-height spectrum is acquired. The energy of the charge pulses from the capacitor, $E_{pulser}$, can be determined using the following equation:

$$E_{pulser}(keV) = \frac{V_{pulser}(mV) \times W\left(\frac{eV}{ehp}\right) \times C_{test}(pF)}{1.6 \times 10^{-19}} \tag{6.14}$$

where $W$ is the electron-hole pair creation energy of the semiconductor detector being tested. The corresponding pulser peak position in terms of channel number of the MCA is also acquired. The pulse height is systematically changed via the pulser to generate several peak positions relative to the pulser energies. A graphical plot between $E_{pulser}$ and corresponding MCA peak positions for different pulse heights gives the calibration graph. Figure 6.14a shows one MCA spectrum with various pulser peak-positions taken during calibration, and Figure 6.14b is the corresponding calibration graph equivalent to a CZT detector crystal with a typical shaping amplifier and MCA settings. Using the calibration equation, values obtained in terms of MCA channel numbers are converted to energy units in keV.

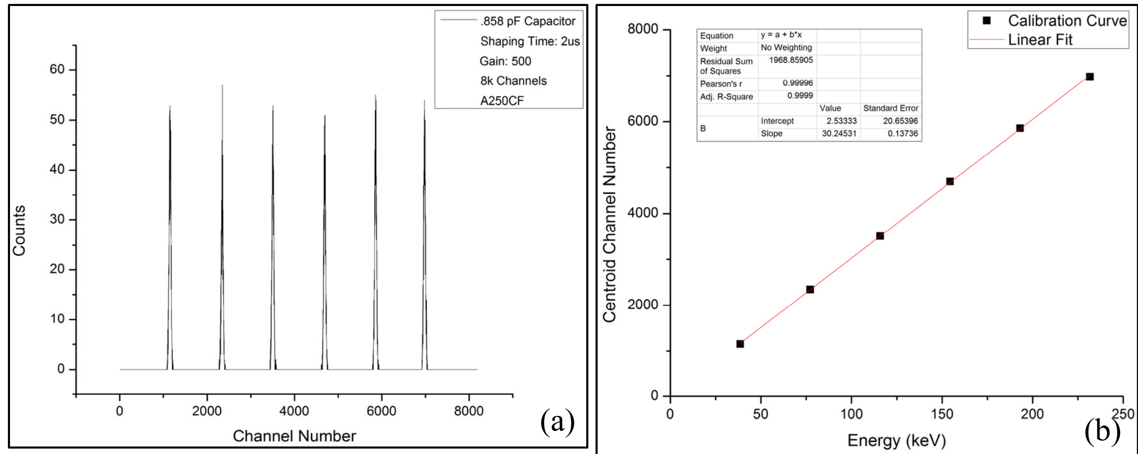


Figure 6.14. (a) Pulse height spectrum obtained for six different pulse sizes, and (b) Corresponding calibration curve.

## 6.3.4 Electronic Noise

In a radiation detection system, there are several sources of noise, which contribute to random fluctuations present in the detection signal. There are mainly three types of noise present which affect detection systems: thermal noise, shot noise, and flicker noise. Thermal noise is generated by the random thermal motion of charge carriers within an electrical conductor. Thermal noise appears approximately white, and therefore appears uniformly throughout the frequency spectrum. The voltage noise variance $v_n$ for a given signal experiencing thermal noise for a resistor $R$ is given by the following equation:

$$v_n = \sqrt{4k_b TR\,\Delta f} \qquad 6.15$$

where $k_b$ is Boltzmann's constant, $T$ is the temperature, and $\Delta f$ is the bandwidth. Since thermal noise affects detectors just as it affects other electrical components, and since thermal noise depends on temperature, some detectors such as high-purity germanium are cooled to liquid nitrogen temperatures to reduce thermal noise.

The second type of electronic noise in detection systems is shot noise. Shot noise is comprised of random statistical fluctuations in the electrical current of a DC circuit, due to the discrete nature of charge. The current noise $\sigma_i$ for a signal is given by the following equation:

$$\sigma_i = \sqrt{2qI\,\Delta f} \qquad 6.16$$

where $q$ is the elementary charge of an electron, $\Delta f$ is the bandwidth, and $I$ is the DC current flowing in the circuit. Bias voltages applied to the detector, which induce a DC current flow across the detector, is an example of shot noise in a detection system. The third type of electronic noise in detection systems is flicker noise, also known as $1/f$ noise. Flicker noise is caused by statistical resistance variations which play more of a role in lower frequency signals than in higher frequency signals. One source of flicker noise in front-end electronics is generation and recombination noise in a transistor due to base current, for example.

The preamplifier circuit in a detection system is responsible for a large portion of the series and parallel circuit noise present in a detection signal. The series resistances and parallel resistances are sources of thermal noise within the detection system. The very first circuit element the detector will see within the preamplifier is the initial FET amplifier. Therefore, it is essential that this FET as well as the preamplifier circuitry is designed well, and it is preferred that the FET is cooled properly in order to reduce thermal noise. For our radiation detection laboratory, we compared the noise performance of two charge sensitive preamplifiers: Amptek A250CF and Cremat CR110. Amptek has used a thermoelectrically cooled FET with a special enclosure, and has tuned the components of the preamplifier to reduce noise, whereas Cremat's design does not make these design considerations. After

calibating both preamplifiers, a single-energy peak of significant counts was generated by the pulser and recorded by the MCA for each preamplifier. The full width at half maxima (FWHM) of these pulser peaks was then calculated.

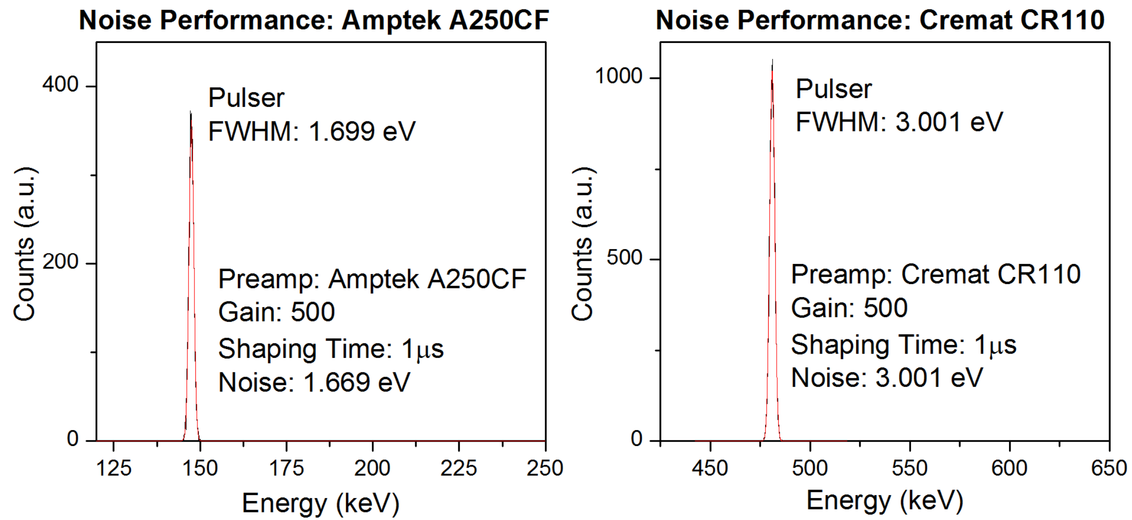


Figure 6.15. Pulser peaks generated for Amptek A250CF and Cremat CR110 charge sensitive preamplifiers in a calibration configuration (using CZT equivalent detector calculation).

Figure 6.15 shows a comparison for both preamplifiers on the basis of noise performance. Under calibration conditions, since there is no detector connected to generate noise, the only significant contribution of noise is the preamplifier circuitry. After calculating the FWHM of each peak, the noise performance of the Amptek A250CF is 1.699 eV, while the Cremat CR110 has a noise performance of 3.001 eV. This means that the CR110 preamplifier is nearly twice as noisy as the A250CF. This result is very meaningful, because this noise affects all experiments involving an actual detector present in the detection system. For this reason, Amptek's A250CF was chosen as the primary preamplifier for detection measurements.

While the primary function of a shaping amplifier is to further amplify the preamplified output signal, its other main function is to reduce the noise of the signal. In order to accomplish this, the shaping amplifier has two primary parameters which control its function: the gain multiplier, and the shaping time. Since the shaping amplifier employs a high pass and low pass circuit to shape the preamplified signal, the shaping time refers to the upper cutoff frequency of the preamplifier signal.

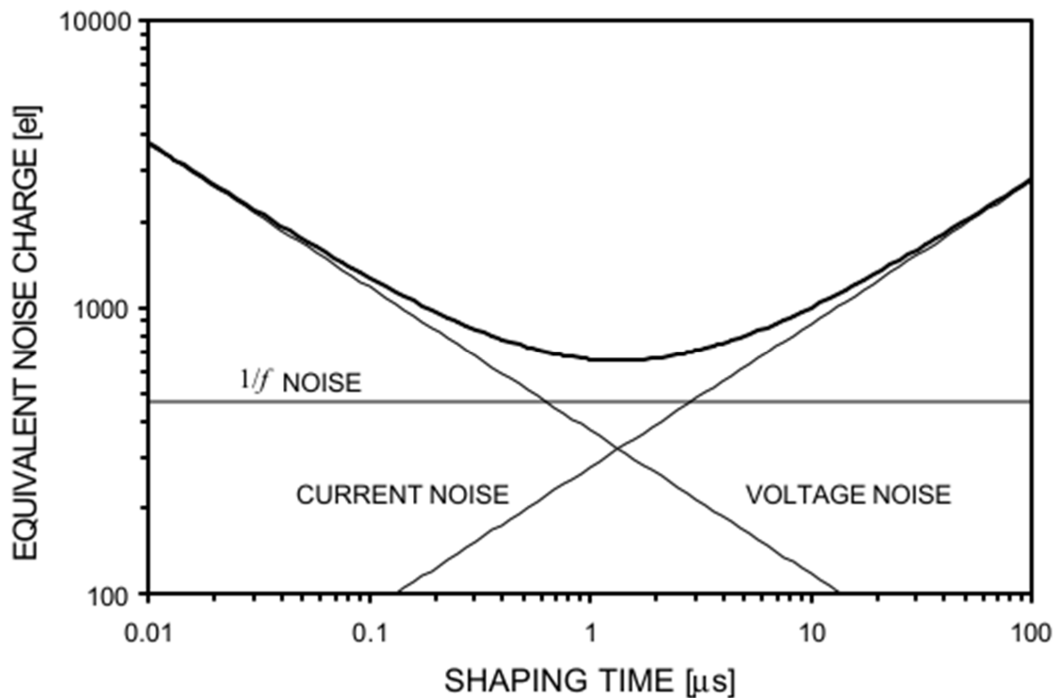


Figure 6.16. Relationship between spectroscopic amplifier shaping time and equivalent noise present in a radiation detection system. [77]

The total noise present after the signal leaves the shaping amplifier is given by the graph shown in Figure 6.16. The graph shown in Figure 6.16 has been derived from the following equation [77]:

$$Q_n^2 = \left(\frac{e^2}{8}\right)\left[\left(2q_e I_D + \frac{4kT}{R_P} + i_{na}^2\right) * \tau + (4kTR_S + e_{na}^2)\frac{C_D^2}{\tau} + 4A_f C_D^2\right] \qquad 6.17$$

where $Q_n$ is the equivalent noise, $q_e$ is electronic charge, $I_D$ is the DC current flowing through the detector, $k$ is the Boltzmann's constant, $T$ is temperature, $Rp$ is any shunt resistance present from the detector to the preamplifier, $i_{na}$ is amplifier current noise, $Rs$ is any series resistance present from the detector to the preamplifier, $e_{na}$ is amplifier voltage noise, $C_D$ is the detector capacitance, $A_f$ is $1/f$ noise, and $\tau$ is the shaping time. In the equation, $\left(2q_e I_D + \frac{4kT}{R_P} + i_{na}^2\right) * \tau$ is the contribution of current noise in the detection system, $(4kTR_S + e_{na}^2)\frac{C_D^2}{\tau}$ is the contribution of voltage noise, and $4A_f C_D^2$ is the contribution of $1/f$ noise. Ultimately, this means that Figure 6.16 shows that both current noise and voltage noise are dependent on the shaping time $\tau$, while $1/f$ noise is independent of shaping time.

### 6.3.5 Effects of Shaping Time and Bias Voltage Variation

In order to determine the effect of varying the bias voltage and shaping time on the noise performance of the analog detection system and the CZT nuclear detectors, the Frisch Collar detector FG1 was tested under various voltages and shaping times using an $^{241}$Am source. Figure 6.17a shows the effects of bias voltage variation for the pulser resolution and $^{241}$Am gamma-ray photopeak resolution, while Figure 6.17b shows the effects of bias voltage variation on the $^{241}$Am peak centroid for detector FG1. The peak resolution and the peak centroid both contribute to the calculation of the percent energy resolution of a detector, as seen in Equation 6.13. In Figure 6.17a, the photopeak resolution increases with

increasing bias voltage until 550V, after which the resolution saturates and increases slightly. Increased bias voltage will improve charge collection within a detector due to a stronger applied electric field, however it will also increase the leakage current, which increases noise. The pulser resolution shows the effects of the leakage current and electronic noise on the output signal. The pulser resolution increases steadily until 550V before behaving inconsistently. Additionally, Figure 6.17b shows the photopeak centroid versus voltage bias for FG1. The photopeak centroid is proportional to the charge collection efficiency of the CZT detector. The centroid values rise sharply until about 500V before saturating. These results show that at low bias voltages, improved charge collection efficiency occurs due to the increased electric field, which improves detector energy resolution. At high bias voltage, charge collection efficiency improvements are less significant due to the electric field fully depleting the detector of space charges, whereas leakage current and electronic noise effects can degrade the detector energy resolution.

Figure 6.18 shows the effects of shaping time variation on the pulser resolution and $^{241}$Am gamma-ray photopeak resolution for detector FG1. The photopeak resolution was best at 1μs shaping time, while the pulser resolution steadily increased with increasing shaping time. This result confirms the equivalent noise vs. shaping time relationship shown in Figure 6.16, suggesting that an optimum shaping time (in this case, 1μs) must be used in order to effectively apply the noise reduction capability of a shaping amplifier.

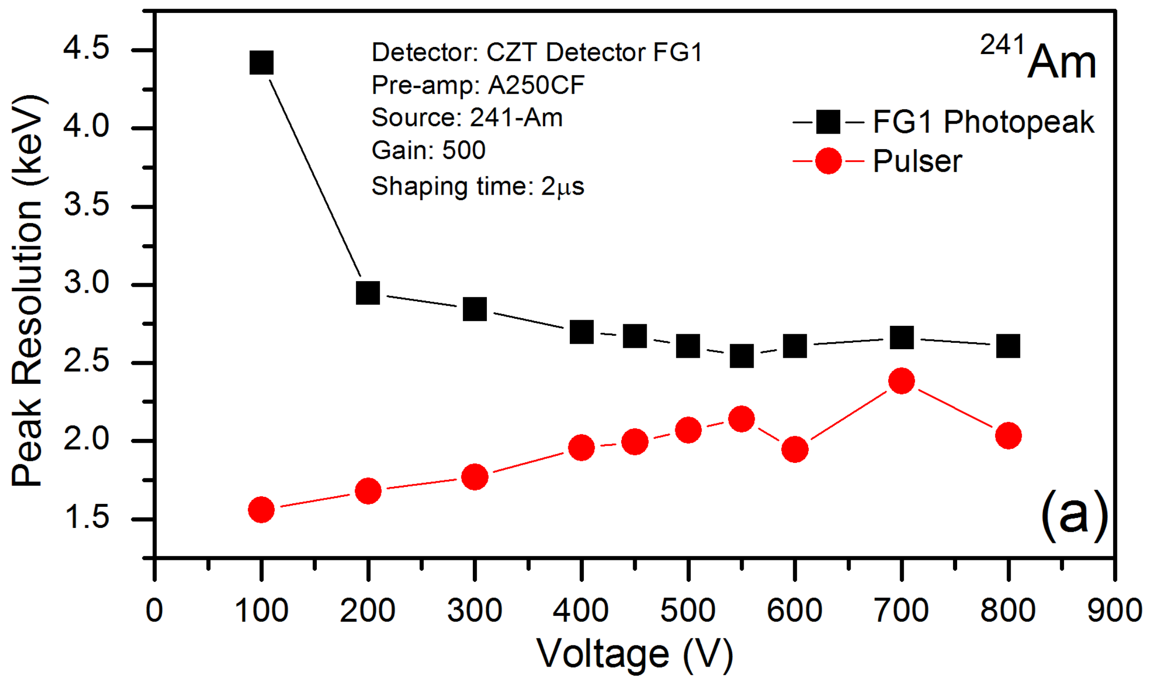


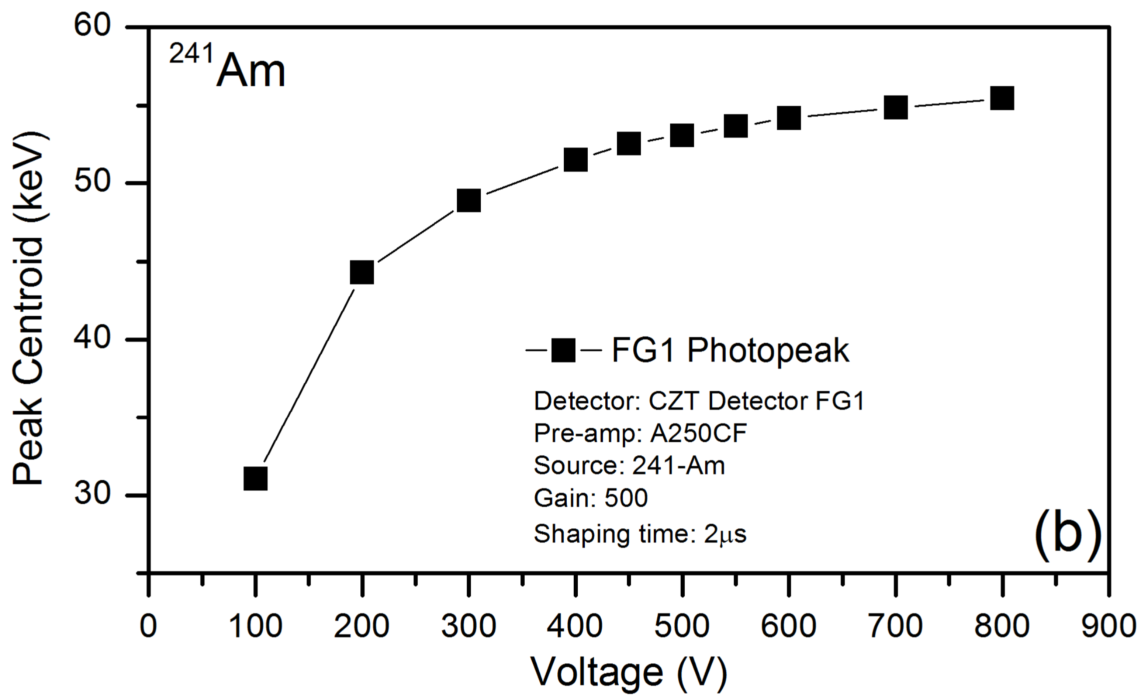


Figure 6.17. Effects of varying voltage bias for detector FG1 under $^{241}$Am irradiation on (a) photopeak and pulser resolution (lower is better), and (b) peak centroid (higher is better)

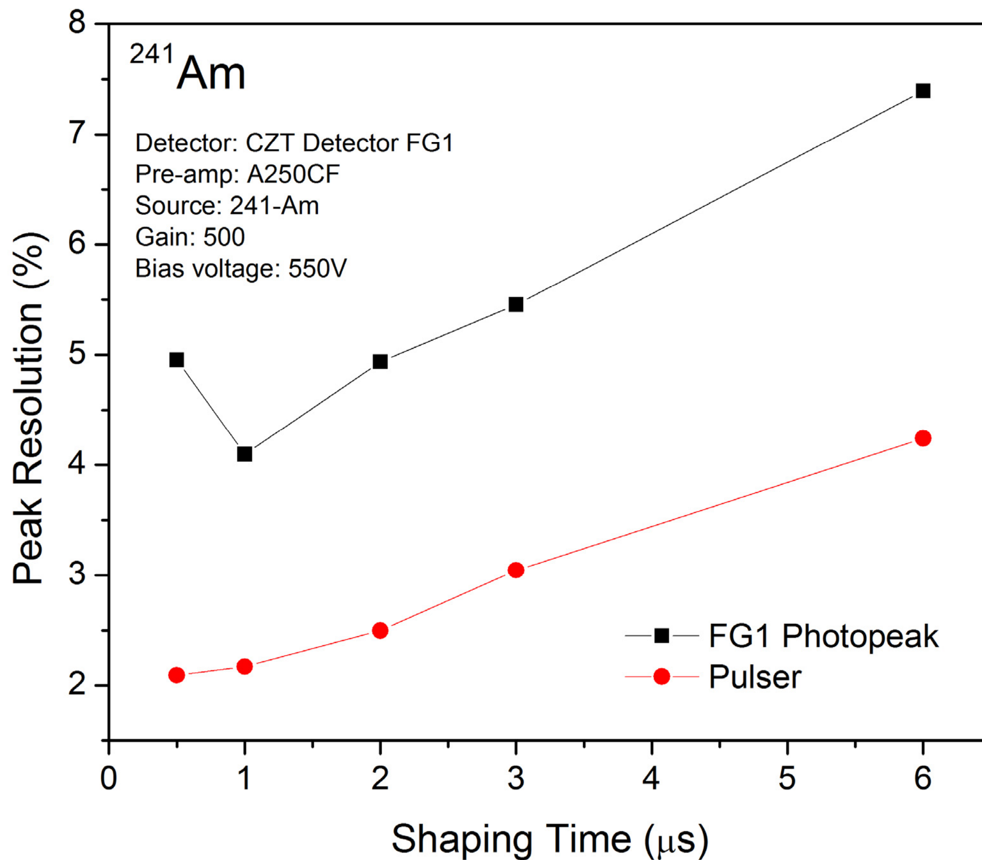


Figure 6.18. Peak and pulser resolution for detector FG1 taken with varying amplifier shaping times under $^{241}$Am irradiation (lower is better).

## 6.4 DIGITAL SIGNAL PROCESSING FOR RADIATION DETECTION

### 6.4.1 Background

Historically, analog pulse-shaping has been the only option for processing signals produced by radiation detection systems due to the high speed and accuracy required. However, in the past two decades, high-speed analog-to-digital converters (ADC) with high resolution have been invented, which allow digital processing of signals produced by radiation detectors. This allows for a wide variety of new data processing techniques to be applied to the radiation detection signals. Additionally, there are a number of advantages

gained by processing detector signals digitally. Digital processing allows for unlimited flexibility in implementing and changing shaping parameters, such as the shaping time, which is limited for analog circuitry. Furthermore, digital processing in theory will be more stable, because the processing will not depend on cable or environmental noise which can affect an analog system. However, one potential disadvantage of digital systems is that they may not be as fast as their analog counterparts.

For the purposes of radiation detection, two parameters are very important when performing analog-to-digital conversion of the signal: the ADC resolution, and the sampling rate. The resolution governs how accurately the digitizer can convert the analog voltage amplitudes to a digital value. A digitizer appropriate for radiation detection must have good ADC resolution in bits, while being able to sample the signal at a high frequency.

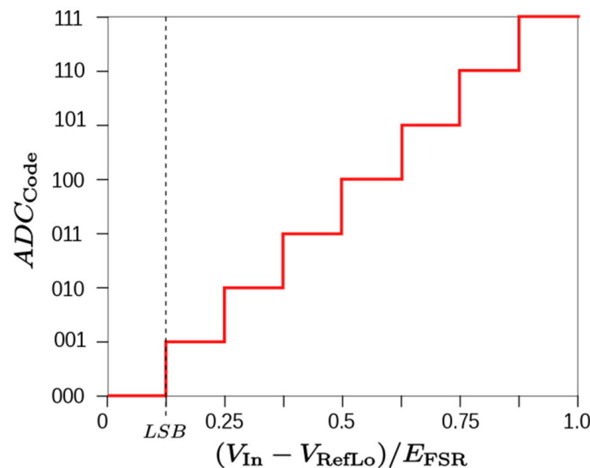


Figure 6.19. An example of an ADC coding scheme for an 8-bit resolution ADC [83].

A digitizer will convert the analog signal based on the coding scheme used for the ADC, which depends on the resolution of the ADC. Figure 6.19 shows an example of a coding scheme for an 8-bit digitizer. Depending on the number of bits of resolution available, the ADC will more accurately be able to store the analog voltages. If the

resolution is too poor, information will be lost from the signal being digitized. The voltage resolution, $V_{res}$, of an ADC can be determined by the following equation:

$$V_{res} = \frac{E_{FSR}}{2^M - 1} \tag{6.18}$$

where $E_{FSR}$ is the voltage range being measured, and $M$ is the ADC resolution in bits. If a signal ranging from 0 to 10V is divided into the code levels available for an 8-bit ADC, then:

$$V_{res} = \frac{10 - 0}{2^8 - 1} = \frac{10}{255} = 39.2\ mV \tag{6.19}$$

This means that an 8-bit ADC will resolve voltage levels in steps no less than 39.2 mV. For the purposes of radiation detection, this means an 8-bit ADC is not suitable, because voltage signals produced by a charge sensitive preamplifier can be as low as 10 mV in peak-to-peak amplitude.

For our laboratory, we have chosen to use a National Instruments NI-5122 digitizer card to perform digitization of detection signals. The NI-5122 has 14 bits of ADC resolution, which gives a $V_{res}$ value of 0.61mV over a 10V range. This resolution is adequate enough to capture pulse information about small or large pulses generated by the radiation detectors. Furthermore, the NI-5122 can capture signals at a rate of 100 Megasamples per second in real-time at 14-bit resolution. This sampling rate is fast enough to capture detector signals and reconstruct them for future use.

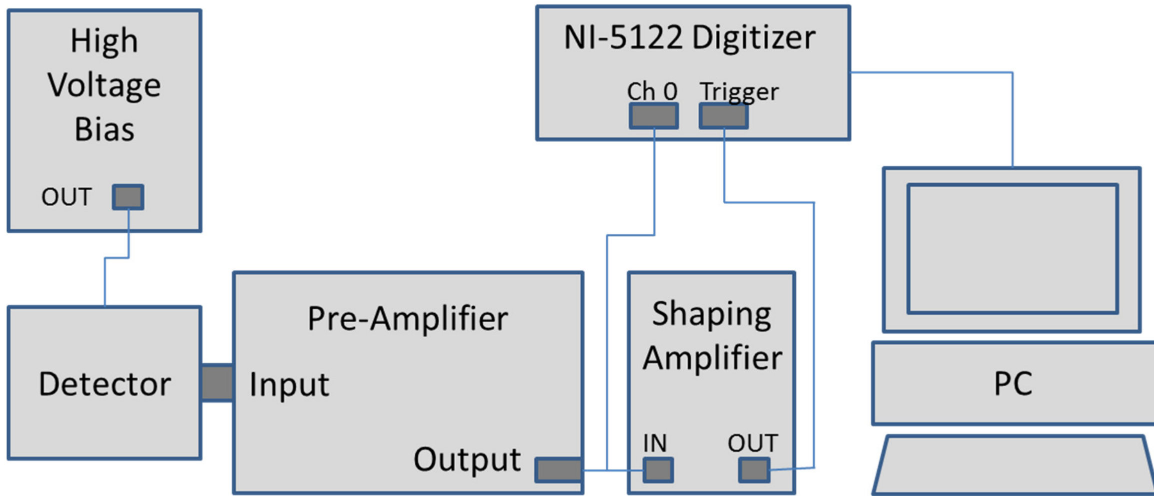


Figure 6.20. Schematic diagram of a digital nuclear detection measurement system.

In order to capture radiation detection pulses from a detector, the radiation detection system was configured in the manner shown in Figure 6.20. A CZT detector biased under high voltage is connected to the preamplifier, which sends its signals to the NI-5122 digitizer card. The pulses are also sent to the shaping amplifier, whose output serves as a reliable external trigger for the NI-5122. The NI-5122 resides within the PC, where the Labview software coded in-house captures the detection signals received and stores it for later use.

### 6.4.2 Digital Pulse Shaping

Once the detection pulses are stored, they must be shaped using a filtering algorithm. Pulse shaping typically uses a linear time-invariant filter, which convolutes the input signal with a filter which does not change its properties based on time. The convolution process for a digital signal can be expressed by the following equation:

$$S(j) = \sum_{i=j-L}^{i=j} V(i)H(j-i) \qquad 6.20$$

where $i$ is the time period between signal sample values, $L$ is the filter length, $V$ is the original signal, $H$ is the response of the filter, and $S$ is the discrete output signal. As the filter $H$ is convoluted through the original signal values $V$, a discrete shaped signal $S$ will be generated.

For analog nuclear detection systems, the most common pulse shaping method employed is CR-$(RC)^n$ shaping. This method, as seen in Figure 6.11, uses one differentiator circuit followed by n integrator circuits wired in series [84]. This style of filter is known as a semi-Gaussian filter, because the resulting pulse shape approximates the Gaussian shape. More integrator circuits provide more noise filtering and further approximation to a Gaussian signal. However, this increases the delay present in processing the signals, and increases the complexity and the number of components present in the processing system. Furthermore, noise reduction suffers from diminishing returns when increasing the integrator circuits [84]. For this reason, in pulse height measurements the typical value of n used is 4.

In a digital system, in order to use a filter on a discrete signal, the transfer function of the filter, in the Z-transform domain, must be used. The Z-domain transfer function of a CR-$(RC)^4$ filter can be expressed by the following equation [84]:

$$H(z) = \frac{z^4\alpha T^3(4 - aT) + z^3\alpha^2T^3(12 - 11aT) + z^2\alpha^3T^3(-12 - 11aT) + z\alpha^4T^3(-4 - aT)}{24(z - \alpha)^5} \qquad 6.21$$

where $a = 1/\tau$, $\alpha = \exp(-T/\tau)$, T is the sampling rate in seconds, and $\tau$ is the time constant. Using this filter, it is possible to perform the semi-Gaussian CR-$(RC)^4$ shaping performed by a shaping amplifier circuit in a digital processing system.

In order to process digital signals produced by the radiation detection system in our laboratory, code was implemented in MATLAB which would perform the necessary steps. First, the CR-$(RC)^4$ filter would be initialized by MATLAB, which would use a given time constant. Next, the detection input signal would be read in by the software, and its vertical scaling would be adjusted so that the signal would start at approximately 0 V, also known as baseline adjustment. Finally, the baseline adjusted signal would be convoluted with the digital filter, yielding an output signal. Appendix C shows the MATLAB code implemented to filter the detection signal. Figure 6.21 shows a signal generated by a test pulser being shaped by the MATLAB software. Figure 6.21a depicts the original signal, whose baseline has already been corrected, and Figure 6.21b shows the signal after being shaped by the CR-$(RC)^4$ filter.

Once a collection of pulse heights have been determined from the stored digital signals, a pulse height histogram can be generated. The histogram will "bin" the pulse heights, and show the number of counts of radiation seen within a range of pulse heights. This process is equivalent to the process an MCA and Genie 2000 undergo when generating pulse height spectrum using an analog system. Figure 6.22 shows an example pulse height distribution generated from detector pulses stored from a CZT detector irradiated using a $^{137}Cs$ source.

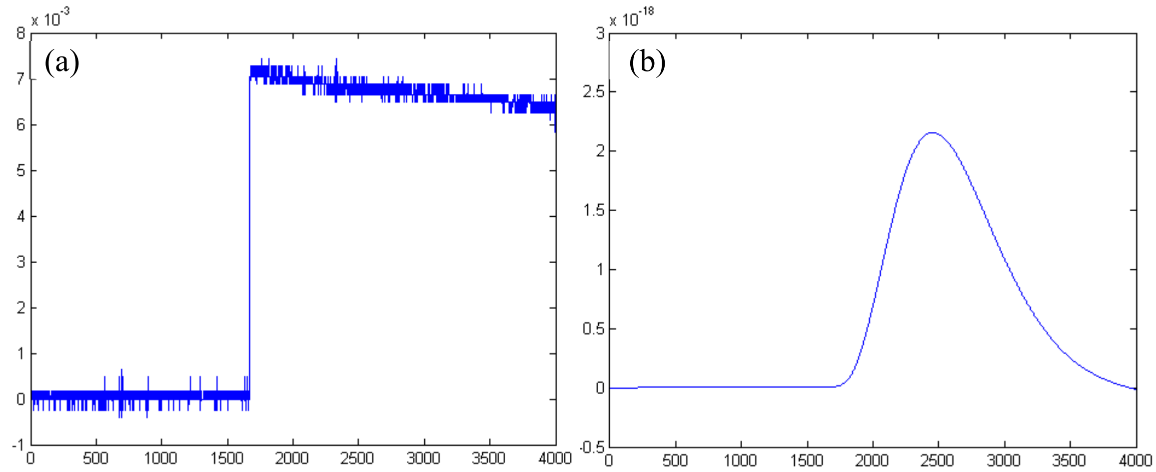


Figure 6.21. (a) Digitized test pulse prior to digital shaping. (b) Test pulse shaped using a CR-(RC)$^4$ digital filter algorithm using MATLAB.

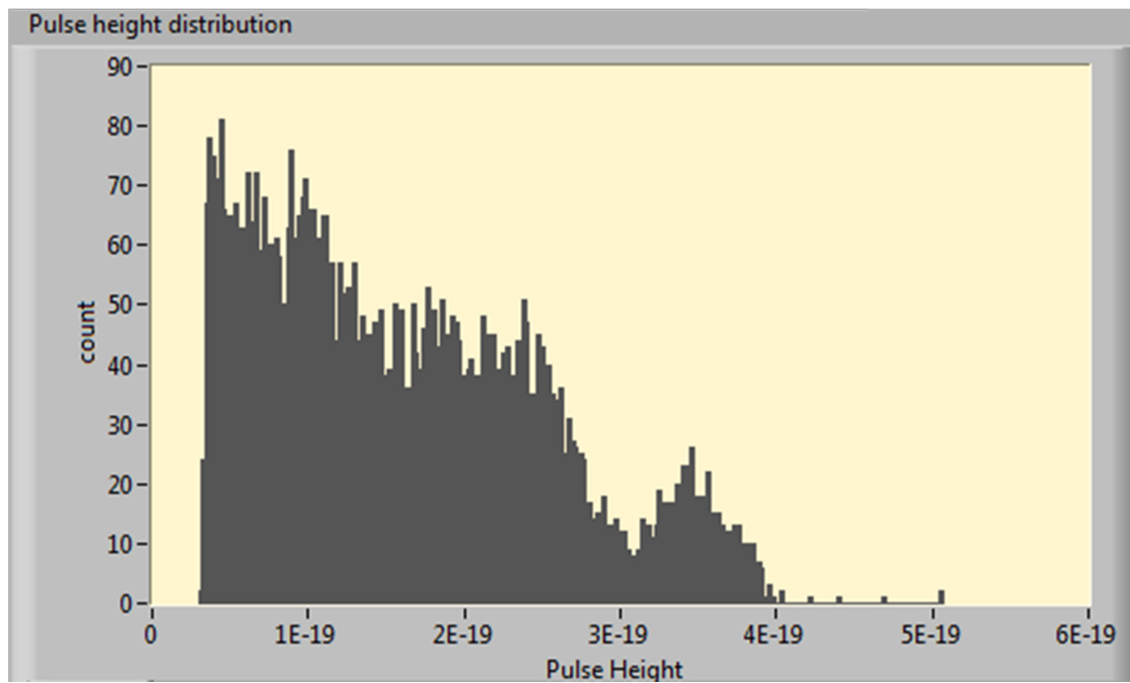


Figure 6.22. Pulse height distribution generated using pulse heights calculated based on digitally stored detector pulses from a CZT detector using a $^{137}Cs$ source.

### 6.4.3 Rise-Time Distribution

In addition to calculating the pulse height digitally, information about the rise-time of a detector pulse can be determined using a digital system. The rise-time of a signal is defined as the time required for a signal output to rise from 10% to 90% of its final value. In the case of radiation detection, it is approximately the time taken for a charge generated due to radiation interaction in the material to travel through the detector material and induce charge on the contact electrodes. Thus, the rise-time gives approximate information about the depth of interaction within a nuclear detector. For high-energy gamma-rays, the depth of interaction can be anywhere along the bulk of the detector material. The longer the charge takes to reach the read-out electrode (typically the anode), the higher its calculated rise-time will be.

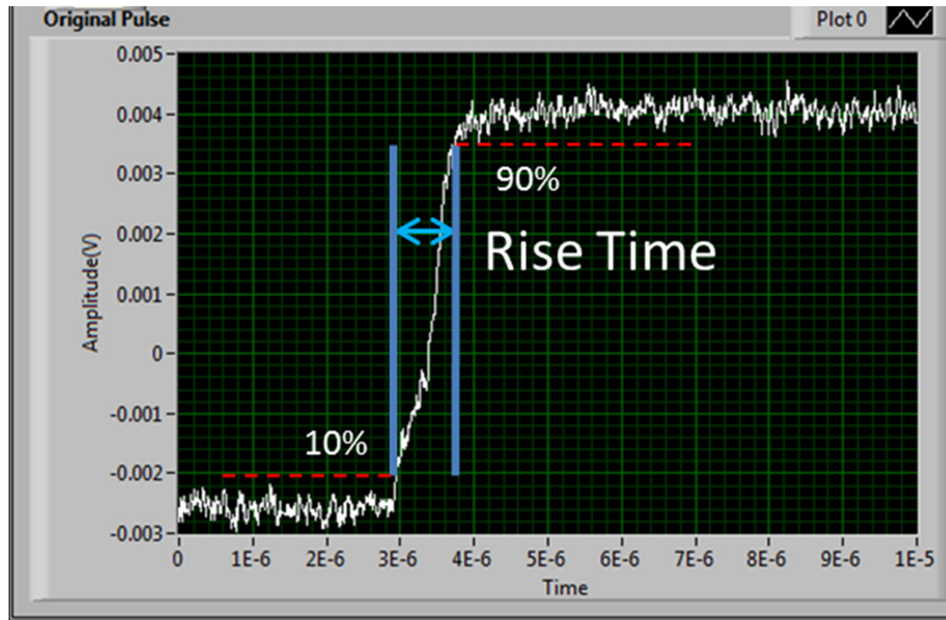


Figure 6.23. Oscilloscope snapshot showing pre-amplifier output of an alpha particle signal detected using CZT.

An example of the rise-time of an alpha particle interaction pulse is shown in Figure 6.23. Once enough pulses have been recorded, a histogram of rise-times can be generated as seen in Figure 6.24. This rise-time distribution is necessary for charge transport measurements, specifically for measuring the mobility of a CZT detector crystal.

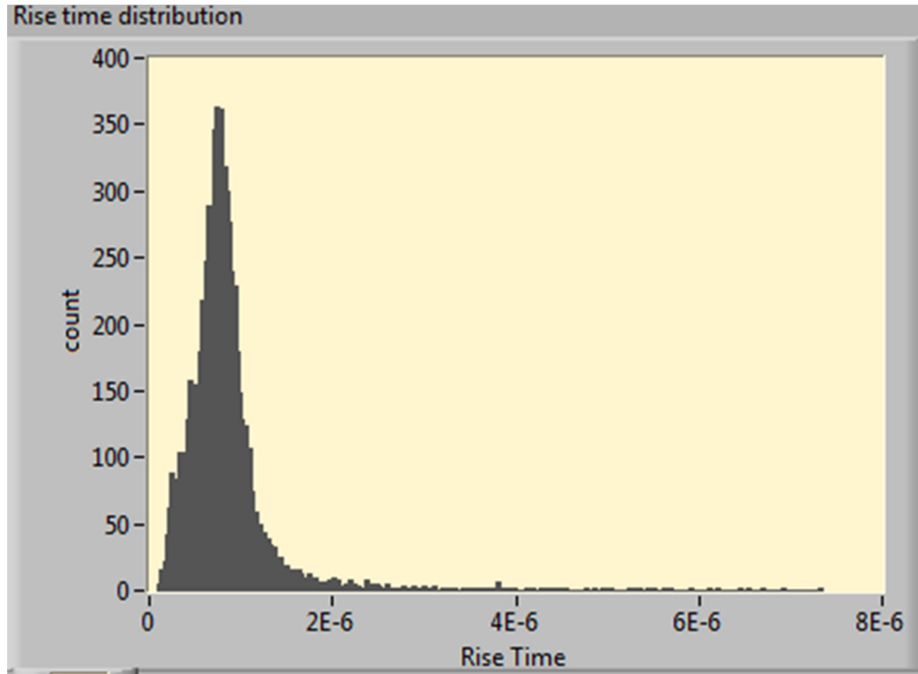


Figure 6.24. Rise-time distribution generated using rise-times calculated based on digitally stored detector pulses from a CZT detector using a $^{137}$Cs source.

## 6.5 Biparametric Plots and Digital Correction Schemes

In addition to pulse height distributions and rise-time distributions, a two dimensional graph combining these sets of data can be used to further analyze a CZT detector's performance. This two dimensional graph is known as a biparametric plot [85, 86]. A biparametric plot provides a visual representation of how the pulse height spectrum of a detector relates to its corresponding rise time distribution. Since the rise-times of

detector pulses correspond to the interaction depth of radiation within a detector, and the pulse heights correspond to the induced charge at the read-out electrode, the biparametric plot can be interpreted as a depiction of the depth of charge versus induced charge. This will reveal what effect the interaction depth of radiation has on the resulting pulse height spectrum, and therefore will give further insight on how a detector is behaving relative to the radiation it is exposed to.

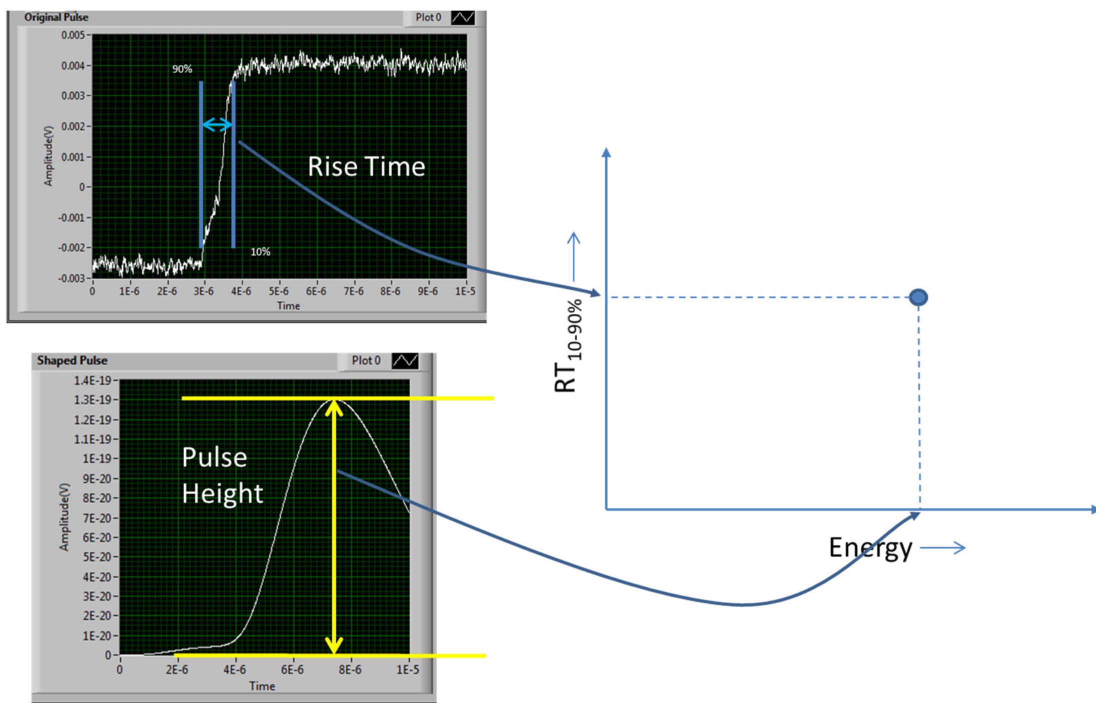


Figure 6.25. Diagram showing how a biparametric plot is generated from rise-times and pulse-heights calculated from nuclear detector pulses.

In order to generate a biparametric plot, both pulse heights and their corresponding rise-times need to be collected for each digitized detector pulse. Histograms of pulse-heights and rise-times are correlated and combined to generate a frequency table. The frequency table stores a two dimensional histogram where for a given range of pulse heights and a given range of rise-times, a number of counts is stored. Based on this two

dimensional array, a contour plot (which is the biparametric plot) can be generated which shows the frequency distribution of the range of rise-times versus the range of pulse heights, for all ranges, as shown in Figure 6.25. MATLAB and LabVIEW-based software was developed in-house to collect the rise-times and pulse heights, as well as create the frequency table and biparametric plot. A biparametric plot for a CZT detector is shown in Figure 6.36. Since the biparametric plot is a 2D histogram depicted using a contour plot, the colormap legend indicates the frequency of counts for a given set of rise-times and pulse heights.

Biparametric plots can also be used to create digital correction schemes which can compensate for the charge losses which affect CZT detectors. Correction of pulse height spectra using biparametric plots has been used in the literature for CZT as an alternative to using special detector fabrication techniques [85]. The digital correction scheme implemented for CZT using MATLAB involves correcting the photopeak interactions based on a correction factor, which is a function of the rise-time and the pulse height. More information about digital correction schemes will be presented in the results section of this chapter.

## 6.6 CHARGE TRANSPORT MEASUREMENTS

### 6.6.1 Background

As seen in Chapter 6.1, the transit time of electrons and holes within the radiation detector material is critical to the accurate operation of the device. In the case of CZT, when holes encounter greater interference in movement than electrons, special considerations have to be taken into account when fabricating the nuclear detector. Similarly, if there are any issues with electron movement within the CZT crystal, nuclear

detection properties can be drastically affected. Charge transport properties, such as drift mobility (μ) and carrier lifetime mobility product (μτ), are measured to determine a crystal's effectiveness as a nuclear detector. Both of the parameters are measured using a radiation detection system, with a nuclear source applying radiation to the CZT crystal. Since hole charge transport properties are far worse than electron transport properties, and detectors are fabricated to eliminate the poor hole charge transport propreties, most focus is given to electron mobility ($\mu_e$) and electron mobility-lifetime product ($\mu\tau_e$) measurements.

### 6.6.2 Mobility

Drift mobility (μ) of a charge carrier is defined as the velocity acquired by a charge carrier per unit applied electric field, and is given by the following equation:

$$v_d = \mu_e E \quad 6.22$$

where $v_d$ is the electron drift velocity for the case of electrons and $E$ is the electric field applied to the device. Typical electron mobility values for CZT are ~1100 $cm^2/Vs$ [9]. It is possible to measure the drift velocity of the electrons for a nuclear detector, under a known electric field bias, if the electrons are travelling from one end of the detector material to the other. This method of measuring the mobility is called a time-of-flight measurement [87]. A detector material is irradiated with alpha particle radiation using an $^{241}Am$ alpha source on the cathode of the detector, as seen in Figure 6.26. The cathode will have a negative applied voltage bias, while the anode will be grounded, and will collect the resulting generated signals. The alpha particles will strike the cathode, which will cause electron-hole pairs to be generated just below the cathode, as alpha particles have very less penetration depth in CZT. Since electron-hole pairs are generated immediately at the

cathode, the electrons will have to travel the entire distance of the detector to reach the anode. Furthermore, the movement of holes in the resulting signal will be negligible due to their close proximity to the negatively biased cathode, where they will be collected.

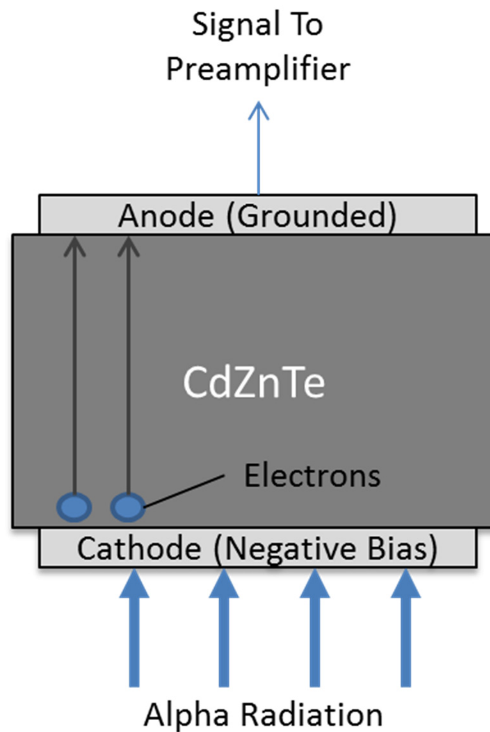


Figure 6.26. Schematic of mobility ($\mu_e$) and the mobility-lifetime product ($\mu\tau_e$) measurements for electrons in a CZT radiation detector.

An example of the resulting detector signals generated by the electrons can be seen in Figure 6.23. Several thousand rise-times are calculated from their respective stored pulses, and a histogram is generated, as seen in Figure 6.27. The centroid of the histogram is calculated assuming a Gaussian distribution to determine the mean rise time.

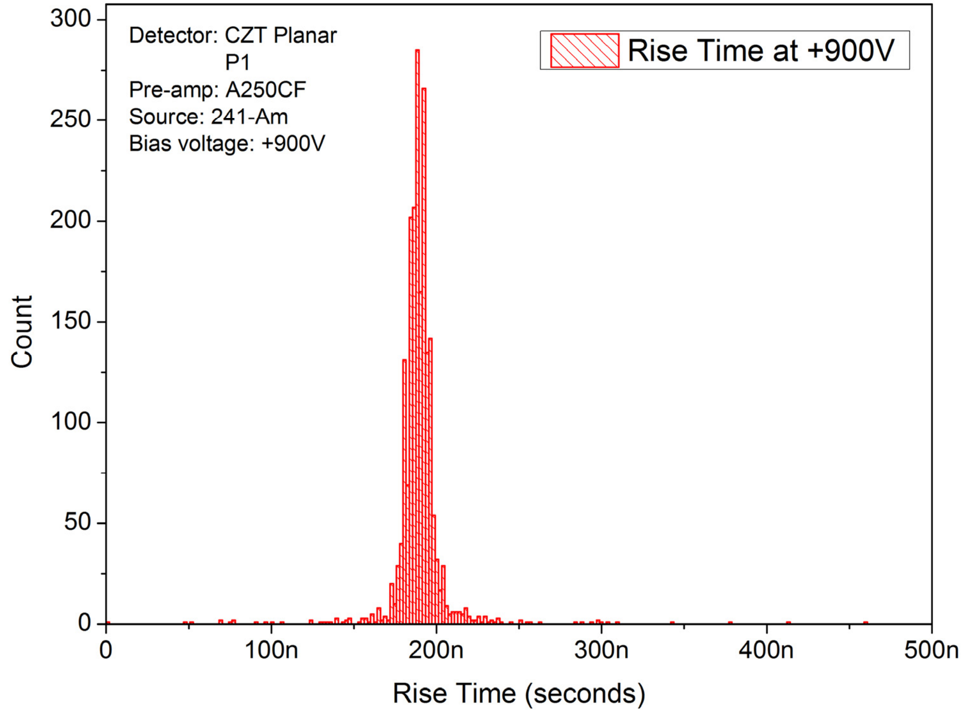


Figure 6.27. Histogram of rise times generated from the planar CZT detector PL1 biased at 900V.

Several rise times are calculated for different bias voltages, and the drift velocity is calculated for each rise time using the relationship $v_d = \frac{L}{t}$, where L is the detector thickness in cm, and t is the rise time in seconds. The electric field for each rise time is also calculated using the relationship $E = \frac{V}{L}$, where V is the bias voltage and L is the detector thickness. The drift velocities versus electric field are plotted, and a linear fit is performed on the resulting data, as shown in Figure 6.28. This process was performed on the CZT planar detector P1, shown in Figure 6.2. After determining the slope of the fitted data, the electron mobility of planar detector P1 was calculated to be 1208 $cm^2/Vs$.

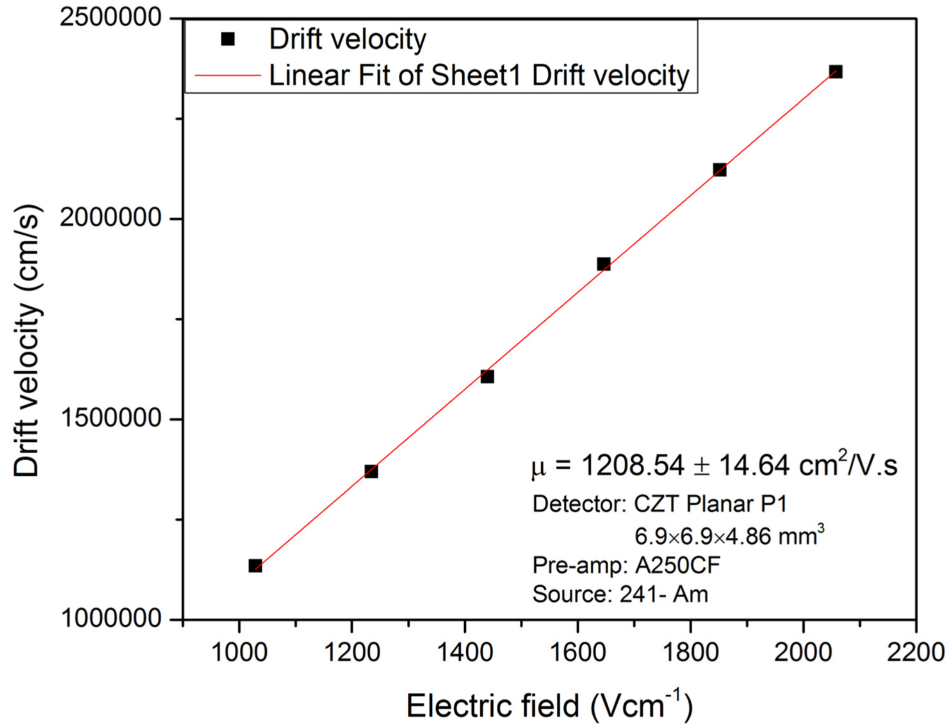


Figure 6.28. Drift velocity vs. Electric field plot for the planar CZT detector PL1. The slope of the linear fit of the data gives the mobility of the CZT detector crystal.

### 6.6.3 Mobility-Lifetime Product

The mobility-lifetime product ($\mu\tau$) is another charge transport property commonly measured to determine the effectiveness of a CZT crystal used as a nuclear detector. It is the product of the carrier mobility ($\mu$), and the carrier lifetime ($\tau$). The carrier lifetime in a material is defined as the average time charge carriers spend between generation and recombination in that material [77]. If a charge carrier is trapped, even if carrier is released from the trap eventually, the resulting detection signal will reflect this inefficiency of charge collection. The charge collection efficiency (CCE) of a nuclear detector can be related to the $\mu\tau$ product using the Hecht equation [88], given by:

$$CCE = \frac{Q_s}{Q_o} = \frac{\mu\tau_e V}{d^2}\left[1 - exp\left(\frac{-d^2}{\mu\tau_e V}\right)\right] + \frac{\mu\tau_h V}{d^2}\left[1 - exp\left(\frac{-d^2}{\mu\tau_h V}\right)\right] \quad 6.23$$

where $Q_s$ is the total charge detected, $Q_o$ is the expected total charge, $\mu\tau_e$ and $\mu\tau_h$ are the electron and hole mobility lifetime products, respectively, V is the bias voltage, and d is the detector thickness. The Hecht equation is a function of both $\mu\tau_e$ and $\mu\tau_h$, and so the charge collection efficiency accounts for both hole and electron movement. When measuring the μτ product, only the μτ for electrons or holes can be measured at a time. Therefore, for measurement purposes, the following single carrier version of the Hecht equation is applied instead:

$$CCE = \frac{\mu\tau V}{d^2}\left[1 - exp\left(\frac{-d^2}{\mu\tau V}\right)\right] \quad 6.24$$

For CZT, the electron mobility-lifetime product is a common measurement used to characterize the charge transport properties of a detector, since it highlights both the electron trapping tendency and electron mobility, both of which are important to radiation detection. Lower $\mu\tau_e$ values result in lower energy counts in the resulting detection spectrum which actually belong to higher energy gamma-rays, resulting in a tail present in the photopeak [89].

The electron mobility-lifetime product is measured by irradiating a CZT detector with alpha particles at the cathode, in the same configuration shown in Figure 6.26 for mobility measurements. The detection signal is then sent through the analog detection system shown in Figure 6.9. Analog spectrum is recorded using the PC software at varying bias voltages, and the energy of the $^{241}$Am alpha particles is recorded. Figure 6.29 shows the analog spectrum collected at various bias voltages. As seen in the Hecht equation,

charge collection efficiency is dependent on the bias voltage as well. The peak positions shift to higher energies as higher bias voltage is applied, due to more efficient charge collection. Charges are more quickly separated and swept to the collecting electrodes under higher voltage bias applied to the detector.

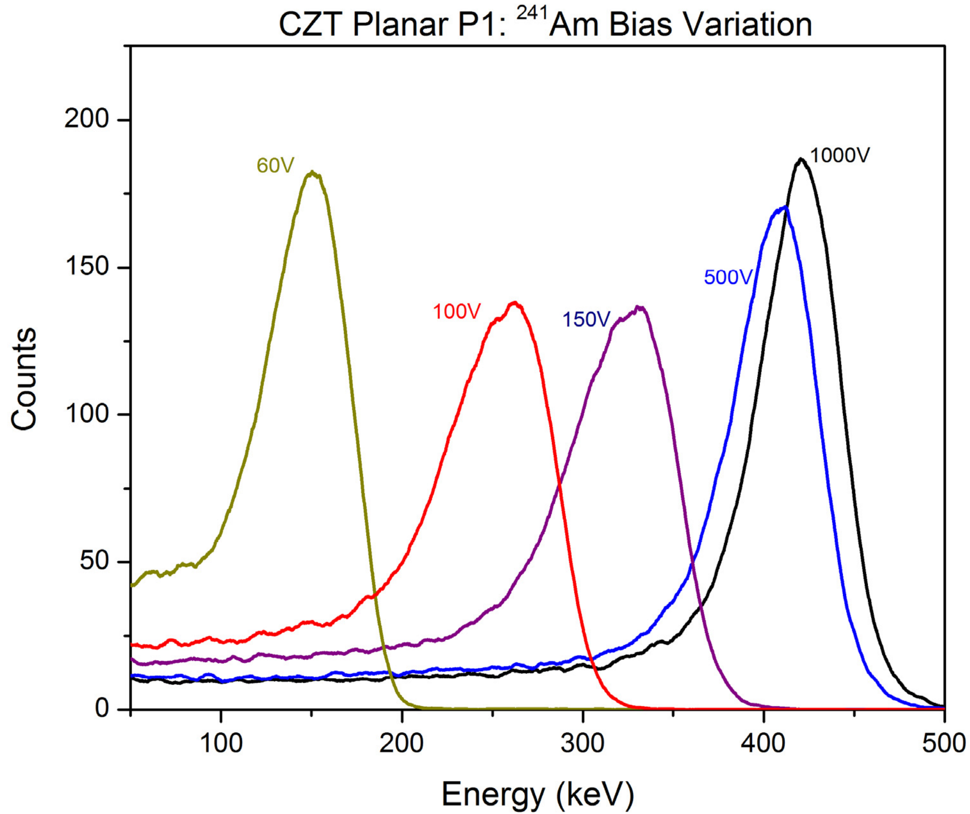


Figure 6.29. Alpha particle spectra at varying voltage bias for CZT planar detector P1 irradiated with $^{241}$Am.

After collecting the energy of the photopeaks versus bias voltage, the charge collection efficiency at each bias voltage is calculated by dividing the actual energy by the incident energy for $^{241}$Am alpha particles (5.486 MeV). The charge collection efficiencies versus bias voltage values are plotted, and the resulting values are fit using the single carrier Hecht equation, as shown in Figure 6.30. After the curve fitting, the $\mu\tau_e$ of the planar CZT

detector PL1 is determined to be $2.72 \times 10^{-3}$ $cm^2/V$. This value is in the typical range of $\mu\tau_e$ values reported for detector grade CZT crystals [9].

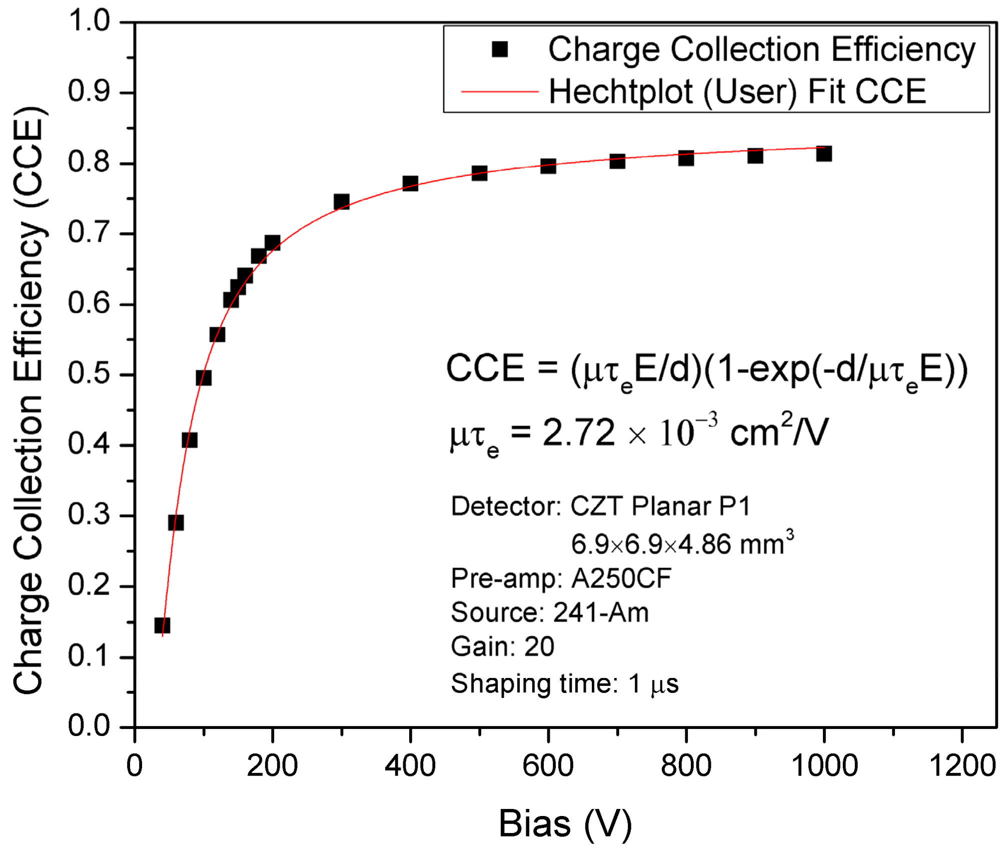


Figure 6.30. Charge collection efficiency vs. bias voltage plot for the planar CZT detector PL1. Fitting the data with the Hecht equation gives the $\mu\tau_e$ of the CZT crystal.

## 6.7 DETECTOR CHARACTERIZATION RESULTS

### 6.7.1 Planar Detector vs. Frisch Collar Detector

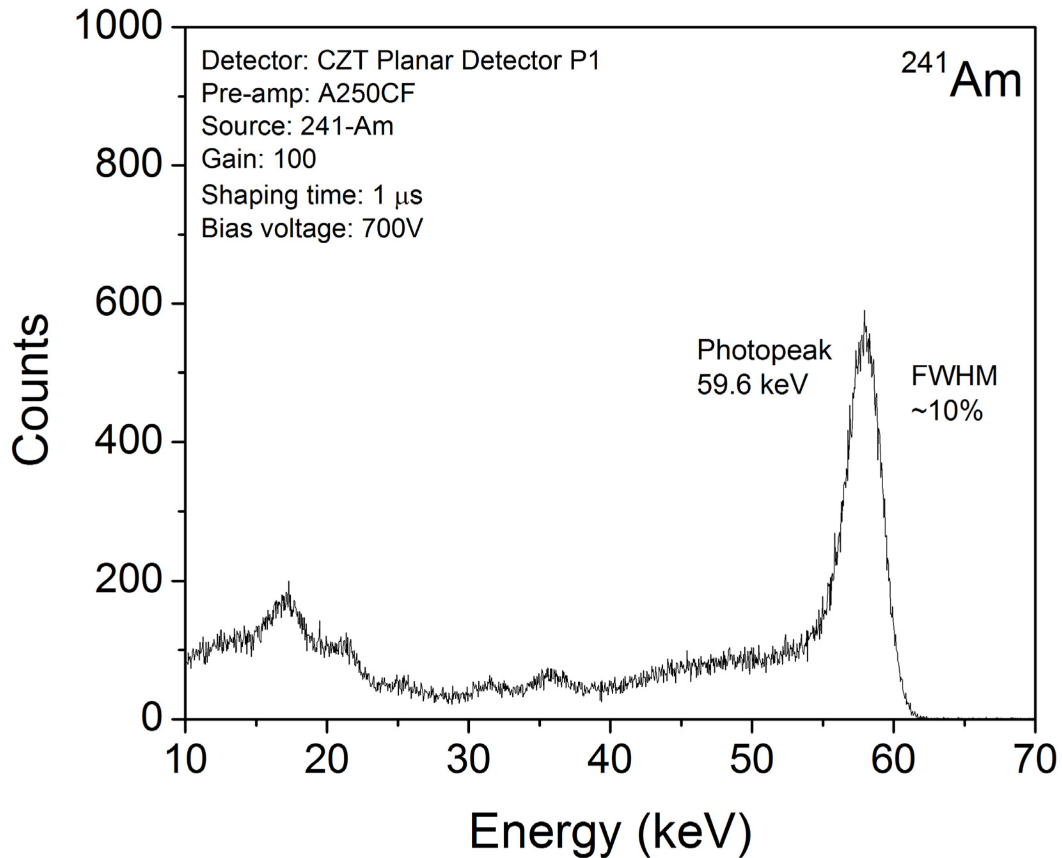


Figure 6.31. $^{241}$Am pulse height spectrum obtained from CZT detector P1 biased at 700V.

The planar detector P1 was first tested using the $^{241}$Am source to test its response to low-energy gamma-rays. Figure 6.31 shows the resulting pulse height spectrum with $^{241}$Am for detector P1. After performing Gaussian peak fitting, the FWHM of the gamma photopeak at ~59keV was calculated to be ~10%. Since the weighting potential of a planar detector is dependent upon interaction depth, a CZT planar detector will be inefficient at detecting gamma-rays since interactions would occur at any depth within the detector, and therefore poor hole transport properties would smear the photopeak. Although this detector is in a planar configuration, low-energy gamma-rays penetrate less deeply into the detector

bulk than high-energy gamma-rays. The gamma-rays emitted by the $^{241}$Am source interact with the detector near the cathode of the detector, and therefore most of the detection signal produced will be due to the movement of electrons through the detector. Since electron charge transport properties within CZT are better than hole charge transport properties, a photopeak is observed for the low-energy gamma-rays at 59.6 keV.

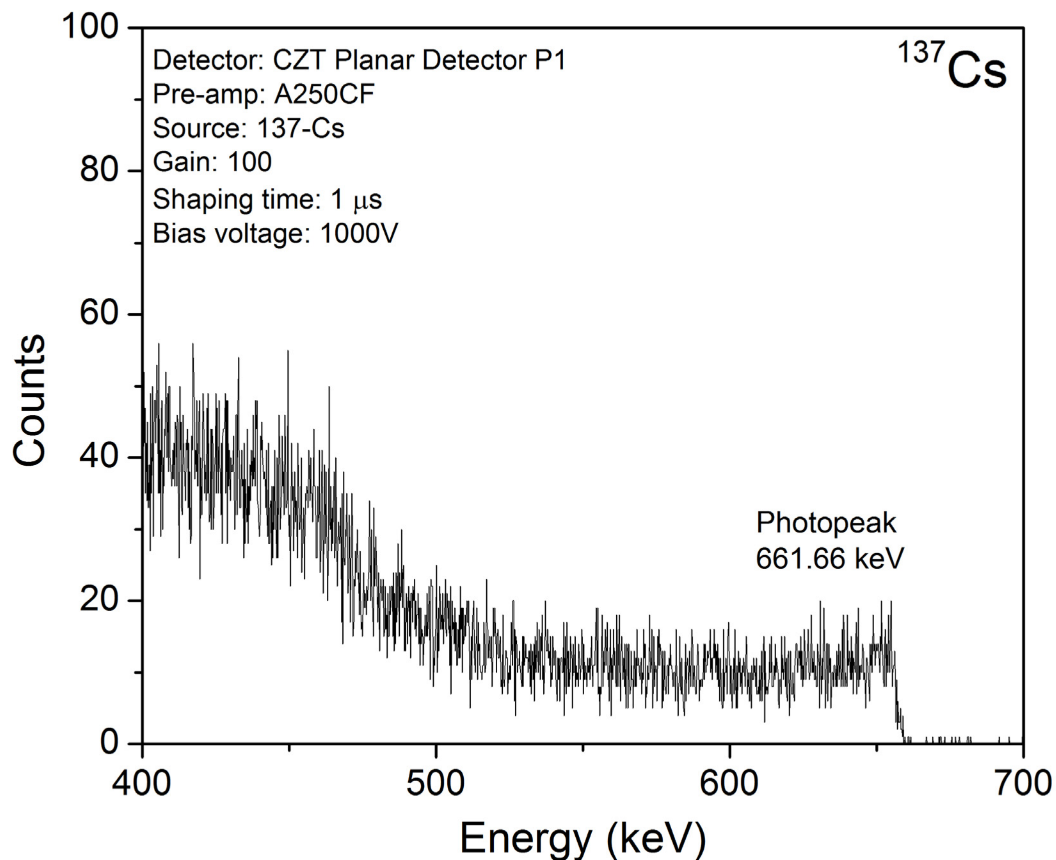


Figure 6.32. $^{137}$Cs pulse height spectrum obtained from CZT detector P1 biased at 1000V.

The planar detector P1 was then tested using the $^{137}$Cs source to test its response to high-energy gamma-rays, as seen in the pulse height spectrum shown in Figure 6.32. Since high-energy gamma-rays penetrate deeper into the bulk of the crystal than the low-energy gamma-rays, the effects of poor hole transport properties are more apparent. Instead of a

clear peak at 662 keV, the photopeak is smeared towards the lower energy side. This smearing occurs with all CZT detectors in the typical planar configuration, which necessitates the special detector geometries discussed previously.

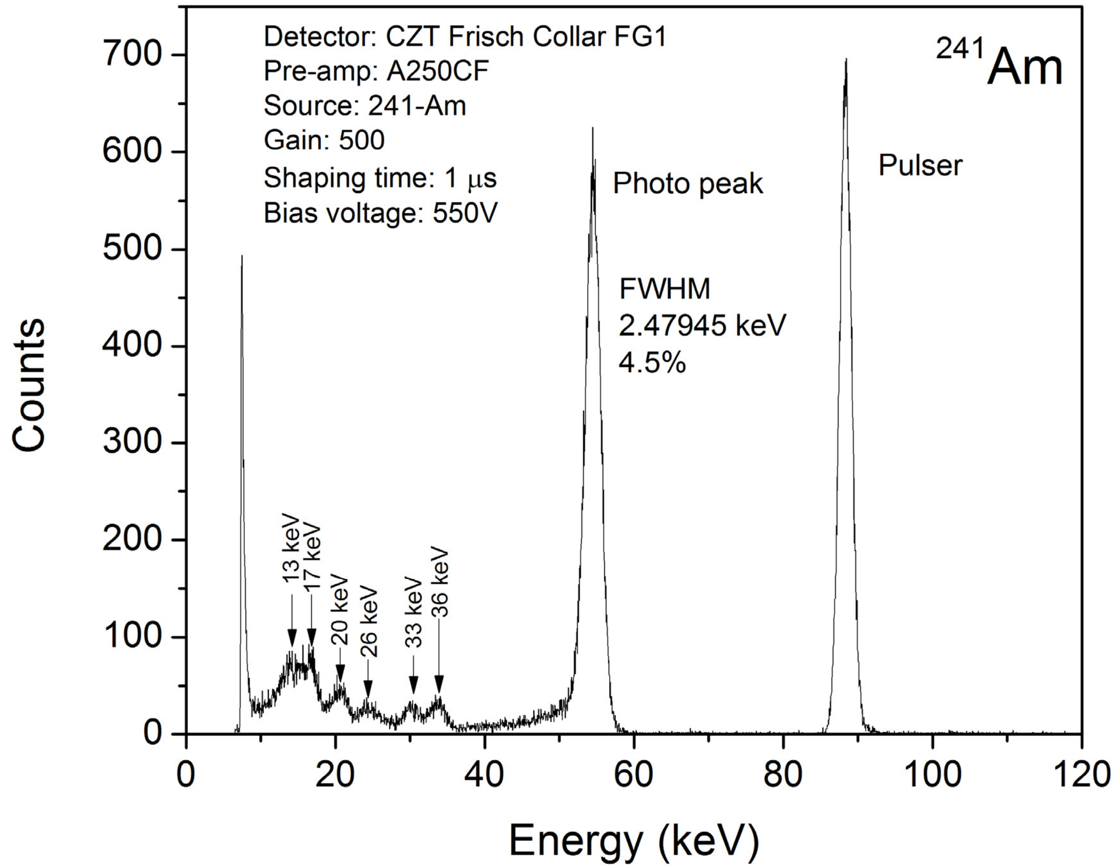


Figure 6.33. $^{241}$Am pulse height spectrum obtained from CZT detector FG1 biased at 550V.

The first Frisch collar detector FG1 was tested using the $^{241}$Am nuclear source, whose results are shown in Figure 6.33. Just like the planar detector P1, a photopeak is observed for the low-energy 59.6 keV gamma-rays. The energy resolution was calculated to be 4.5% (2.47 keV @ 59.6 keV) after Gaussian peak fitting.

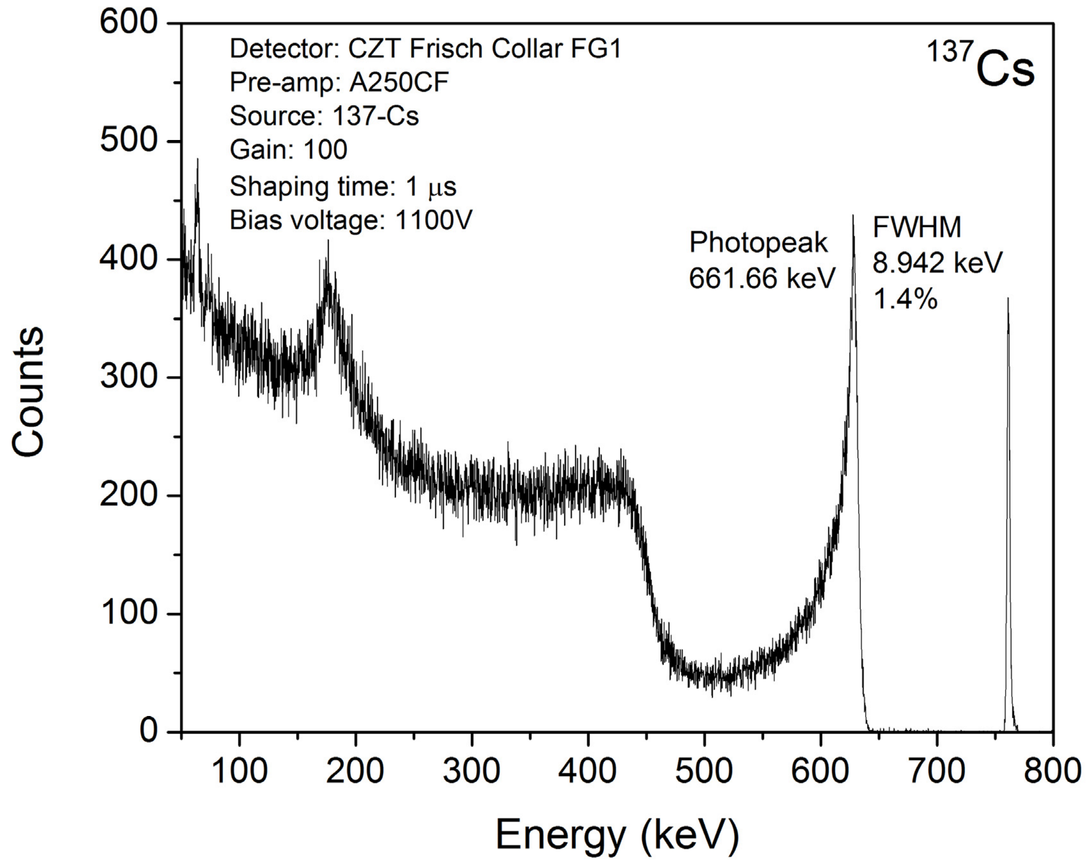


Figure 6.34. $^{137}$Cs pulse height spectrum obtained from CZT detector FG1 biased at 1100V.

FG1 was then tested using $^{137}$Cs nuclear source, whose results are shown in Figure 6.34. The full photopeak corresponding to the 662 keV gamma rays was clearly resolved by the virtual Frisch grid detector. After peak fitting, the energy resolution was calculated to be 1.4% (8.94 keV @ 662 keV). When compared to the planar CZT detector's $^{137}$Cs response, shown in Figure 6.35, the virtual Frisch grid is able to observe the 662 keV photopeak, whereas the planar detector is unable to because of the effects of poor hole transport properties in CZT.

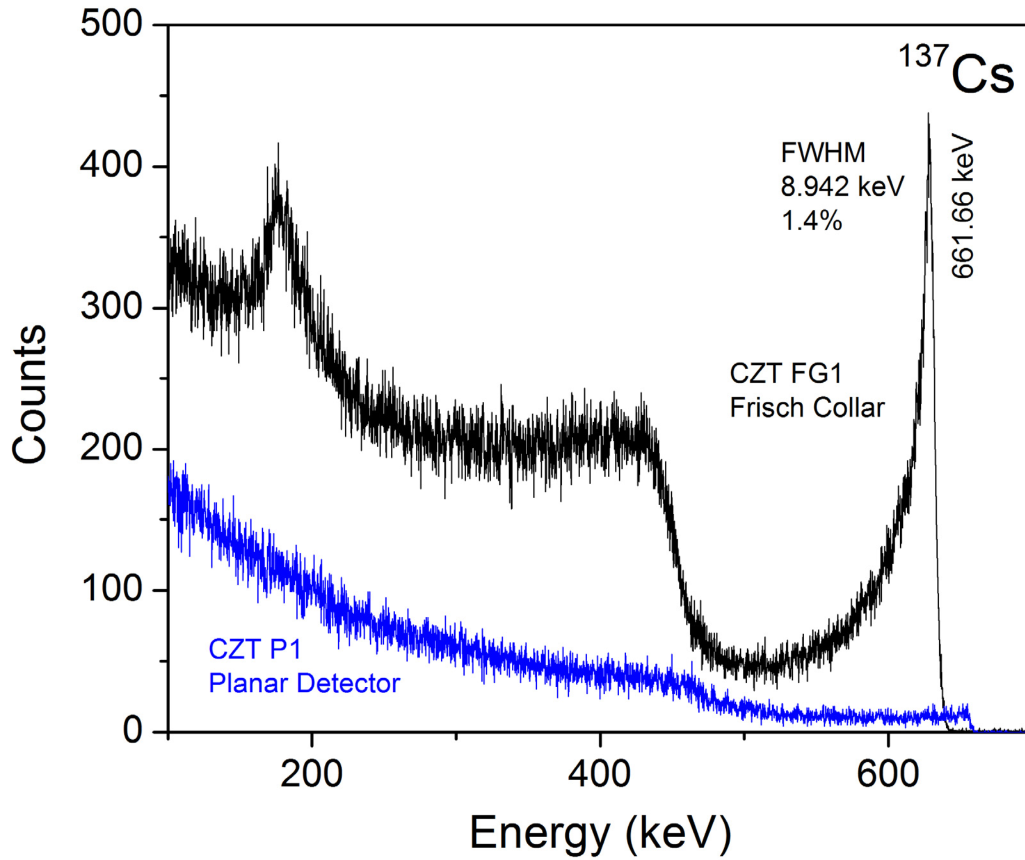

Figure 6.35. Comparison of $^{137}$Cs spectrum taken from detectors P1 and FG1.

### 6.7.2 Digital Spectroscopy Results using Planar Detector

For further insight into the performance of the planar detector P1's $^{137}$Cs pulse height spectrum, digital spectroscopy was used. Figure 6.36 shows a biparametric plot generated for detector P1, comparing the pulse heights versus their respective rise-times.

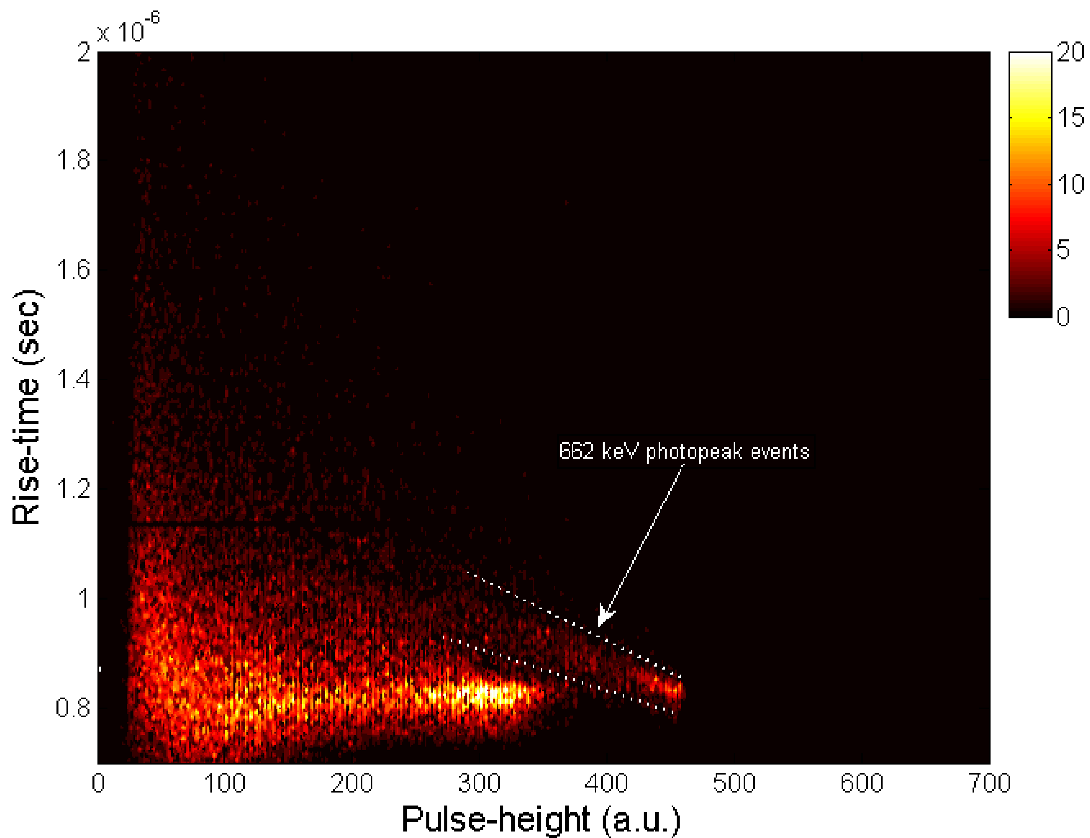


Figure 6.36. Biparametric plot of CZT detector P1 biased at 1000V, irradiated using $^{137}$Cs source. Brighter regions indicate higher frequency of counts.

In order to compare this biparametric plot with expected detector behavior, Figure 6.37 shows a biparametric plot of detector FG1, which produced an excellent photopeak in the pulse height spectrum for $^{137}$Cs, as shown in Figure 6.34. In the FG1 biparametric plot, the 662 keV events occur at a nearly singular pulse height region with varying rise-times from about 0.85 to 0.95 μs.

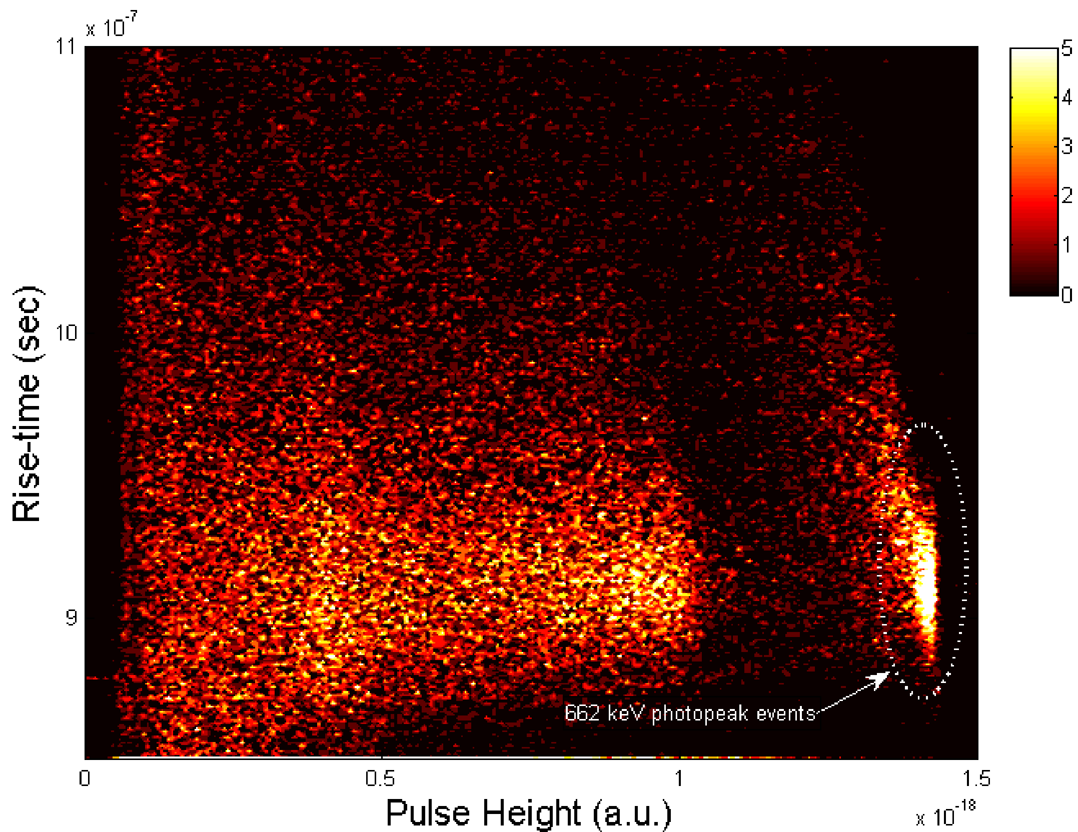


Figure 6.37. Biparametric plot of CZT detector FG1 biased at 1200V, irradiated using $^{137}Cs$ source.

In a biparametric plot, rise-times correspond to the interaction depth of radiation within a detector, and pulse heights correspond to induced charge of the radiation at the detector electrodes. In an ideal planar detector with no defects, or a single polarity charge sensing detector, the interaction depth of the radiation would not affect the induced charge seen at the detector electrodes. For the 662 keV events seen for FG1 in Figure 6.37, induced charge at the electrodes (pulse height) does not change depending on where in the detector the interaction of radiation has occurred (varying rise-times). Since FG1 uses the virtual Frisch grid detector configuration, charge resulting from radiation interactions will only affect the pulse height distribution in the near-grid region of the virtual Frisch grid detector.

The biparametric plot for planar detector P1 in Figure 6.36 shows the 662 keV photopeak to be slanted, with pulse heights decreasing with increasing rise-times. This corresponds to the smeared 662 keV photopeak seen in the pulse height spectrum shown in Figure 6.32. For a planar CZT detector, the induced charge seen at the read-out electrode (in this case, the anode) is dependent upon the interaction location within the detector. Since the high-energy gamma-rays have interacted at any location through the thickness of the detector, the pulse height energy of the photopeak appears reduced, and is directly correlated to the amount of time the charge takes to travel through the detector. This can be more clearly visualized in Figure 6.38, which shows the pulse height spectrum at four different depth intervals (or rise-time intervals) of the detector. These spectra were regenerated from the biparametric plot shown in Figure 6.36 by plotting pulse height spectra from events lying in four different rise-time intervals. The spectrum obtained from the highest rise-time events are considered to be closest to the anode (interval 4) and similarly interval 1 shows the pulse height spectrum from the events close to the cathode. Interval 4 shows very few spectral features as the hole movement contributes significantly to the signal from these events. However, the spectrum obtained from the events close to the cathode show a sharp peak for the 662 keV events, since the signals were formed mostly due to electron movement within the detector.

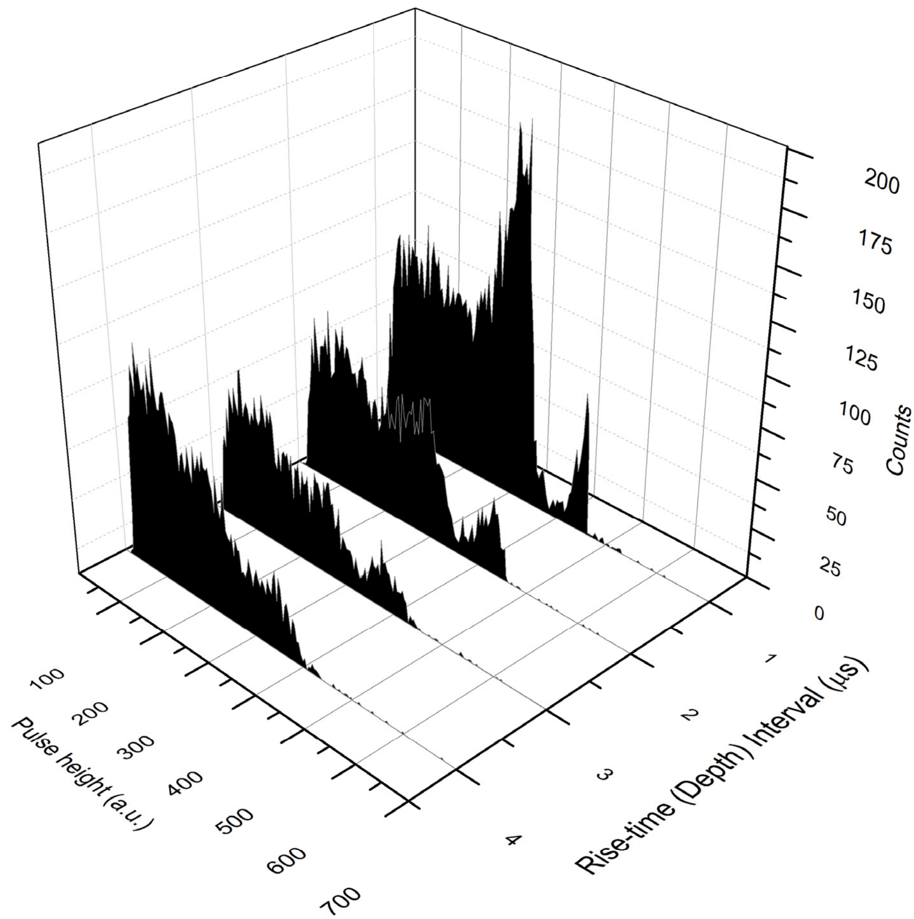


Figure 6.38. $^{137}$Cs pulse-height spectra generated from the biparametric plot for events from four different depth-intervals in CZT detector P1. Interval 1 shows spectrum from events close to the anode, while interval 4 shows spectrum from events close to the cathode.

Using a digital correction scheme, the biparametric plot can be used to correct the effects of poor hole transport properties and recover the $^{137}$Cs spectrum for planar detector P1. In order to recover the pulse-height spectrum from the effect of the hole-trapping, the relevant data points in the biparametric plot were displaced by adding numerical factors depending on the rise-time of the particular event. Figure 6.39 shows the biparametric plot before and after application of the correction scheme.

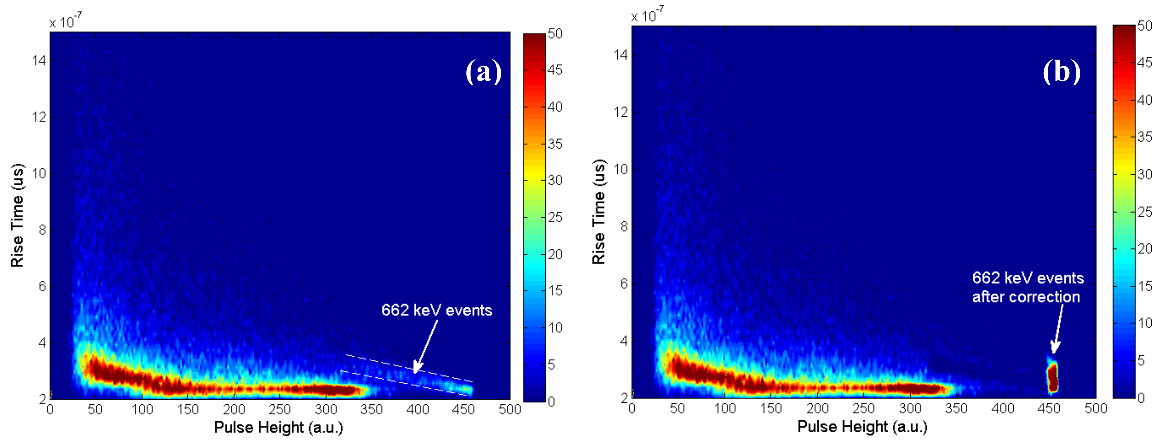


Figure 6.39. Biparametric plot obtained from interaction of 662 keV gamma rays with the planar detector P1 (a) uncorrected (b) corrected.

The corrected pulse-height spectrum regenerated from the corrected biparametric plot is shown in Figure 6.40. Spectral features like the photopeak and the Compton edge, which were missing in the $^{137}$Cs analog pulse-height spectrum shown in Figure 6.32, are clearly visible in the digitally corrected spectrum. A distinct 662 keV peak can now be seen in the corrected plot. A percentage energy resolution of 1.6 % for 662 keV gamma rays was calculated from the corrected spectrum.

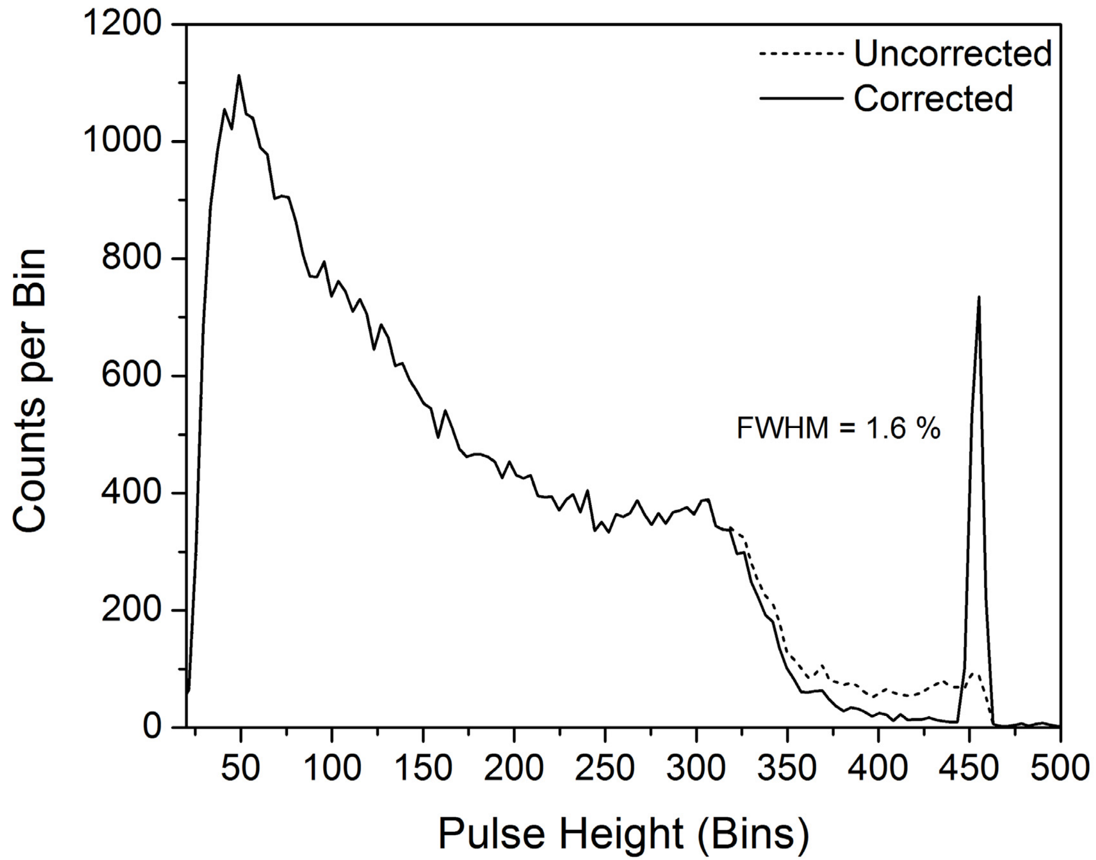


Figure 6.40. Corrected pulse height spectrum generated from the digital corrections applied to the biparametric plot of detector P1 shown in Figure 6.39.

### 6.7.3 Comparison of Frisch Collar Detectors

While the Frisch Collar detector structure is very successful at eliminating the effects of poor hole transport in CZT detectors, issues with the measurement region in a detector cannot be remedied by this method. Two Frisch collar detectors were fabricated in the laboratory; FG1 and FG2 (see Figure 6.8). Figure 6.34 shows the analog pulse height spectrum obtained for FG1 irradiated using high-energy gamma rays ($^{137}Cs$), while Figure 6.41 shows the analog pulse height spectrum for FG2 under high-energy gamma-ray irradiation.

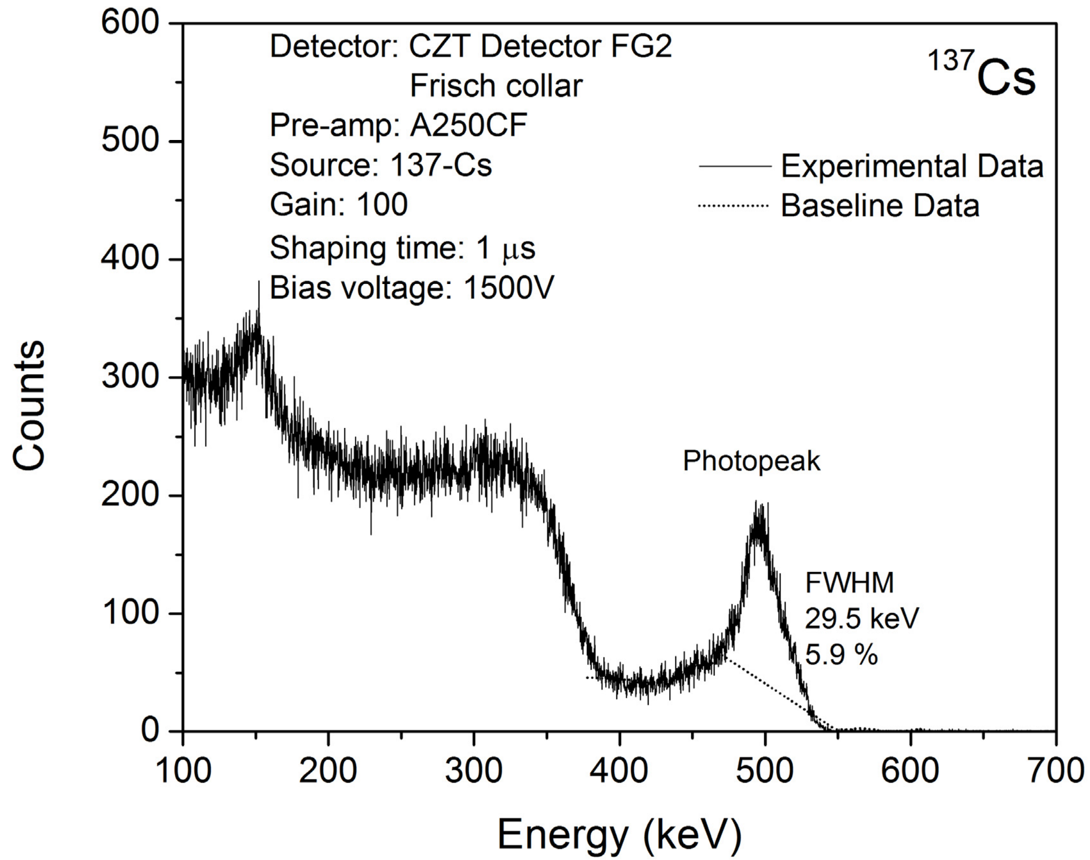


Figure 6.41. $^{137}$Cs pulse height spectrum obtained from CZT detector FG2 biased at 1200V.

The $^{137}$Cs photopeak for detector FG2 has a calculated energy resolution of 5.9% after peak-fitting. Furthermore, the photopeak for FG2 lies at ~500 keV, which is much lower than the expected 662 keV energy for $^{137}$Cs, which indicates a lower charge collection efficiency at similar bias voltages to FG1. To further understand the lower energy resolution and lower charge collection efficiency of this detector, a rise-time distribution of detectors FG1 and FG2 was constructed, as well as a biparametric plot of detector FG2.

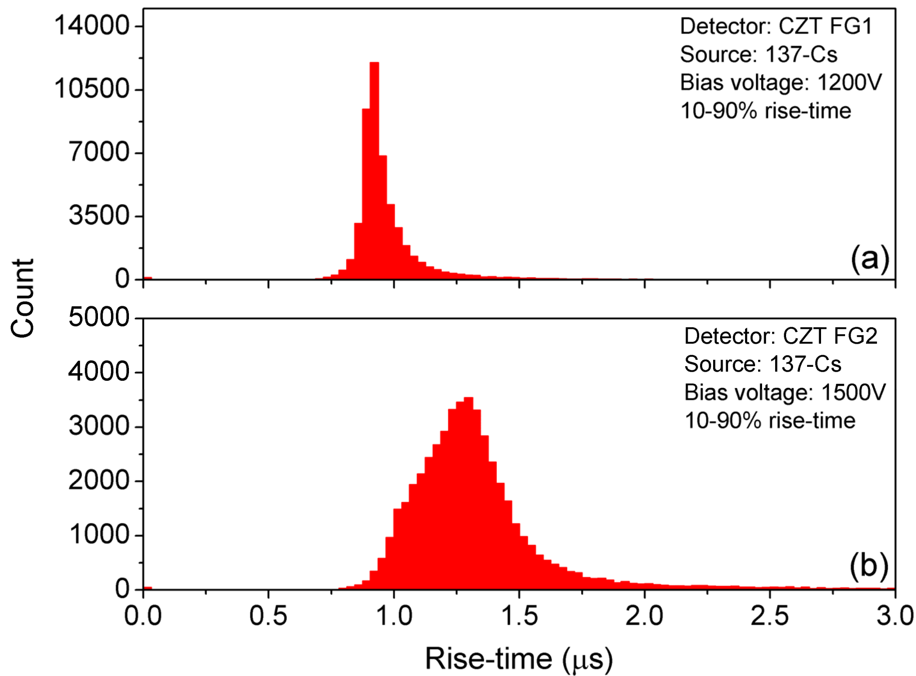


Figure 6.42. Rise-time distribution calculated from detection pulses from $^{137}Cs$ for CZT detectors (a) FG1 and (b) FG2.

The rise-time distributions for both FG1 and FG2 can be seen in Figure 6.42. For a Frisch collar detector, the rise-time of the detector pulses gives the transit-time of electrons within the measurement region. The average rise-time of pulses obtained from detector FG1 is less than detector FG2, which suggests that the weighting potential distribution near the anode is steeper in the measurement region in FG1 compared to FG2, which results in a more rapid transit of the electrons in this region. Also a broader distribution of the rise-times for FG2 reflects the combined effect of trapping and incomplete charge collection on the detector output signal.

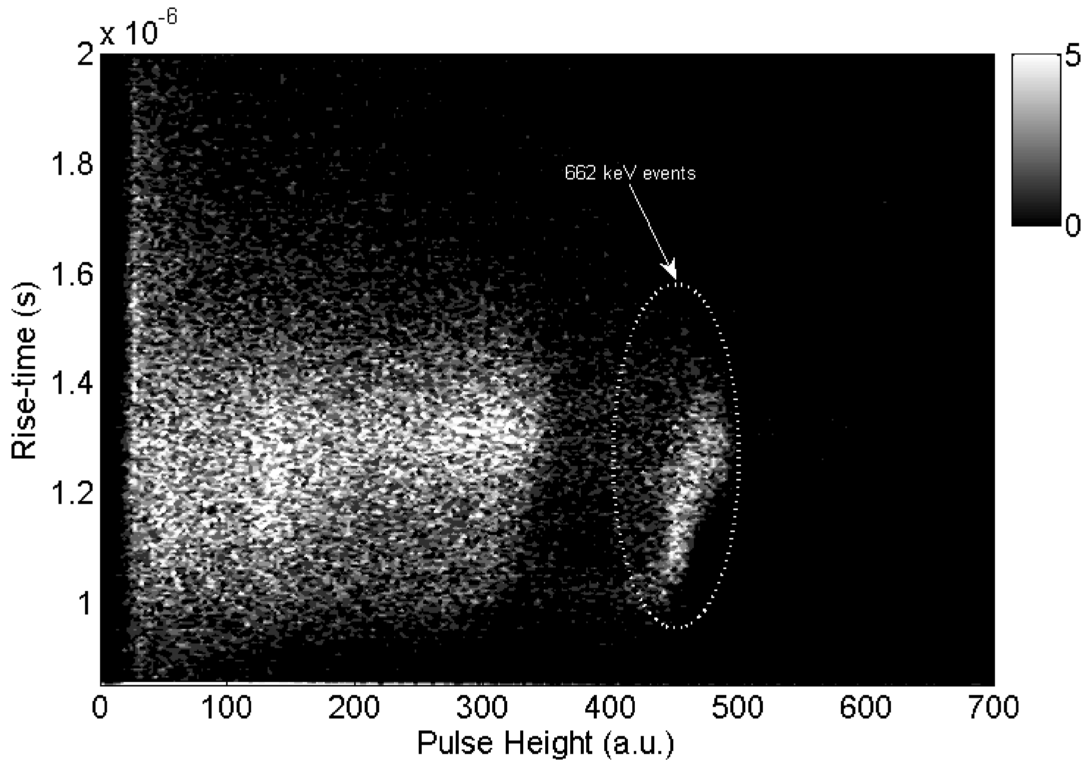


Figure 6.43. Biparametric plot of CZT detector FG2 biased at 1500V, irradiated using $^{137}$Cs source.

A biparametric plot showing the $^{137}$Cs events for detector FG2 can be seen in Figure 6.43. For the events due to the 662 keV interactions, an incline in the photopeak can be seen with respect to the rise-times. This incline is likely due to electron trapping centers present within the measurement region of the Frisch collar detector. Electrons which are trapped due to defects in the measurement region will experience smaller pulse heights due to partial charge collection. This effect would also cause the broader rise-time distribution seen for FG2 as compared to FG1. As electrons eventually become de-trapped more charge is collected at the anode. In the case of electrons that are not trapped at all, full charge collection is present, as is the case at rise-times of 1.2 to 1.4 μs.

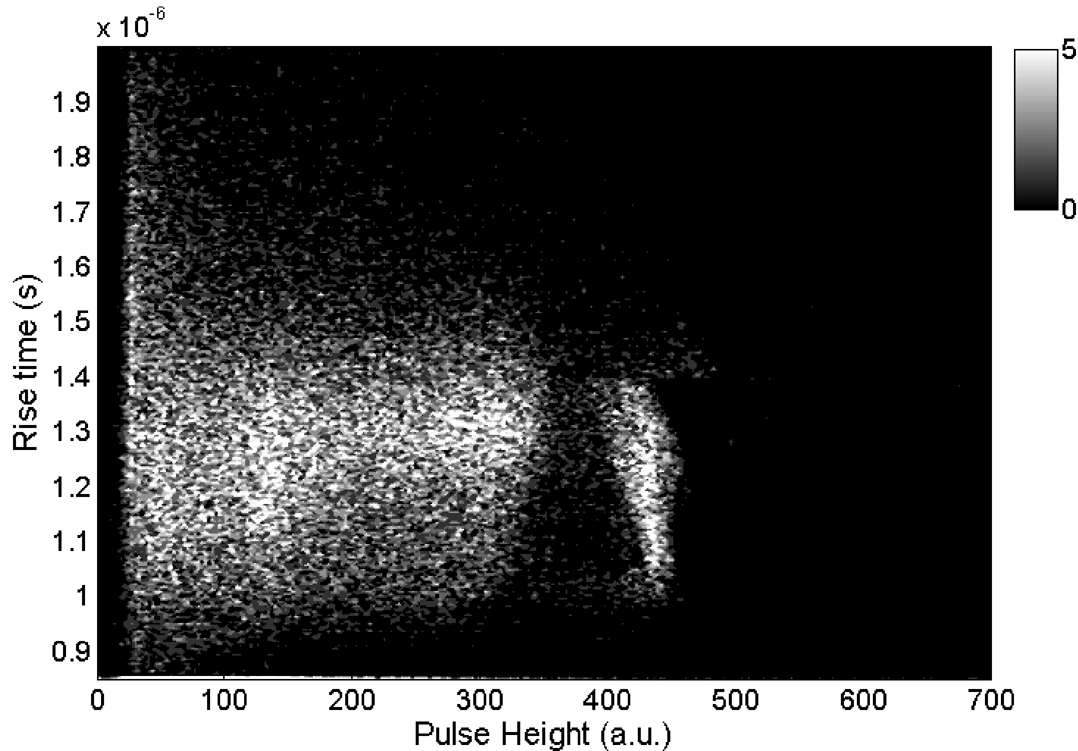


Figure 6.44. Biparametric plot obtained from detector FG2 after applied digital corrections.

The effects of electron trapping can be compensated for by using digital corrections on the biparametric plot for detector FG2, just as was performed for detector P1. Figure 6.44 shows the biparametric plot of detector FG2 after digital corrections were applied to the digitized pulse heights. The pulse height distribution of the digital pulses seen in the biparametric plot can be seen in Figure 6.45. In our digital detection system, before corrections FG2 has an energy resolution of 8.1% at 662 keV events, while after corrections a resolution of 6.5% is obtained. While the effects of electron trapping cannot be fully compensated for by using the same correction scheme used for detector P1, an improvement in the detector's energy resolution is apparent. Furthermore, it is noted that the FWHM of the uncorrected spectrum for the digital system is much higher than for the

analog system. This suggests that the digital system has unknown sources of noise present which are contributing to the resulting digitized spectrum.

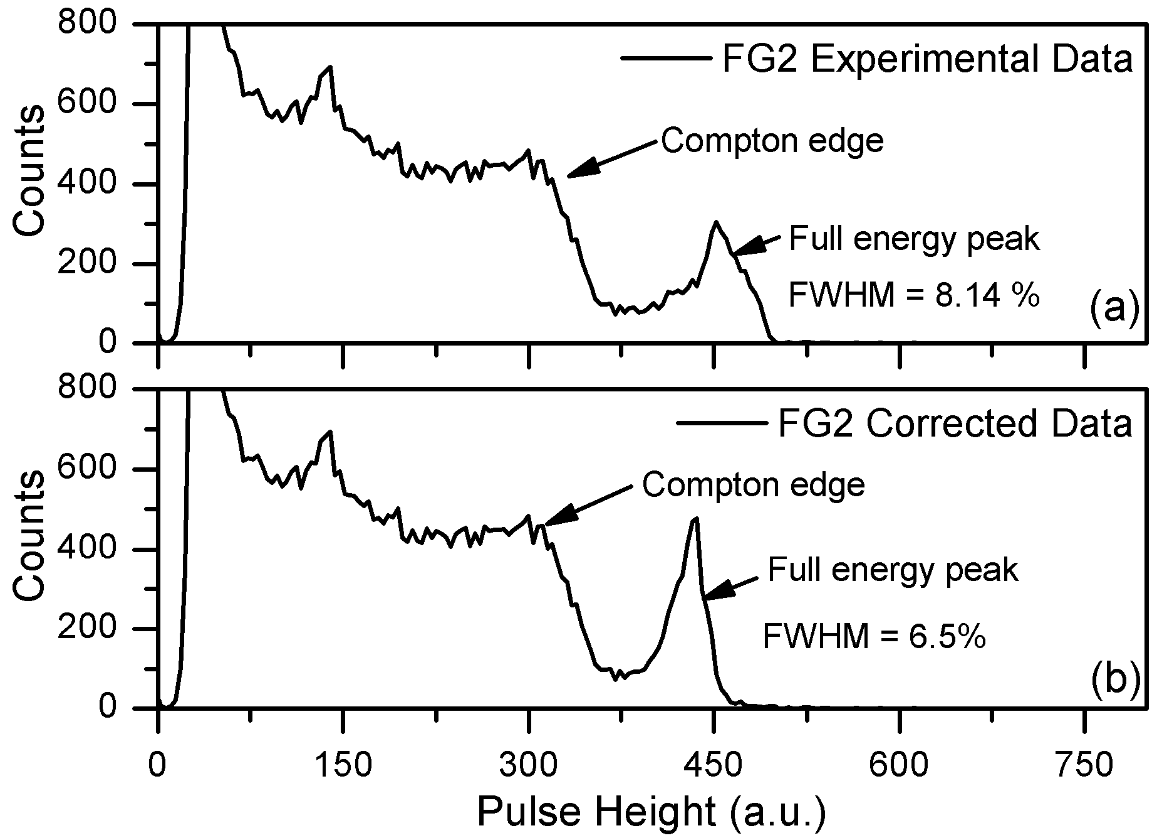


Figure 6.45. Pulse height distribution obtained (a) before and (b) after digital corrections from the digital radiation detection system for detector FG2.

### 6.7.4 Pixel Guard Ring Detector

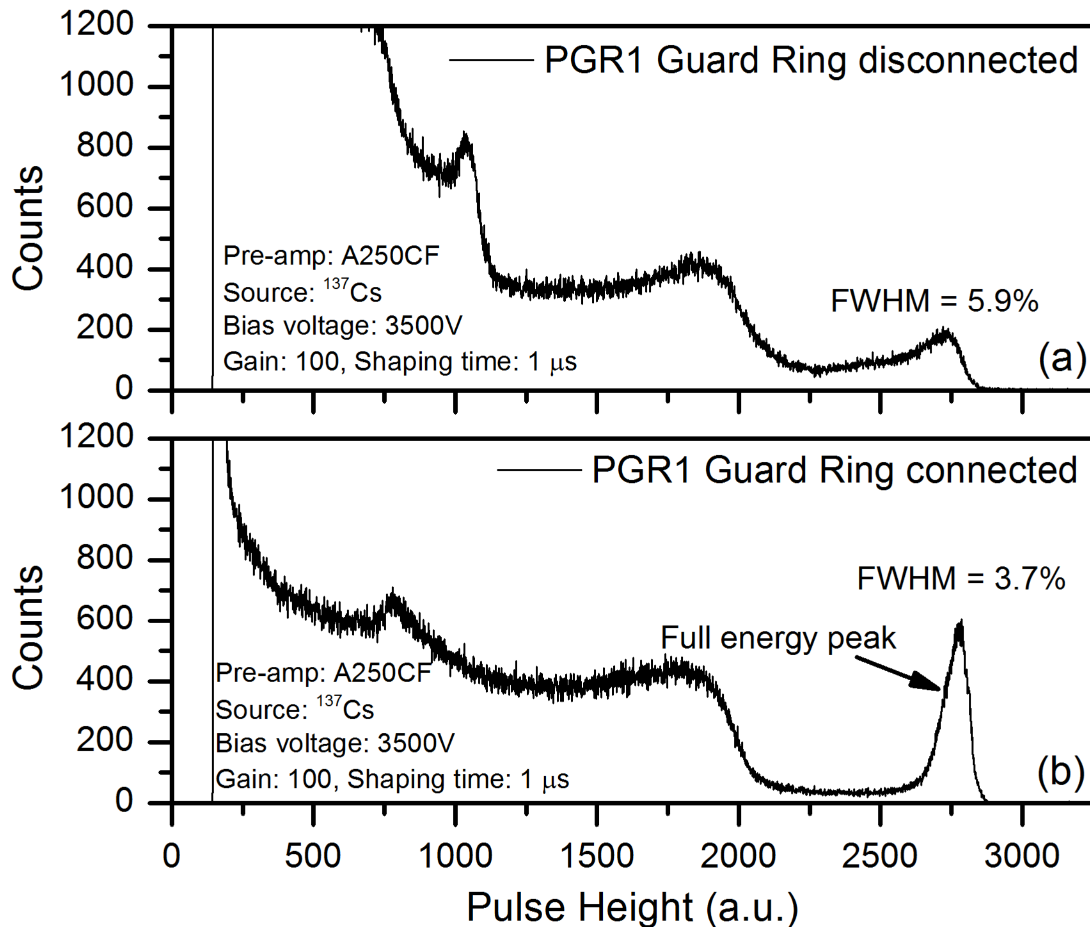


Figure 6.46. Analog pulse height spectrum obtained (a) with the guard ring disconnected and (b) with the guard ring connected for detector PGR1.

The pixel guard ring detector PGR1 was tested using $^{137}$Cs at 3500V bias first without the guard ring attached, whose results are shown in Figure 6.46a. The FWHM of the detector in this configuration was calculated to be 5.9%. Afterwards, the guard ring was biased to the same voltage as the anode pixel (0V bias), and PGR1 was retested using $^{137}$Cs, as shown in Figure 6.46b. The FWHM with the guard ring in use for detector PGR1 improved to 3.7% from 5.9%. This improvement in FWHM is substantial as a result of the use of the guard ring. In addition, the Compton background is seen to be well above the

photopeak when the guard ring is not in use, however the peak is more clearly resolved above the background after attaching the guard ring.

## 6.8 Conclusion

In this chapter, the solution-grown CZT crystals were fabricated into nuclear detectors and tested using gamma-ray energy sources. A variety of detector geometries were explored to work around the poor hole transport properties of CZT, such as the pixel guard ring detector and Frisch collar detector. Analog and digital pulse height measurements were performed to analyze detector behavior. Detection measurements using a Frisch collar configuration produced very clear high-energy gamma-ray peaks, with up to 1.4% energy resolution for $^{137}$Cs. A biparametric plot was generated using digital spectroscopy, which allowed for advanced interpretation of the detection spectra. While the planar configuration did not produce a clear gamma photopeak, a digital correction scheme was implemented to correct for the poor hole transport properties. After digital corrections, a photopeak with 1.6% energy resolution was obtained for a planar detector yielding no discernable peak for $^{137}$Cs high energy gamma-ray irradiation.

# CHAPTER 7: CONCLUSION AND FUTURE WORK

## 7.1 CONCLUSION

In this dissertation, a comprehensive investigation of CdZnTe for use as a gamma-ray nuclear detector has been performed, with crystals grown using a low temperature solution-growth method developed at USC. First, an overview of CZT and its advantages over other materials, as well as its drawbacks, was provided in the first chapter. In the second chapter, an overview of prior growth techniques along with the new solution-growth method were compared. Preparation for the crystal growth was performed using zone refining of the precursor materials and carbon coating of the quartz growth ampoules. Crystal growth of CZT was successfully performed using the solution-growth method, using 50% excess tellurium with indium as a dopant.

In Chapter 3, the grown crystals were processed using wafering, polishing, and etching in preparation for characterization. Optical transmission studies were performed to determine the band gap of the CZT, while EDS studies were performed to reveal the stoichiometry of the elemental Cd, Zn, and Te present in the grown crystals. Infrared imaging was performed to analyze the quantity and size of Te inclusions/precipitates, and electrical characterization was performed to ensure that only high resistive CZT crystals were fabricated into detectors. In Chapter 4, surface modification studies using sulfide passivation was performed on the grown CZT crystals. Passivation using $Na_2S$ and $(NH_4)_2S$ solutions were used to apply a passivating layer on the CZT surface. XPS studies revealed that the passivation techniques were successful at removing surface states, replacing them

with sulfur bonds. Electrical characterization of passivated samples revealed lower leakage current for the passivated surfaces than the unpassivated surfaces.

In Chapter 5, surface and deep-level defect studies were performed to determine the type and severity of defects present in the grown CZT crystals. TSC studies revealed the presence of hole traps with a large capture cross section. Chemical etching results revealed surface defects present on the surface which can affect the electrical properties of the CZT crystals. EBIC results combined with chemical etching images show clusters of dislocations and point defects within the bulk of the CZT crystals. In Chapter 6, nuclear detectors were fabricated from high-resistive CZT crystals, and nuclear detection properties were tested using gamma-ray sources. Analog and digital spectrum was collected and analyzed, and the results show that the solution-growth CZT detectors are very effective at detecting both low and high energy gamma-rays.

## 7.2 FUTURE WORK

While detector characterization of the solvent-grown CZT crystals showed very good performance, there are numerous areas of future research which must be undertaken to improve upon the existing body of information about crystals grown using this method. Future recommended work is as follows:

- Prior to fabrication of nuclear detectors, sulfur passivation should be applied to the CZT detector material, and detector characterization using $^{241}$Am and $^{137}$Cs can be performed to demonstrate the possible positive effects of surface modification on detector energy resolution.
- Other types of detector geometries, such as a co-planar and multiple small pixel detector structure, can be applied to CZT. For this study, only the planar, pixel

guard-ring, and Frisch collar detector structures were utilized to eliminate the effects of hole-trapping within the CZT detectors. The multiple pixel and co-planar detector structures are also well known detector structures, and have a good possibility of demonstrating strong detector performance when applied to the solvent-grown CZT crystals.

- Deep-level transient spectroscopy (DLTS) can be applied to the solvent-grown CZT crystals for further defect analysis. DLTS is a very sensitive technique for determining defects present in the space-charge region of a semiconductor material using voltage pulses. By using this spectroscopy technique, further information about the deep-level defects can be determined, which may assist future endeavors in reducing defects in the solvent-grown CZT crystals.

# REFERENCES


[1] A. Verger, W. Djaballah, N. Fourquet, F. Rouzet, G. Koehl, L. Imbert, S. Poussier, R. Fay, V. Roch, D. L. Guludec, G. Karcher and P.-Y. Marie, "Comparison between stress myocardial perfusion SPECT recorded with cadmium-zinc-telluride and Anger cameras in various study protocols," *European Journal of Nuclear Medicine and Molecular Imaging,* vol. 40, pp. 331-340, 2013.

[2] R. Nakazato1, D. S. Berman, S. W. Hayes, M. Fish, R. Padgett, Y. Xu1, M. Lemley, R. Baavour, N. Roth and P. J. Slomka, "Myocardial Perfusion Imaging with a Solid-State Camera: Simulation of a Very Low Dose Imaging Protocol," *Journal of Nuclear Medicine,* vol. 54, pp. 373-379, 2013.

[3] N. Zhang, A. Yeckel and J. J. Derby, "Maintaining convex interface shapes during electrodynamic gradient freeze growth of cadmium zinc telluride using a dynamic, bell-curve furnace profile," *Journal of Crystal Growth,* vol. 355, pp. 113-121, 2012.

[4] G. Yang, A. Bolotnikov, P. Fochuk, Y. Cui, G. S. Camarda, A. Hossain, K. H. Kim, J. Horace, B. McCall, R. Gul, O. Kopach, S. Egarievwe and R. James, "Post-growth Annealing of Cadmium Zinc Telluride Crystals for Room-Temperature Radiation Detectors," *Journal of Electronic Materials,* vol. 41, p. 2912, 2012.

[5] B. Milbrath, A. Peurrung, M. Bliss and W. Weber, "Radiation detector materials: An overview," *Journal of Materials Research,* vol. 23, pp. 2561-2581, 2008.

[6] S. D. Sordo, L. Abbene, E. Caroli, A. M. Mancini, A. Zappetteni and P. Ubertini, "Progress in the Development of CdTe and CdZnTe Semiconductor Radiation Detectors for Astrophysical and Medical Applications," *Sensors,* vol. 9, pp. 3491-3526, 2009.

[7] A. Owens and A. Peacock, "Compound semiconductor radiation detectors," *Nuclear Instruments and Methods in Physics Research A,* vol. 531, pp. 18-37, 2004.

[8] T. E. Schlesinger and R. B. James, Eds., Semiconductors for Room Temperature Nuclear Detector Applications, San Diego: Academic Press Inc., 1995.

[9] T. Schlesinger, J. Toney, H. Yoon, E. Lee, B. Brunett, L. Franks and R. James, "Cadmium zinc telluride and its use as a nuclear radiation detector material," *Materials Science and Engineering,* vol. 32, pp. 103-189, 2001.

[10] G. Dhanaraj, K. Byrappa, V. Prasad and M. Dudley, Eds., Springer Handbook of Crystal Growth, New York: Springer, 2010.

[11] "École Polytechnique de Montréal, Fact database," 2010. [Online]. Available: http://www.crct.polymtl.ca/fact/documentation/.

[12] M. J. Harrison, A. P. Graebner, W. J. McNeil and D. S. McGregor, "Carbon coating of fused silica ampoules," *Journal of Crystal Growth,* vol. 290, no. 2, pp. 597-601, 2006.

[13] W. G. Pfann, Zone Melting, 2 ed., Kreiger Publishing, 1978.

[14] W. R. Wilcox, Zone Refining, Kirk-Othmer Encyclopedia of Chemical Technology, John Wiley & Sons, 2001.

[15] Zone Refining, McGraw-Hill Science & Technology Encyclopedia, The McGraw-Hill Companies, Inc., 2005.

[16] K. C. Mandal, C. Noblitt, M. Choi, R. D. Rauh, U. N. Roy, M. Groza, A. Burger, D. E. Holcomb and G. E. J. Jr., "Crystal growth, characterization, and testing of CdZnTe single crystals for radiation detectors," in *SPIE Proceedings*, Denver, 2004.

[17] N. Kolesnikov, A. Kolchin, D. Alov, Y. Ivanov, A. Chernov, M. Schieber, H. Hermon, R. James, M. Goorsky, H. Yoon, J. Toney, B. Brunett and T. Schlesinger, "Growth and Characterization of p-type Cd(1- x)Zn(x)Te (x = 0.2, 0.3, 0.4)," *Journal of Crystal Growth,* vol. 174, pp. 256-262, 1997.

[18] P. Gille, F. Kiessling and M. Burkert, "A new approach to crystal growth of Hg(1-x)Cd(x)Te by the travelling heater method (THM)," *Journal of Crystal Growth,* vol. 114, pp. 77-86, 1991.

[19] U. Roy, A. Gueorguiev, S. Weiller and J. Stein, "Growth of spectroscopic grade Cd(0.9)Zn(0.1)Te:In by THM technique," *Journal of Crystal Growth,* vol. 312, pp. 33-36, 2009.

[20] H. Chen, S. A. Awadalla, F. Harris, P. Lu, R. Redden, G. Bindley, A. Copete, J. Hong, J. Grindlay, M. Amman, J. S. Lee, P. Luke, I. Kuvvetli and C. Budtz-Jorgensen, "Spectral Response of THM Grown CdZnTe Crystals," *IEEE Transactions on Nuclear Science,* vol. 55, pp. 1567-1572, 2008.

[21] U. Roy, S. Weiler and J. Stein, "Growth and interface study of 2 in diameter CdZnTe by THM technique," *Journal of Crystal Growth,* vol. 312, pp. 2840-2845, 2010.

[22] R. M. Krishna, T. C. Hayes, P. G. Muzykov and K. C. Mandal, "Low Temperature Crystal Growth and Characterization of Cd(0.9)Zn(0.1)Te for Radiation Detection Applications," *MRS Proceedings,* vol. 1341, pp. 39-44, 2011.

[23] G. Li, X. Zhang, H. Hua and W. Jie, "A Modified Vertical Bridgman Method for Growth of High-Quality Cd(1–x)Zn(x)Te Crystals," *Journal of Electronic Materials,* vol. 34, pp. 1215-1224, 2005.

[24] G. Cohen-Taguria, M. Levinshteina, A. Ruzinb and I. Goldfarb, "Real-space identification of the CZT(1 1 0) surface atomic structure by scanning tunneling microscopy," *Surface Science,* vol. 602, no. 3, pp. 712-723, 2008.

[25] B. Hafner, "Energy Dispersive Spectroscopy on the SEM: A Primer," Characterization Facility, University of Minnesota—Twin Cities.

[26] S. Wen-Bin, Y. Mei-Yun and W. Wen-Hai, "Crystal growth and characterization of CdTe from the melt under controlled Cd partial pressure," *Journal of Crystal Growth,* vol. 86, pp. 127-131, 1990.

[27] A. Nelson, A. Conway, C. Reinhardt, J. Ferreira, R. Nikolic and S. Payne, "X-ray photoemission analysis of passivated Cd(1-x)ZnxTe surfaces for improved radiation detectors," *Materials Letters,* vol. 63, no. 2, pp. 180-181, 2009.

[28] G. A. Carini, A. E. Bolotnikov, G. S. Camarda, G. W. Wright, R. B. James and L. Li, "Effect of Te precipitates on the performance of CdZnTe detectors," *Applied Physics Letters,* vol. 88, no. 14, p. 143515, 2006.

[29] A. Bolotnikov, G. Camarda, G. Carini, Y. Cui, L. Lib and R. James, "Cumulative effects of Te precipitates in CdZnTe radiation detectors," *Nuclear Instruments and Methods in Physics Research A,* vol. 571, no. 3, pp. 687-698, 2007.

[30] R. Krishna, S. Chaudhuri, K. Zavalla and K. Mandal, "Characterization of CdZnTe based virtual Frisch grid detectors for high," *Nuclear Instruments and Methods in Physics Research A,* vol. 701, pp. 208-213, 2013.

[31] A. Burger, H. Chen, K. Chattopadhyay, D. Shi, S. Morgan, W. Collins and R. James, "Characterization of metal contacts on and surfaces of cadmium zinc telluride," *Nuclear Instruments and Methods in Physics Research A,* vol. 428, pp. 8-13, 1999.

[32] S. M. Sze and K. K. Ng, "Metal-Semiconductor Contacts," in *Physics of Semiconductor devices*, Hoboken, New Jersey, John Wiley & Sons, Inc., 2007, pp. 134-190.

[33] D. R. Lide, Ed., CRC Handbook of Chemistry and Physics, 90 ed., Boca Raton: CRC Press/Taylor and Francis, 2010.

[34] T. Lauinger, J. Schmidt, A. G. Aberle and R. Hezel, "Record low surface recombination velocities on 1 Ω cm p-silicon using remote plasma silicon nitride passivation," *Applied Physics Letters,* vol. 68, p. 1232, 1996.

[35] A. Nelson, A. Conway, C. Reinhardt, J. F. R. Nikolic and S.A.Payne, "X-ray photoemission analysis of passivated Cd(1-x)ZnxTe surfaces for improved radiation detectors," *Materials Letters,* vol. 63, pp. 180-181, 2008.

[36] S. Babar, P. Sellin, J. Watts and M. Baker, "An XPS study of bromine in methanol etching and hydrogen peroxide passivation treatments for cadmium zinc telluride radiation detectors," *Applied Surface Science,* vol. 264, pp. 681-686, 2013.

[37] K. Chattopadhyay, M. Hayes, J.-O. Ndap, A. Burger, W. J. Lu, H. G. McWhinney, T. Grady and R. B. James, "Surface Passivation of Cadmium Zinc Telluride Radiation Detectors by Potassium Hydroxide Solution," *Journal of Electronic Materials,* vol. 29, no. 6, pp. 708-712, 2000.

[38] S. H. Park, J. H. Ha, Y. H. Cho, H. S. Kim, S. M. Kang, Y. K. Kim and J. K. Kim, "Surface Passivation Effect on CZT-Metal Contact," *IEEE Transactions on Nuclear Science,* vol. 55, no. 3, pp. 1547-1550, 2008.

[39] C. J. Sandroff, R. N. Nottenburg, J. Bischoff and R. Bhat, "Dramatic enhancement in the gain of a GaAs/AlGaAs heterostructure bipolar transistor by surface chemical passivation," *Applied Physics Letters,* vol. 51, p. 33, 1987.

[40] T. Ohno, "Sulfur passivation of GaAs surfaces," *Physical Review B,* vol. 44, no. 12, pp. 6306-6311, 1991.

[41] B. A. Parkinson, A. Heller and B. Miller, "Effects of Cations on the Performance of the Photoanode in the n-GaAs|K2Se-K2Se2-KOH|C Semiconductor Liquid Junction Solar Cell," *Electrochemical Science and Technology,* vol. 126, no. 6, pp. 954-960, 1979.

[42] A. Heller, "Conversion of Sunlight into Electrical Power and Photoassisted Electrolysis of Water in Photoelectrochemical Cells," *Accounts of Chemical Research,* vol. 14, pp. 154-162, 1981.

[43] S. Kasap and P. Capper, Eds., Springer Handbook of Electronic and Photonic Materials, New York: Springer Science, 2006.

[44] T. B. Wu, J. S. Chen, C. D. Chiang, Y. M. Pang and S. J. Yang, "Study on polished and etched surfaces of polar (111) CdTe by xray photoelectron spectroscopy and grazingincidence xray diffraction," *Journal of Applied Physics,* vol. 71, pp. 5212-5216, 1992.

[45] P. Bartolo-Pérez, M. Farías, R. Castro-Rodríguez and J. Peña, "XPS analysis of oxidation states of Te in CdTe oxide films grown by rf sputtering with an Ar-NH3 plasma," *Superficies y Vacío,* vol. 12, pp. 8-11, 2001.

[46] K.-T. Chen, D. T. Shi, H. Chen, B. Granderson, M. A. George, W. E. Collins, A. Burger and R. B. James, "Study of oxidized cadmium zinc telluride surfaces," *Journal of Vacuum Science and Technology A,* vol. 15, pp. 850-853, 1997.

[47] D. W. Niles, D. Waters and D. Rose, "Chemical reactivity of CdCl wet-deposited on CdTe films studied by X-ray photoelectron spectroscopy," *Applied Surface Science,* vol. 136, pp. 221-229, 1998.

[48] M. George, M. Azoulay, H. Jayatirtha, A. Burger, W. Collins and c. E. Silberman, "X-ray photoelectron spectroscopy and atomic force microscopy characterization of the effects of etching Zn(x)Cd(1-x)Te surfaces," *Surface Science,* vol. 296, no. 2, pp. 231-240, 1993.

[49] A. A. Rouse, C. Szeles, J.-O. Ndap, S. A. Soldner, K. B. Parnham, D. J. Gaspar, M. H. Engelhard, A. S. Lea, S. V. Shutthanandan, T. S. Thevuthasan and D. R. Baer, "Interfacial Chemistry and the Performance of Bromine-Etched CdZnTe Radiation Detector Devices," *IEEE Transactions on Nuclear Science,* vol. 49, no. 4, pp. 2005-2009, 2002.

[50] J. Häring, J. G. Werthen, R. H. Bube, L. Gulbrandsen, W. Jansen and P. Luscher, "Study of cleaved, oxidized, etched, and heattreated CdTe surfaces," *Journal of Vacuum Science and Technology A,* vol. 1, pp. 1469-1472, 1983.

[51] Y. S. Wu, C. R. Becker, A. Waag, R. Schmiedl, S. Einfeldt and G. Landwehr, "Oxygen on the (100) CdTe surface," *Journal of Applied Physics,* vol. 73, pp. 7385-7388, 1993.

[52] K. H. Kim, J. H. Won, S. H. Cho, J. H. Suh, P. K. Cho, J. Hong, S. U. Kim and Y. R. Han, "Passivation of Semi-Insulating Polycrystalline CdZnTe Films," *Journal of the Korean Physical Society,* vol. 53, no. 1, pp. 317-321, 2008.

[53] B. H. Parker, C. M. Stahle, S. D. Barthelmy, A. M. Parsons, J. Tueller, J. T. VanSant, B. F. Munoz, S. J. Snodgrass and R. E. Mullinix, "Correlation between bulk material defects and spectroscopic response in cadmium zinc telluride detectors," in *Proceedings of SPIE 3768: Hard X-Ray, Gamma-Ray, and Neutron Detector Physics*, Denver, CO, 1999.

[54] M. Schieber, T. Schlesinger, R. James, H. Hermon, H. Yoon and M. Goorsky, "Study of impurity segregation, crystallinity, and detector performance of melt-

grown cadmium zinc telluride crystals," *Journal of Crystal Growth,* Vols. 237-239, p. 2082–2090, 2002.

[55] C. Szeles, "CdZnTe and CdTe materials for X-ray and gamma ray radiation detector applications," *Physica Status Solidi B,* vol. 241, no. 3, pp. 783-790, 2004.

[56] D. K. Schroder, Semiconductor Material and Device Characterization, New York: John Wiley & Sons, Inc., 1998.

[57] H. Wright and G. Allen, "Thermally stimulated current analysis," *British Journal of Applied Physics,* vol. 17, pp. 1181-1185, 1966.

[58] Y. Lu, R. K. Route, D. Elwell and R. S. Feigelson, "Etch pit studies in CdTe crystals," *Journal of Vacuum Science and Technology A,* vol. 3, no. 1, pp. 264-270, 1985.

[59] M. Inoue, I. Teramoto and S. Takayanagi, "Etch Pits and Polarity in CdTe Crystals," *Journal of Applied Physics,* vol. 33, p. 2578, 1962.

[60] C. Parish, D. Batchelor, C. Progl and P. Russell, "Tutorial: Electron Beam-Induced Current in the Scanning Electron Microscope," *Microscopy and Analysis,* pp. 11-13, September 2007.

[61] Z. -Q. Fang, B. Claflin, D. C. Look, L. Polenta and W. C. Mitchel, "Thermally stimulated current spectroscopy of high-purity semi-insulating 4H-SiC substrates," *Journal of Electronic Materials,* vol. 34, no. 4, pp. 336-340, 2005.

[62] K. C. Mandal, P. G. Muzykov, R. Krishna, T. Hayes and T. S. Sudarshan, "Thermally stimulated current and high temperature resistivity measurements of 4H semi-insulating silicon carbide," *Solid State Communications,* vol. 151, no. 7, pp. 532-535, 2011.

[63] N. Krsmanovic, K. G. Lynn, M. H. Weber, R. Tjossem, T. Gessmann, C. Szeles, E. E. Eissler, J. P. Flint and H. L. Glass, "Electrical compensation in CdTe and CdZnTe by intrinsic defects," *Physical Review B,* vol. 62, no. 24, pp. R16 279-282, 2000.

[64] R. Soundararajan, K. Lynn, S. Awadallah, C. Szeles and S.-H. Wei, "Study of Defect Levels in CdTe Using Thermoelectric Effect Spectroscopy," *Journal of Electronic Materials,* vol. 35, no. 6, pp. 1333-1340, 2006.

[65] AZoNano, "Fundamentals of Contact Mode and TappingMode Atomic Force Microscopy," 18 May 2012. [Online]. Available: http://www.azonano.com/article.aspx?ArticleID=3010.

[66] L. C. Teague, M. C. Duff, J. R. Cadieux, R. Soundararajan, C. R. S. Jr. and K. G. Lynn, "Characterization of etch pit formation via the Everson-etching method on CdZnTe crystal surfaces from the bulk to the nanoscale," *Nuclear Instruments and Methods in Physics Research A,* vol. 652, pp. 178-182, 2011.

[67] T. Soga, T. Jimbo and M. Umeno, "Low etch pit density GaAs on Si grown by metalorganic chemical vapor deposition," *Applied Physics Letters,* vol. 56, p. 1433, 1990.

[68] Y. Lu, R. S. Feigelson, R. K. Route and Z. U. Rek, "A study of the defect structures in CdTe crystals using synchrotron x-ray topography," *Journal of Vacuum Science and Technology A,* vol. 4, p. 2190, 1986.

[69] C. Donolato, "On the theory of SEM charge-collection imaging of localized defects in semiconductors," *Optik,* vol. 52, pp. 19-36, 1978.

[70] P. G. Muzykov, R. Krishna, S. Das, T. Hayes, T. S. Sudarshan and K. C. Mandal, "Characterization of 4H semi-insulating silicon carbide single crystals using electron beam induced current," *Materials Letters,* vol. 65, pp. 911-914, 2011.

[71] R. M. Krishna, P. G. Muzykov and K. C. Mandal, "Electron beam induced current imaging of dislocations in CdZnTe crystal," *Journal of Physics and Chemistry of Solids,* vol. 74, pp. 170-173, 2013.

[72] S. I. Maximenko, S. R. Messenger, C. D. Cress, J. J. A. Freitas and R. J. Walters, "Application of CL/EBIC-SEM Techniques for Characterization of Radiation Effects in Multijunction Solar Cells," *IEEE Transactions on Nuclear Science,* vol. 57, pp. 3095-3100, 2010.

[73] G. F. Knoll, Radiation Detection and Measurement, 3rd ed., New York: John Wiley & Sons, Inc., 2000.

[74] Z. He, "Review of the Shockley–Ramo theorem and its application in semiconductor gamma-ray detectors," *Nuclear Instruments and Methods in Physics Research A,* vol. 463, pp. 250-267, 2001.

[75] W. Shockley, "Currents to conductors induced by a moving point charge," *Journal of Applied Physics,* vol. 9, pp. 635-636, 1938.

[76] S. Ramo, "Currents induced by electron motion," *Proceedings of the I.R.E.,* p. 584, 1939.

[77] H. Spieler, Semiconductor Detector Systems, Oxford: Oxford Science, 2005.

[78] A. H. Goldan and K. S. Karim, "Unipolar Charge Sensing Using Frisch Grid Technique for Amorphous Selenium Radiation Detectors," *Proceedings of SPIE,* vol. 7079, p. 70790P1, 2008.

[79] H. H. Barrett, J. Eskin and H. B.Barber, "Charge Transport in Arrays of Semiconductor Gamma-Ray Detectors," *Physical Review Letters,* vol. 75, pp. 156-159, 1995.

[80] D. McGregor, R. Rojeski, Z. He, D. Wehe, M. Driver and M. Blakely, "Geometrically weighted semiconductor Frisch grid radiation spectrometers," *Nuclear Instruments and Methods in Physics Research A,* vol. 422, pp. 164-168, 1999.

[81] O. Frisch, "British Atomic Energy Report," 1944.

[82] Y. Cui, A. Bolotnikov, G. Camarda, A. Hossain, G. Yang and R. James, "CZT Virtual Frisch-grid Detector: Principles and Applications," in *IEEE Long Island Systems, Applications and Technology Conference*, Farmingdale, NY, 2009.

[83] "Wikipedia," 16 May 2010. [Online]. Available: http://en.wikipedia.org/wiki/Analog-to-digital_converter.

[84] M. Nakhostin, "Recursive Algorithms for Real-Time Digital CR-(RC)^n Pulse Shaping," *IEEE Transactions on Nuclear Science,* vol. 58, no. 5, pp. 2378-2381, 2011.

[85] L. Verger, J. P. Bonnefoy, F. Glasser and P. Ouvrier-Buffet, "New Developments in CdTe and CdZnTe Detectors for X and y-Ray Applications," *Journal of Electronic Materials,* vol. 26, pp. 738-744, 1997.

[86] S. K. Chaudhuri, A. Lohstroh, M. Nakhostin and P. J. Sellin, "Digital pulse height correction in HgI2 γ-ray detectors," *Journal of Instrumentation,* vol. 7, p. T04002, 2012.

[87] J. C. Erickson, H. W. Yao, R. B. James, H. Hermon and M. Greaves, "Time of Flight Experimental Studies of CdZnTe Radiation Detectors," *Journal of Electronic Materials,* vol. 29, pp. 699-703, 2000.

[88] K. Hecht, "Zum Mechanismus des lichtelektrischen Prim¨arstroms in iso-lierenden Kristallen," *Z. Physik,* vol. 77, pp. 235-245, 1932.

[89] S. Miyajima, H. Sakuragi and M. Matsumoto, "Extraction of mean free path of charge carriers in CdZnTe crystals from measured full-energy peaks," *Nuclear Instruments and Methods in Physics Research A,* vol. 485, p. 533–538, 2002.

[90] S. N. Ahmed, Physics & Engineering of Radiation Detection, San Diego: Elsevier, 2007.

[91] J. Philippot, "Automatic Processing of Diode Spectrometry Results," *IEEE Transactions on Nuclear Science,* vol. 17/3, pp. 446-488, 1970.

[92] G. A. Armantrout, "Sensitivity Problems in Biological and Environmental Counting," *IEEE Transactions on Nuclear Science,* vol. 19/1, pp. 107-116, 1972.

[93] P. N. Luke, "Single-polarity charge sensing in ionization detectors using coplanar electrodes," *Applied Physics Letters,* vol. 65, p. 2884, 1994.

[94] J. G. Simmons and G. W. Taylor, "High-Field Isothermal Currents and Thermally Stimulated Currents in Insulators Having Discrete Trapping Levels," *Physical Review B,* vol. 5, no. 4, pp. 1619-1629, 1972.

[95] L. Chibani, M. Hage-Ali and P. Siffert, "Electrically active defects in detector-grade CdTe:Cl and CdZnTe materials grown by THM and HPBM," *Journal of Crystal Growth,* vol. 161, pp. 153-158, 1996.

# APPENDIX A – CARBON COATER MECHANICAL DRAWINGS

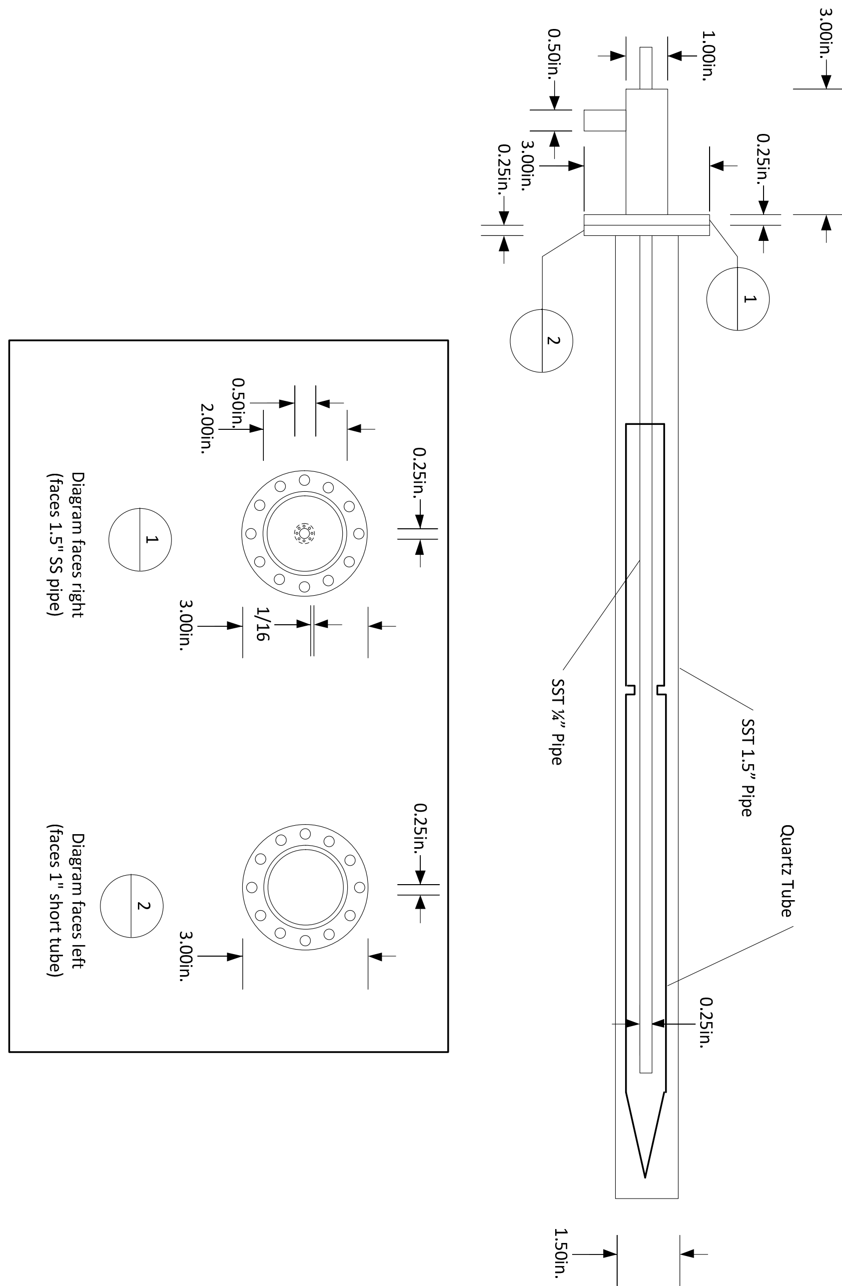

# APPENDIX B – CRYSTAL GROWTH FURNACE SOFTWARE

Arduino Code:

```
/*-----------------------------------------------
+++++++++++++++++++++++++++++++++++++++++++++++++
Pulling and Rotation Software for Crystal Growth Furnaces
Authors: Tim Hayes and Ramesh Krishna
+++++++++++++++++++++++++++++++++++++++++++++++++
-----------------------------------------------*/

#include <TimedAction.h>
/* This can be downloaded from
http://www.arduino.cc/playground/Code/TimedAction. This allows a
function to be repeated every X milliseconds. No variables may be
passed to this function through TimedAction. This function is now
included in the Wiring software.*/

#include <Messenger.h>
//This is the messenger function, to simplify communication between the
arduino and computer. This function is now included in the Wiring
software.

/****************************
* Input/Output Variables from Arduino Board *
****************************/
//Digital Pins for Arduino Board
int upPin = 8; //Tells motor to move up
int downPin = 9; //Tells motor to move down
int rotforwardPin = 11; //Tells rotation motor to rotate forward
int rotbackwardPin = 12; //Tells rotation motor to rotate backwards.

//Digital PWM output
int pulseoutPin = 5; //Outputs pulses to move the actuator
int rotatePin = 3; //Outputs pulses to the rotation motor

// Variables for GUI control
unsigned long delaymotortime; //Rate of movement in milliseconds per
tick, which will be fed to the timedaction function for stepping the
motor.
unsigned long reversedelaymotortime; //Rate of reverse movement in
milliseconds per tick, which will be fed to the timedaction function
for stepping the motor.
boolean moveconstantly = false; //Motor should move until a signal from
the computer says to stop.
long starttime; //When the puller started operation.
long endtime; //When the puller should stop operation.
```

```
long currentticks = 0; //How many ticks have elapsed since starting
puller operation.
long totalticks = 0; //How many ticks should the motor go.
int reverseticks = 0; //Number of ticks to go reverse. Is a function of
forward ticks.

//Values used passed from the GUI
unsigned long compinput[9]; //Array where variables are stored
int pulleropmode; //Mode of operation for the puller.
int rotationopmode; //Mode of operation for the rotation system.
unsigned long pullerendPosition; //Number of encoder pulses before the
motor will finish moving.
unsigned long pullermovetime; //Total time of pulling.
unsigned long revpullermovetime; //Total time of reverse pulling.
unsigned long pullerdelay;
unsigned long rotationdelay;
int rotationspeed;

//Values to process puller and rotation delays
unsigned long startpullermillis = 0; //Tells when the puller should
start pulling.
unsigned long initialpullermillis = 0; //Tells what time it is now
relative to when the puller should start.
unsigned long startrotmillis = 0;
unsigned long initialrotmillis = 0;
unsigned long acrtrotformillis = 0;
unsigned long acrtcurrmillis = 0;
unsigned long acrtcheckmillis = 0;

int motordelaypulse = 20; //Length of time the motor shall be kept on
(in milliseconds). This is the length of the pulse sent by the Minimum
Pulse Motor Movement Function, or pulsemotor().
int numberofpulses = 1130; //Number of pulses for 1" for VB2.
//int numberofpulses = 790; //Number of pulses for 1" for VB1.


int forwardrunsvar = 0; //How many times the puller has completed a
forward run.
int reverserunsvar = 0; //How many times the puller has completed a
reverse run.
int totalrunsvar = 0; //How many times the puller needs to run.
int currentrunmode; //Tells whether the motor should run in forward
mode (has value of 1), reverse mode ( value of 2), or do nothing (value
of 0).

Messenger message = Messenger();

TimedAction timedmotorpulse = TimedAction(10000,pulsemotor); //Calls
the pulsemotor function once every delaymotortime milliseconds.
Hardcoded for 10 seconds, but this will be changed in the code below.

TimedAction reversemotorpulse = TimedAction(10000,pulsemotor); //Calls
the pulsemotor function once every delaymotortime milliseconds.
Hardcoded for 10 seconds, but this will be changed in the code below.

TimedAction statusupdateaction = TimedAction(10000,statusupdate);
//Calls the statusupdate function once every 10000 milliseconds.
```

```
/****************************
* Set-Up Function *
****************************/
//Function to set up Arduino
void setup() {
      Serial.begin(9600); //Initialize the Serial output (USB) for
 communication
      message.attach(messageCompleted); //Run messageCompleted when a
 message is processed.
    pinMode(upPin, OUTPUT); //Defines upPin (Digital Pin 8) as an
Output
    pinMode(downPin, OUTPUT); //Defines downPin (Digital Pin 9) as an
Output
    pinMode(pulseoutPin, OUTPUT); //Defines pulseoutPin (Digital Pin 5,
PWM) as an Output
    pinMode(rotatePin, OUTPUT); //Defines rotatePin (Digital Pin 3) as
a PWM output

      pinMode(rotforwardPin, OUTPUT); //Defines rotforwardPin (Digital
Pin 11) as an output
      pinMode(rotbackwardPin, OUTPUT); //Defines rotbackwardPin
(Digital Pin 12) as an output

    pulleropmode = 1; //Start the puller in the off mode.
      rotationopmode = 1; //Start the rotation system in the off mode.
    mode(); //Put it in off mode.

}

/****************************
* Main Program *
****************************/
//Main program for Puller operation

void loop(){
//Note: 1 encoder pulse is equal to 0.5291666667 mm (48 pulses = 1
inch, according to http://www.sadoun.com/Sat/Products/S/HARL-3618-TD-
18-Moteck-Actuator.htm) For 18 inch actuator, total number of pulses is
864.
while ( Serial.available() ) message.process( Serial.read() ); //Let
messenger take care of serial input.
statusupdateaction.check(); //Send status updates on a regular
interval.

if(pulleropmode == 4 || pulleropmode==5)
{
      if((forwardrunsvar < totalrunsvar) && (currentrunmode == 1))
        forwardrun();
    if((reverserunsvar <= totalrunsvar) && (currentrunmode == 2))
        reverserun();
    if((forwardrunsvar >= totalrunsvar) && ((reverserunsvar+1) >=
totalrunsvar))
      {
```

```
        pulleropmode = 1;
        rotationopmode = 1;
        mode();
      }
}

if(rotationopmode == 4)
    acrtrotforward();

}
```

```
/***************************
* Minimum Pulse Motor Movement Function *
***************************/
//Issues one pulse to the H-Bridge to move the motor for a set time in
milliseconds (hardcoded).
void pulsemotor()
{
      analogWrite(pulseoutPin, 255);
      delay(motordelaypulse); //Hard-coded the length of time the
motor will run high before cutting off at currently 30 milliseconds,
every time this function is called.
      analogWrite(pulseoutPin,0);
      if (currentrunmode == 2)
          currentticks--;
      else
            currentticks++;
      Serial.print("Current Tick: ");
      Serial.println(currentticks);
}
```

```
/***************************
* Move Motor Completely Function *
***************************/
//
void moveallway()
{
    while(moveconstantly == true)
    {
          analogWrite(pulseoutPin, 255);
            delay(motordelaypulse); //Hard-coded the length of time
      the motor will run high before cutting off at currently 30
      milliseconds, every time this function is called.
            analogWrite(pulseoutPin,0);
            while ( Serial.available() ) message.process( Serial.read()
      ); //Check if computer is sending the stop signal
    }
}


/***************************
```

```
* Get info Function *
****************************/
//Function used to get the user input from the GUI. GUI sends 7
variables to the arduino.
//Variables to arduino from GUI: 1. puller mode of operation, 2.
rotation mode of operation 3. total puller distance (number of encoder
pulses to go) 4. puller total time of movement (in seconds) 5. puller
delay time (before begining to pull) 5. rotation speed (PWM units) 6.
Rotation delay time (before begining to rotate 7. Number of runs to
perform.

void messageCompleted() {
      int count=0;
      while ( message.available() ) {
      compinput[count] = message.readLong();
      count++;
      }
      if(compinput[0] != 0){
          pulleropmode = compinput[0];
          //25ms pulses at 850 pulses for 1"
            pullerendPosition = (compinput[2]*numberofpulses)/100;
      //This definition takes the value given by the computer,
      multiplies it by the number of ticks per inch, and divides by a
      scaling factor of 100. 100 is the scaling factor because longs in
      C do not store decimal places, and I wanted to send fractions of
      an inch. So, the computer sends a fraction of an inch times 100,
      and the arduino divides it again.
        pullermovetime = compinput[3];
        pullerdelay = compinput[4];
        totalrunsvar = compinput[5];
        revpullermovetime = compinput[8];
            }
    if(compinput[1] != 0){
            rotationopmode = compinput[1];
            rotationspeed = compinput[6];
            rotationdelay = compinput[7];
            }
      memset(compinput, 0, sizeof(compinput)); //Zero the array when
      done.
      statusupdate();
      mode();
 }




/****************************
* Operation Mode Function *
****************************/
//This function will determine how the motor will run, by setting
variable values.
void mode()
{
    if(pulleropmode == 1) //Mode 1 shuts off all puller output.
      {
          moveconstantly = false;
          digitalWrite(upPin, LOW);
```

```
        digitalWrite(downPin, LOW);
          timedmotorpulse.disable();
          reversemotorpulse.disable();
          statusupdateaction.disable();
          digitalWrite(pulseoutPin, LOW);
          currentticks = 0;
          totalticks = 0;
          initialpullermillis = 0;
          startpullermillis = 0;
          currentrunmode = 0;
          forwardrunsvar = 0;
          reverserunsvar = 0;
          totalrunsvar = 0;
    }

    if(pulleropmode == 2) //Mode 2 forces the puller all the way up.
    {
        moveconstantly = true; //Move constantly.
          digitalWrite(upPin, HIGH);
          digitalWrite(downPin, LOW);
          moveallway();
          timedmotorpulse.disable();
          reversemotorpulse.disable();
          statusupdateaction.disable();
          currentrunmode = 0;
          forwardrunsvar = 0;
          reverserunsvar = 0;
          totalrunsvar = 0;
    }

    if(pulleropmode == 3) //Mode 3 forces the puller all the way
down.
    {
        moveconstantly = true; //Move constantly.
          digitalWrite(upPin, LOW);
          digitalWrite(downPin, HIGH);
          moveallway();
          timedmotorpulse.disable();
          reversemotorpulse.disable();
          statusupdateaction.disable();
          currentrunmode = 0;
          forwardrunsvar = 0;
          reverserunsvar = 0;
          totalrunsvar = 0;
    }


    if(pulleropmode == 4) //Mode 4 begins pulling upwards.
    {
          initialpullermillis = 0;
          startpullermillis = 0;
        moveconstantly = false; //Dont move constantly.
          digitalWrite(upPin, HIGH); //Enable upwards movement.
          digitalWrite(downPin, LOW);
        calculate(); //Calculate the delaymotortime.
        initialpullermillis = millis();
        startpullermillis = pullerdelay + initialpullermillis;
```

```
            timedmotorpulse.enable(); //Turn on the TimedAction
      timedmotorpulse.
            timedmotorpulse.setInterval(delaymotortime); //Changes the
      delay interval for running the motor, based on the value of
      delaymotortime.
            reversemotorpulse.enable(); //Turn on the TimedAction
      reversemotorpulse.
            reversemotorpulse.setInterval(reversedelaymotortime);
      //Changes the delay interval for reverse running the motor, based
      on the value of reversedelaymotortime.
            statusupdateaction.enable();
            currentrunmode = 1;
            forwardrunsvar = 0;
            reverserunsvar = 0;
      }

      if(pulleropmode == 5) //Mode 5 begins pulling downwards.
      {
            initialpullermillis = 0;
            startpullermillis = 0;
          moveconstantly = false;
            digitalWrite(upPin, LOW);
            digitalWrite(downPin, HIGH);
          calculate(); //Calculate the delaymotortime.
          initialpullermillis = millis();
          startpullermillis = pullerdelay + initialpullermillis;
            timedmotorpulse.enable(); //Turn on the TimedAction
      timedmotorpulse.
            timedmotorpulse.setInterval(delaymotortime); //Changes the
      delay interval for running the motor, based on the value of
      delaymotortime.
            reversemotorpulse.enable(); //Turn on the TimedAction
      reversemotorpulse.
            reversemotorpulse.setInterval(reversedelaymotortime);
      //Changes the delay interval for reverse running the motor, based
      on the value of reversedelaymotortime.
            statusupdateaction.enable();
            currentrunmode = 1;
            forwardrunsvar = 0;
            reverserunsvar = 0;
      }


    if(rotationopmode == 1) //Mode 1 shuts off all rotation output.
      {
          digitalWrite(rotforwardPin, LOW);
          digitalWrite(rotbackwardPin, LOW);
         analogWrite(rotatePin,0); //Output the Rotation PWM to Digital
Pin 3. Duty cycle is out of a maximum value of 255 (where 255 is 100%
duty cycle).
      }

    if(rotationopmode == 2) //Mode 2 enables rotation forward.
      {
          digitalWrite(rotforwardPin, HIGH);
          digitalWrite(rotbackwardPin, LOW);
```

```
         analogWrite(rotatePin,rotationspeed); //Output the Rotation
PWM to Digital Pin 3. Duty cycle is out of a maximum value of 255
(where 255 is 100% duty cycle).
      }

    if(rotationopmode == 3) //Mode 3 enables rotation backwards.
      {
          digitalWrite(rotforwardPin, LOW);
          digitalWrite(rotbackwardPin, HIGH);
         analogWrite(rotatePin,rotationspeed); //Output the Rotation
PWM to Digital Pin 3. Duty cycle is out of a maximum value of 255
(where 255 is 100% duty cycle).
      }

    if(rotationopmode == 4)
    {
          digitalWrite(rotforwardPin, LOW);
          digitalWrite(rotbackwardPin, LOW);
         analogWrite(rotatePin,0);
           acrtcurrmillis = 0;
           acrtrotformillis = 0;
           acrtcheckmillis = 0;
    }
}


/***************************
* ARCT Rotation Function *
****************************/
//Function to do ACRT rotation
void acrtrotforward() {
    acrtcurrmillis = millis();
      acrtcheckmillis = acrtcurrmillis - acrtrotformillis;
    if (acrtcheckmillis > 0 && acrtcheckmillis <= 1000){
          digitalWrite(rotforwardPin, HIGH);
          digitalWrite(rotbackwardPin, LOW);
         analogWrite(rotatePin,rotationspeed);
        }
    if (acrtcheckmillis >= 1000 && acrtcheckmillis <= 2000){
          digitalWrite(rotforwardPin, LOW);
          digitalWrite(rotbackwardPin, LOW);
         analogWrite(rotatePin,0);
        }
    if (acrtcheckmillis > 2000)
        acrtrotformillis = millis();
}

/***************************
* Calculate Function *
***************************/
//This function will calcuate the number of seconds per tick (the
minimum rate of movement of the puller). It will multiply the ticks per
encoder count times the total encoder counts to go, then divide the
total number of seconds to pull by this number. This number will later
be fed to the TimedAction function.
void calculate()
{
```

```
    long movetimems = pullermovetime*1000; //Calculate movetime in
milliseconds.
    long revmovetimems = revpullermovetime*1000; //Calculate
revmovetime in milliseconds.
    totalticks = pullerendPosition; //Multiplies the total movement
distance (from computer) by the number of ticks per encoder pulse.
    if (pulleropmode==5)
            reverseticks = totalticks*1.06666; //Adjusts the reverse
      movement ticks to adjust for gravity.
      if (pulleropmode==4)
            reverseticks = totalticks*0.9375; //Adjusts the reverse
      movement ticks to adjust for gravity.
    delaymotortime = movetimems/totalticks; //Get the
milliseconds/tick.
    reversedelaymotortime = revmovetimems/reverseticks; //Get reverse
milliseconds/tick.
      Serial.print("Movement Rate: ");
      Serial.println(delaymotortime);
      Serial.println();
}



/****************************
* Single Run Function *
****************************/
//This function will run the motor one complete run forward.
void forwardrun()
{

    //Checks to see if its time to start the puller. If it is time, it
resets the variables, and calls timedmotorpulse to move the motor. If
not yet time, it sets initialpullermillis to the current time, and
checks again.
    if(pulleropmode == 4 && (startpullermillis - initialpullermillis)
<= 0 && currentticks < totalticks){
          startpullermillis = 0;
          initialpullermillis = 0;
            digitalWrite(upPin, HIGH); //Enable upwards movement.
            digitalWrite(downPin, LOW);
          timedmotorpulse.check(); //Performs the timedmotorpulse
      delayed action, which pulses the motor and stops for the amount
      of time specified in "delaymotortime"
          }
      else if(pulleropmode == 4 && (startpullermillis -
initialpullermillis) > 0)
           initialpullermillis = millis();

    if(pulleropmode == 5 && (startpullermillis - initialpullermillis)
<= 0 && currentticks < totalticks){
          startpullermillis = 0;
          initialpullermillis = 0;
            digitalWrite(upPin, LOW);
            digitalWrite(downPin, HIGH); //Enable downwards movement.
          timedmotorpulse.check(); //Performs the timedmotorpulse
      delayed action, which pulses the motor and stops for the amount
      of time specified in "delaymotortime"
```

```
        }
    else if(pulleropmode == 5 && (startpullermillis -
initialpullermillis) > 0)
           initialpullermillis = millis();

      if((currentticks >= totalticks) && (totalticks > 0)){
            forwardrunsvar++;
          currentrunmode = 2;
            initialpullermillis = millis();
          startpullermillis = pullerdelay + initialpullermillis;
          currentticks = reverseticks;
            statusupdate();
      } //Checks to see if the motor has moved all the ticks that it
      needs to in order to complete the forward run. If it completes
      the forward run, it logs it as a completed forward run, and puts
      the motor into reverse mode. Checks based on the calculated total
      number of ticks, and the number of ticks recorded by the minimum
      movement function.

}


/****************************
* Reverse Run Function *
****************************/
//This function will retract the motor fully once.
void reverserun()
{
      if((currentticks <= 0) && (reverseticks > 0))
      {
          reverserunsvar++;
          currentrunmode = 1;
            initialpullermillis = millis();
          startpullermillis = pullerdelay + initialpullermillis;
          statusupdate();
      } //Checks to see if it has moved backwards the same number of
ticks it moved forwards. If it has, then it logs a completed reverse
run, and puts the motor into forward mode.


    if(pulleropmode == 4 && (startpullermillis - initialpullermillis)
<= 0 && currentticks > 0){
          startpullermillis = 0;
          initialpullermillis = 0;
            digitalWrite(upPin, LOW); //Puller moves down.
            digitalWrite(downPin, HIGH);
            reversemotorpulse.check();
            }
      else if(pulleropmode == 4 && (startpullermillis -
initialpullermillis) > 0)
           initialpullermillis = millis();

    if(pulleropmode == 5 && (startpullermillis - initialpullermillis)
<= 0  && currentticks > 0){
          startpullermillis = 0;
          initialpullermillis = 0;
            digitalWrite(upPin, HIGH); //Puller moves up.
```

```
            digitalWrite(downPin, LOW);
            reversemotorpulse.check();
            }
      else if(pulleropmode == 5 && (startpullermillis -
initialpullermillis) > 0)
           initialpullermillis = millis();

}



/***************************
* Status Update Function *
***************************/
//This function will send status updates to the GUI every once in a
while.
void statusupdate()
{
      Serial.print("Puller Mode: ");
      Serial.println(pulleropmode);
      Serial.print("Puller End Position: ");
      Serial.println(pullerendPosition);
      Serial.print("Puller Move Time: ");
      Serial.println(pullermovetime);
      Serial.print("Puller Delay: ");
      Serial.println(pullerdelay);
      Serial.print("Rotation Mode: ");
      Serial.println(rotationopmode);
      Serial.print("Rotation Speed: ");
      Serial.println(rotationspeed);
      Serial.print("Rotation Delay: ");
      Serial.println(rotationdelay);
      Serial.print("Number of Total Runs: ");
      Serial.println(totalrunsvar);
      Serial.print("Number of Forward Runs: ");
      Serial.println(forwardrunsvar);
      Serial.print("Number of Reverse Runs: ");
      Serial.println(reverserunsvar);
      Serial.print("Total Ticks: ");
      Serial.println(totalticks);
      Serial.print("Current Tick: ");
      Serial.println(currentticks);
      Serial.println();
}
```

Visual Basic .net Code:

```
Imports System.Math
Imports System

'http://msdn.microsoft.com/en-us/library/dy85x1sa.aspx For string
contains method.

Public Class MainView

    Dim WithEvents serialPort As New IO.Ports.SerialPort
    Dim currenttext As String
    Dim arduinooutput() As String

    Private Sub Form1_Load( _
       ByVal sender As System.Object, _
       ByVal e As System.EventArgs) _
       Handles MyBase.Load

        'Tooltips (mouse hover text) goes here
        Me.ToolTip1.SetToolTip(Me.BtnPullDown, "")
        Me.ToolTip1.SetToolTip(Me.BtnPullUp, "")

        For i As Integer = 0 To _
           My.Computer.Ports.SerialPortNames.Count - 1
            cbbCOMPorts.Items.Add( _
               My.Computer.Ports.SerialPortNames(i))
        Next
        btnDisconnect.Enabled = False
    End Sub

    Private Sub DataReceived( _
       ByVal sender As Object, _
       ByVal e As System.IO.Ports.SerialDataReceivedEventArgs) _
       Handles serialPort.DataReceived



        txtDataReceived.Invoke(New _
                        myDelegate(AddressOf updateTextBox), _
                        New Object() {})
        Dim stringseparators() As String = {": "}
        arduinooutput = currenttext.Split(stringseparators, _
                      StringSplitOptions.RemoveEmptyEntries)

        Dim stval As Integer
        Dim ardcurrtick As Integer
        Dim ardendtick As Integer
        Control.CheckForIllegalCrossThreadCalls = False
        If arduinooutput(0) = "Puller Mode" Then
            stval = Convert.ToInt16(arduinooutput(1))
            Select Case stval
                Case "1"
                    StPullMode.Text = "Off"
                Case "2"
                    StPullMode.Text = "Force Up"
```

```
                Case "3"
                    StPullMode.Text = "Force Down"
                Case "4"
                    StPullMode.Text = "Pulling Up"
                Case "5"
                    StPullMode.Text = "Pulling Down"
            End Select
        End If
        If arduinooutput(0) = "Rotation Mode" Then
            stval = Convert.ToInt16(arduinooutput(1))
            Select Case stval
                Case "1"
                    StRotMode.Text = "Off"
                Case "2"
                    StRotMode.Text = "Forward"
                Case "3"
                    StRotMode.Text = "Reverse"
                Case "4"
                    StRotMode.Text = "ACRT"
            End Select
        End If
        If arduinooutput(0) = "Puller End Position" Then
            ardendtick = Convert.ToInt32(arduinooutput(1))
            stPullTotTicks.Text = ardendtick
        End If
        If arduinooutput(0) = "Puller Move Time" Then
            stval = Convert.ToInt32(arduinooutput(1)) / (60)
        End If
        If arduinooutput(0) = "Number of Forward Runs" Then
            stval = Convert.ToInt32(arduinooutput(1))
            stPullForwardRun.Text = stval
        End If
        If arduinooutput(0) = "Number of Reverse Runs" Then
            stval = Convert.ToInt32(arduinooutput(1))
            stPullReverseRun.Text = stval
        End If
        If arduinooutput(0) = "Number of Total Runs" Then
            stval = Convert.ToInt32(arduinooutput(1))
            stPullTotalRuns.Text = stval
        End If
        If arduinooutput(0) = "Total Ticks" Then
            stval = Convert.ToInt32(arduinooutput(1))
            stPullTotTicks.Text = stval
        End If
        If arduinooutput(0) = "Current Tick" Then
            ardcurrtick = Convert.ToInt32(arduinooutput(1))
            stPullCurrTick.Text = ardcurrtick
        End If

    End Sub

    Private Sub btnSend_Click( _
       ByVal sender As System.Object, _
       ByVal e As System.EventArgs) _
       Handles btnSend.Click
        Try
            serialPort.Write(txtDataToSend.Text & vbCr)
```

```
            With txtDataReceived
                .SelectionColor = Color.Black
                .AppendText(txtDataToSend.Text & vbCr)
                .ScrollToCaret()
            End With
            txtDataToSend.Text = String.Empty
        Catch ex As Exception
            MsgBox(ex.ToString)
        End Try
    End Sub

    Public Delegate Sub myDelegate()
    Public Sub updateTextBox()
        With txtDataReceived
            .Font = New Font("Microsoft Sans Serif", 8.25!,
FontStyle.Bold)
            .SelectionColor = Color.Red
            currenttext = serialPort.ReadLine
            .AppendText(currenttext)
            .ScrollToCaret()
        End With
    End Sub

    Private Sub btnConnect_Click( _
       ByVal sender As System.Object, _
       ByVal e As System.EventArgs) _
       Handles btnConnect.Click
        If serialPort.IsOpen Then
            serialPort.Close()
        End If
        Try
            With serialPort
                .PortName = cbbCOMPorts.Text
                .BaudRate = 9600
                '.Parity = IO.Ports.Parity.None
                '.DataBits = 8
                '.StopBits = IO.Ports.StopBits.One
                .Encoding = System.Text.Encoding.ASCII
            End With
            serialPort.Open()

            lblMessage.Text = cbbCOMPorts.Text & " connected."
            btnConnect.Enabled = False
            btnDisconnect.Enabled = True
        Catch ex As Exception
            MsgBox(ex.ToString)
        End Try
    End Sub

    Private Sub btnDisconnect_Click( _
       ByVal sender As System.Object, _
       ByVal e As System.EventArgs) _
       Handles btnDisconnect.Click
        Try
            serialPort.Close()
            lblMessage.Text = serialPort.PortName & " disconnected."
            btnConnect.Enabled = True
```

```
            btnDisconnect.Enabled = False
        Catch ex As Exception
            MsgBox(ex.ToString)
        End Try
    End Sub

    Private Sub BtnRunPuller_Click(ByVal sender As System.Object, ByVal
e As System.EventArgs) Handles BtnRunPuller.Click
        Dim pullermode As Integer
        Dim encoderticks As Integer
        Dim pullertime As Double
        Dim pullertimedelay As Double
        Dim totalruns As Integer
        Dim reversetime As Double
        encoderticks = Round(PullDistNum.Value * 100)
        pullertime = PullingTimehrsnum.Value * 60 * 60
        pullertimedelay = Round(PullerTimeDelayUpDwn.Value * 60 * 1000)
        totalruns = PullerRunsCountUpDwn.Value
        reversetime = ReverseTimehrsnum.Value * 60 * 60
        Select Case PullerDirection.Text
            Case "Upwards"
                pullermode = 4
            Case "Downwards"
                pullermode = 5
        End Select
        Try
            serialPort.Write(pullermode & " 0 " & encoderticks & " " &
pullertime & " " & pullertimedelay & " " & totalruns & " 0 0 " &
reversetime & vbCr)
        Catch ex As Exception
            MsgBox(ex.ToString)
        End Try
    End Sub

    Private Sub BtnPullUp_Click(ByVal sender As System.Object, ByVal e
As System.EventArgs) Handles BtnPullUp.Click
        Try
            serialPort.Write("2 0 0 0 0 0 0 0 0" & vbCr)
        Catch ex As Exception
            MsgBox(ex.ToString)
        End Try
    End Sub

    Private Sub BtnPullDown_Click(ByVal sender As System.Object, ByVal
e As System.EventArgs) Handles BtnPullDown.Click
        Try
            serialPort.Write("3 0 0 0 0 0 0 0 0" & vbCr)
        Catch ex As Exception
            MsgBox(ex.ToString)
        End Try
    End Sub

    Private Sub BtnStopPuller_Click(ByVal sender As System.Object,
ByVal e As System.EventArgs) Handles BtnStopPuller.Click
        Try
            serialPort.Write("1 0 0 0 0 0 0 0 0" & vbCr)
        Catch ex As Exception
```

```
            MsgBox(ex.ToString)
        End Try
    End Sub

    Const NumSeconds As Integer = 5
    Private Sub Button1_Click(ByVal sender As System.Object, ByVal e As
System.EventArgs) Handles cmBtn.Click
        serialPort.Write("2 0 0 0 0 0 0 0 0" & vbCr)
        Timer1.Interval = 1000  'measure seconds
        Timer1.Enabled = True
    End Sub

    Private Sub Timer1_Tick(ByVal sender As System.Object, ByVal e As
System.EventArgs) Handles Timer1.Tick
        Static n As Integer
        n = n + 1
        If n >= NumSeconds Then
            serialPort.Write("1 0 0 0 0 0 0 0 0" & vbCr)
            Timer1.Enabled = False
            n = 0
        End If
    End Sub


    Private Sub BtnStopAll_Click(ByVal sender As System.Object, ByVal e
As System.EventArgs) Handles BtnStopAll.Click
        serialPort.Write("1 1 0 0 0 0 0 0 0" & vbCr)
    End Sub

    Private Sub BtnRunRot_Click(ByVal sender As System.Object, ByVal e
As System.EventArgs) Handles BtnRunRot.Click
        Dim rotpwmspeed As Integer
        Dim rotationmode As Integer
        Dim rottimedelay As Double
        rotpwmspeed = RotationSpeedUpDwn.Value
        rottimedelay = Round(RotTimeDelayUpDwn.Value * 60 * 1000)
        Select Case RotationDirection.Text
            Case "Forwards"
                rotationmode = 2
            Case "Backwards"
                rotationmode = 3
            Case "ACRT"
                rotationmode = 4
        End Select
        serialPort.Write("0 " & rotationmode & " 0 0 0 0 " &
rotpwmspeed & " " & rottimedelay & " 0" & vbCr)
    End Sub

    Private Sub BtnStopRot_Click(ByVal sender As System.Object, ByVal e
As System.EventArgs) Handles BtnStopRot.Click
        serialPort.Write("0 1 0 0 0 0 0 0 0" & vbCr)
    End Sub

End Class
```

Visual Basic .net User Interface:

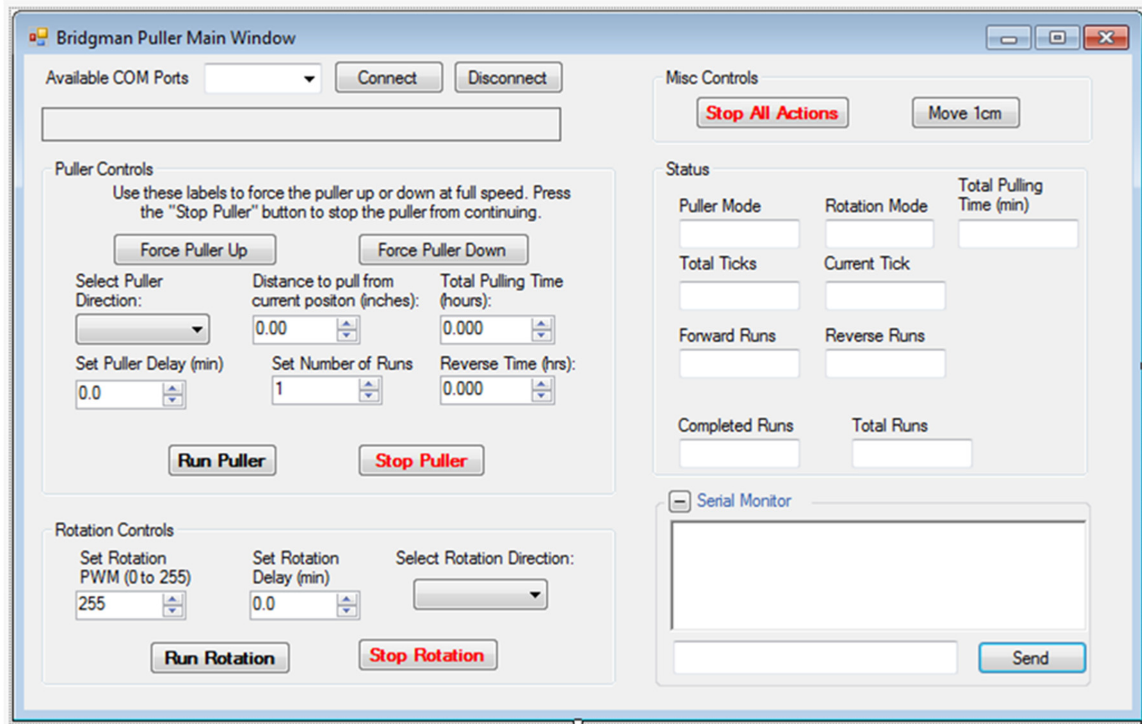

# APPENDIX C – MATLAB SOFTWARE FOR PULSE SHAPING

```
T=1e-8; % Sampling Interval
tau = 2e-6; % Time Constant

a=1/tau;
ap=exp(-T/tau);

% CR-RC^4 Z-transfer function
z = tf('z', T);
hz = (z^4*ap*T^3*(4-(a*T)) + z^3*ap^2*T^3*(12-11*a*T) +
z^2*ap^3*T^3*(-12-11*a*T) + z*ap^4*T^3*(-4-a*T)) / (24*(z-
ap)^5); [hznum hzden Ts] = tfdata(hz,'v');

% Baseline correction for data
sz = size(data,1);
pct = .25;
psz = round(pct*sz);
baselinemode = mode(data(psz,1));
data2 = data - baselinemode;

% Filter for signal
xf=filter(hznum,hzden,data2);
```